SUBMILLIMETER HETERODYNE SPECTROSCOPY OF STAR FORMING REGIONS

by

Christopher Emil Groppi

A Dissertation Submitted to the Faculty of the

DEPARTMENT OF ASTRONOMY

In Partial Fulfillment of the Requirements

For the Degree of

DOCTOR OF PHILOSOPHY

In the Graduate College

THE UNIVERSITY OF ARIZONA

2 0 0 3

THE UNIVERSITY OF ARIZONA ®
GRADUATE COLLEGE

As members of the Final Examination Committee, we certify that we have read the dissertation prepared by Christopher Emil Groppi entitled Submillimeter Heterodyne Spectroscopy of Star Forming Regions

and recommend that it be accepted as fulfilling the dissertation requirement for the Degree of Doctor of Philosophy

Christopher K. Walker	10/28/2003 Date
John H. Bieging	11/4/2003 Date
Michael R. Meyer	11/4/2003 Date
Erick T. Young	11/4/2003 Date
	Date

Final approval and acceptance of this dissertation is contingent upon the candidate's submission of the final copy of the dissertation to the Graduate College.

I hereby certify that I have read this dissertation prepared under my direction and recommend that it be accepted as fulfilling the dissertation requirement.

Dissertation Director, Christopher K. Walker — 10/28/2003 Date

STATEMENT BY AUTHOR

This dissertation has been submitted in partial fulfillment of requirements for an advanced degree at The University of Arizona and is deposited in the University Library to be made available to borrowers under rules of the Library.

Brief quotations from this dissertation are allowable without special permission, provided that accurate acknowledgment of source is made. Requests for permission for extended quotation from or reproduction of this manuscript in whole or in part may be granted by the head of the major department or the Dean of the Graduate College when in his or her judgment the proposed use of the material is in the interests of scholarship. In all other instances, however, permission must be obtained from the author.

SIGNED: Christopher E. Gryga

ACKNOWLEDGEMENTS

This dissertation represents the work I have done since my arrival at Steward Observatory and SORAL in 1997. The four projects described here, especially the instrumentation projects, are products of the work of many people, before and after my arrival at SORAL.

My advisor, Christopher Walker, was the inspiration behind the ideas that are brought forth in these projects. His willingness to dare, to take on the projects others thought impossible, are the driving force behind my work and success. He has taught me that nothing is impossible, and the only thing in our way is the inability to dream.

Work on the PoleSTAR and DesertSTAR receivers would have been impossible without the contributions of the people who have worked at SORAL throughout the years. The work of Jeff Capara, Henry Knoepfle, Gopal Narayanan, Aimee Hungerford, Dathon Golish, Craig Kulesa and Abby Hedden all made these projects possible. In addition, long hours put in by Jacob Kooi at Caltech and Kirby Hnat at Infrared Labs were invaluable.

I would particularly like to thank both Craig Kulesa and Dathon Golish, who have been instrumental in every project described here. Craig has written all the instrument control software we have. The two of us have spent long hours in the lab and at the South Pole, and he has answered my numerous stupid questions every time without complaint. Dathon Golish knows more about 3D solid modeling than anyone I know. All the incredibly detailed and beautiful 3D figures you will see in this thesis, and all of our proposals, talks and papers are his doing. I really don't know what we would have done if he had gone to graduate school somewhere else. He is already working at the level of a senior graduate student, even though he's only been one for a few weeks.

While many people see graduate school as a trying time, it has been the best time of my life. In no small way has this been influenced by all my friends, and particularly all the graduate students in the Astronomy department. Doug Miller and Christian Drouet d'Aubigny were two of the best friends and roommates anyone could hope for. I will fondly remember these times, from the stage of the graduate student play, to the bottom of a glass of Doug's beer.

Most thanks go to my best friend and wife Jackie. Throughout the time we've known each other, she has brought happiness and humor to my life. The word "soulmate" is an overused cliche, but I can't think of a better word to describe her. She is, simply put, the best thing that ever happened to me. I'd also like to thank Bartleby the Dog. No matter what the ailment, nothing heals like a wet nose and fuzzy, floppy ears.

Finally, I'd like to thank my parents who never ceased to encourage and help me since I decided that I wanted to be an astronomer at the age of 8. They have both made enormous sacrifices to help me get to where I am. None of this would have been possible without their help throughout my entire life.

DEDICATION

To my parents, Barbara and Robert Groppi. Without their love and support, none of this would be possible.

TABLE OF CONTENTS

TABLE OF CONTENTS - *Continued*

LIST OF FIGURES

LIST OF FIGURES - *Continued*

LIST OF TABLES

ABSTRACT

The sub-mm wave portion of the electromagnetic spectrum is on the frontier of both scientific and technical research in astrophysics. Being a relatively young field, scientific advancement is driven by advancements in detector technology. In this thesis, I discuss the design, construction, testing and deployment of two sub-mm wave heterodyne array receivers. PoleStar is a 4 pixel (2x2) heterodyne array built for operation in the 810 GHz atmospheric window. It is in operation at the AST/RO telescope at the South Pole. This receiver has increased imaging speed in this band at AST/RO by a factor of ~20 compared to previous receiver systems. DesertStar is a 7 pixel, hexagonally close packed heterodyne array receiver built to operate in the 345 GHz atmospheric window at the Heinrich Hertz Telescope in Arizona. This system will be a facility instrument at the telescope, and will increase mapping speed over the existing dual polarization single beam receiver at the telescope now by a factor of ~16. Both these receiver systems enable scientific projects requiring large area imaging that were previously impossible. I also discuss two scientific applications of sub-mm wave receiver systems. We have used multiple telescopes to observe several mm, submm transitions and continuum emission towards the R CrA molecular cloud core. Originally thought to be associated with high mass star formation, we find that the driving source behind the mm-wave emission is a low mass protostar. The close proximity of R CrA allows us to achieve high spatial resolution even with single dish mm-wave and sub-mm wave telescopes. With this resolution, we are able to disentangle the effects of infall, rotation and outflow motions. We also use vibrationally excited HCN emission to probe the protostellar accretion disk in a sample of nearby high and low mass protostars of varying ages. While these observations are difficult with single dish telescopes, we show the promise of the technique, and report results on 4 sources.

1. INTRODUCTION

The submillimeter region of the electromagnetic spectrum is one of the most recently accessible tools for the study of astrophysical phenomenon. Only in the past 35 years has Wilson, Jefferts and Penzias discovered emission from the CO molecule using the NRAO 36 foot telescope and a Schottky diode heterodyne receiver of their own design (Wilson et al. 1970). Since then, the study of molecular gas in our own galaxy and beyond has exploded. While a more mature discipline than in 1970, the submillimeter is still tied very closely to the technologies used to build telescopes and detectors. The combination of innovative science and innovative technology drives this field at a rapid pace. The technology of heterodyne receivers allows us to obtain very high spectral resolution. In addition, the natural linewidth of molecular transitions are small, encoding all the kinematics of the source into the molecular line shape. This makes the submillimeter an important tool in studying the star formation process. Deeply embedded and obscured protostars are invisible to visible and even infrared radiation. The only radiation that can penetrate the dust to allow study of the nascent star are far infrared, submillimeter and longer wave radiation. Since stars are born in molecular clouds, the molecular gas and dust present is the primary tool to probe very young objects.

Since the discovery of CO, the basic picture of the star formation process has been sketched. In the earliest stages, infalling gas, a rotating dense core, Keplarian disk rotation and feedback through molecular outflows are all competing processes occurring in most

protostellar sources. Size scales range from tens of AU for the protostellar source and inner accretion disk to parsecs for the outflow lobes and surrounding molecular cloud. We need to be able to see the combined effects of all these processes to be able to disentangle the data we collect and understand the process of star formation. Ideally, we would like to be able to collect data on size scales from individual protostars and accretion disks to entire molecular cloud complexes. With the next generation of submillimeter interferometers several years away, we need to develop techniques to study protostellar accretion disks with single dish sub-mm wave telescopes. By carefully choosing molecular tracers that only emit under conditions found in the disk (i.e. high density and temperature), we can study the disk through its kinematic signature encoded in the shape of the molecular line. With small maps and the moderate spatial resolution available to us with single dish telescopes, we can spatially resolve and study infall and rotation, again through the information encoded in the line shapes. Individual outflows are within our reach with moderate to large scale mapping observations. The ultimage goal of mapping entire molecular clouds at the spatial and spectral resolution necessary to begin to understand the star formation feedback process is still difficult or impossible.

Since study of protostars began, technology has been a limiting factor in our ability to understand the star formation process. Outflows can contain as much or more mass than the protostellar source driving them. They influence the molecular cloud energetics and structure far from the source, but the role outflows play in the life cycle of molecular clouds is not well known. All but a few sub-mm receiver systems on today's radio tele-

scopes have a single spatial pixel. While the On-The-Fly mapping process, and decreases in receiver noise temperature have dramatically increased mapping speed allowing for moderately wide field imaging, the technology is reaching its limit. Most modern receivers are within a few times the quantum noise limit of hν/k, the uncertainty of a single photon, inherent to all coherent detection techniques. While dual polarization and single sideband receiver systems can increase mapping speed by factors of ~2, the only way to break through the barrier preventing wide field imaging with large single dish telescopes is through focal plane arrays. The Steward Observatory Radio Astronomy Laboratory (SORAL) has been a pioneer in the development of heterodyne focal plane arrays at submillimeter wavelengths. Currently, there are only four submillimeter wave heterodyne array receivers in operation in the world, and only three more millimeter wave (heterodyne) array receivers. Table 1 summarizes these receivers. In this dissertation, I discuss the two heterodyne array receivers built by SORAL in the past 6 years: PoleStar, a 4 pixel array receiver operating in the 810 GHz atmospheric window, and DesertStar, a 7 pixel array receiver operating in the 345 GHz atmospheric window. Both receivers increase mapping speed for wide field imaging by over an order of magnitude compared to the single pixel receivers at their respective telescopes. This increase in imaging capability brings into reach projects that were impossible before their construction.

Using a combination of data from the AST/RO telescope at the South Pole, the Kitt Peak 12m telescope and the 10m Heinrich Hertz Telescope, we have studied the most active part of the R CrA molecular cloud. Since R CrA is extremely nearby, we are able to

obtain physical spatial resolution as high as 0.01pc over an area of 0.16 pc^2, with velocity resolution finer than 1 km/s. With this combination of spatial and spectral resolution, we can separate the effects of infall, rotation and outflow to assemble a clear picture of low mass star formation in action. Using vibrationally excited HCN(4-3) emission as a probe of protostellar accretion disks, we have developed a technique for finding and studying structure in these disks without spatially resolving disk structure. While the observations are difficult with single dish telescopes, the technique has promise for unlocking the secrets within protostellar disks, and might lead to a better understanding of the star and planet formation process. In addition, this technique can be applied with the next generation of sub-mm wave interferometers increasing its effectiveness by orders of magnitudes.

Receiver	Location	Frequency	Beams
NRAO 8 beam	Kitt Peak 12m	230 GHz	8
BEARS	Nobayama 45m	230 GHz	25
HERA	IRAM 30m	230 GHz	9 (2 pol)
CHAMP	CSO	460 GHz	15 (2 pol)
SMART	KOSMA 3m	460/810 GHz	8x2
DesertStar	HHT 10m	345 GHz	7
PoleStar	AST/RO 1.8m	810 GHz	4

Table 1: Operational Heterodyne Array Receivers

2. POLESTAR: AN 810 GHZ ARRAY RECEIVER FOR AST/RO

2.1 Introduction

A 4-pixel array receiver constructed to operate in the astrophysically important 810 GHz atmospheric window was assembled and tested at the Steward Observatory Radio Astronomy Lab (SORAL) and installed on the Antarctic Submillimeter Telescope and Remote Observatory located at the South Pole (AST/RO) at the South Pole (Groppi et al. 2000). In this chapter, we describe the instrument and its performance both in the lab and on the telescope. The cold, dry conditions at the South Pole, coupled with its relatively high altitude (~10,500 ft.) make it an excellent location for observations at submillimeter wavelengths. AST/RO has a 1.7 m aperture and was designed to take advantage of these conditions (Stark et al 2001). Figure 1 shows a CO J=(4-3) image of the giant molecular cloud NGC 6334 made with AST/RO. CO J=(7-6) and [CI] $^3P_2$ spectra toward the same object are also shown. These are first light data taken in the middle of the Antarctic summer with a dual channel, 460/810 GHz receiver system built by our team a few years ago. Much higher atmospheric transmission is routinely available in the winter. These almost ideal atmospheric conditions and the resulting observing efficiency available from the South Pole motivated us to build an 810 GHz array for use on AST/RO. Figure 2 is a photograph of the receiver front-end as it appeared in the lab before deployment.

2.2 Receiver Description

2.2.1 Pole Star Optical Design

The purpose of the optical system is to re-image AST/RO's focal plane onto a compact 2x2 array of lenses located in the array cryostat and to efficiently inject local oscillator power into each mixer. Focal plane re-imaging is achieved by a pair of parabolic mirrors and two flats (Figure 3). Each AST/RO beam expands from the focal plane located ~900 mm above the receiver pallets on to the first offset parabola (P1). P1 collimates the beams and conveys them via two flats to the second parabola (P2). P2 focuses and re parallelizes the beams so that they arrive at the mixer lenses with the correct size and placement. The beam footprint of the array on NGC 6334 is shown in Figure 1 (open circles). Each diffraction limited, half-power beam diameter is ~54". A quasi-optical LO power divider (Figure 4) is used to split the focused LO beam into 4 equal parts. The power dividing is accomplished by two, low-loss, ~50% crystalline quartz beam splitters. Each beam splitter is paired with a flat mirror to give the emerging beams the proper horizontal and vertical offsets. After including all loss mechanisms, we estimate that 18% of the incident LO power is in each LO beam at the output of the power divider. Initially, the plates in the power splitter were fixed, but an upgraded design was later added with adjustable mirrors and plates, along with screw-type attenuators for leveling LO power. The LO polarization is orthogonal to the signal beams. The four beams are then injected into the sky signal path by a high quality wire grid. A Martin-Pupplet Interferometer (MPI) then rotates the LO beam polarization to match that of the sky and directs them into the cry-

ostat. A 2x2 array of HDPE lenses then focuses the beams into the mixer feedhorns. We later chose to replace the MPI with a simple Mylar beamsplitter. While the MPI theoretically couples 100% of both the LO and sky power, they are very sensitive to misaligned beams. Even a 0.5 degree beam squint can cause 3 dB of loss in both LO and sky power, adding close to 600K of noise (Martin et al. 1977). Some groups, like KOSMA, solve this problem by holding each mixer by the horn with a precision machined reference plate. We were not able to do this since the Potter horns used for the PoleStar mixers were too fragile. This makes it virtually impossible to co-align all 4 mixer beams. The Mylar diplexer is not sensitive to mixer squint, and adds very little loss as long as the Mylar thickness is kept small.

2.2.2 JPL Local Oscillator

The first major upgrade to PoleStar was the replacement of the LO chain with whisker contacted multipliers with a state-of-the-art planar diode LO chain with 100 GHz power amplifiers before the first doubler. This LO chain uses multipliers developed for the Herschel HIFI project, designed and built jointly by JPL and UMass (Mehdi et al. 2003). The source is a 100 GHz Gunn Oscillator from J. Carlstrom. This is followed by two 100 GHz power amplifiers in series, then a 200 GHz doubler, a 400 GHz doubler and an 800 GHz doubler. The multipliers are self biased and tunerless. Measured power output at the operational frequency of 807.3 GHz is in excess of 250 μW. After the LO upgrade, it was possible to saturate all the mixers using only a 0.5 mil Mylar beamsplitter. In addition, the

self-biased tunerless operation makes the system much easier to use for the winter-over operators. Figure 5 shows the JPL/UMass LO chain installed on PoleStar.

2.2.3 Pole Star Front-End Design

2.2.3.1 Cryostat

The Pole STAR cryostat (Figure 6) was constructed by Precision Cryogenics and is based on the successful Caltech Submillimeter Observatory (CSO) hybrid design. It uses a CTI model 350 coldhead to cool the outer and inner radiation shields to ~77 and ~12 K, respectively and a 4 liter liquid helium can to maintain the mixers at their operating temperature. This same basic design is used for all AST/RO and CSO receivers. In the single pixel AST/RO receivers, 30.5 mm diameter, Teflon coated, crystalline quartz windows are used at 300 and 77 K. Zitex is used as the IR filter on the 12 K radiation shield. With a good vacuum, hold times of ~6 days can be achieved. With Pole STAR, we have 4 such apertures to contend with in the same cryostat. Furthermore, Teflon coated, crystalline quartz windows are difficult to obtain and the emerging beams from our close-packed lens array makes it impossible to fabricate 4 independent vacuum windows. At 77 K, we have simply substituted an additional layer of Zitex for the 50 mil quartz windows. For the 300K vacuum window, we use a 0.3 in. thick z-cut crystalline quartz vacuum window with polyethylene anti-reflection coating, and diamond dust coating on the inner surface to reduce thermal load. While polyethylene is not as good an anti-reflection coating as Teflon for crystalline quartz, it is easy to apply, robust and inexpensive. This window is based on

the design successfully used on the SPARO polarimeter used on the VIPER telescope also at the South Pole (Dotson et al. 1998). This window has virtually no loss at 810 GHz, and dramatically improved the dewar hold time and vacuum compared to earlier windows. With all 4 mixers and amplifiers mounted in the cryostat, the measured hold time is ~3 days. The hold time is much better than expected based upon the optimum performance of the single pixel receivers. This was achieved by doing away with the vent tube normally used in these cryostats. In the lab we have found that without the vent tube, the fill line is LESS likely to ice up, most likely due to the increased back pressure of helium gas.

2.2.3.2 Mixers

The SIS mixers used in PoleStar were made by KOSMA. Each mixer uses a Potter horn with a circular to half height rectangular waveguide transition to couple radiation to a Nb SIS junction. The junctions achieve low noise (~450 - 650K) performance through the use of an on-substrate Al tuning structure and a fixed waveguide backshort. The mixers have embedded magnets to suppress the Josephson effect. A four-wire bias system is used to ensure stable operation of the mixers. Figure 7 shows a SEM image of the junction and on-chip tuning structure. The inductive stub tunes out the capacitance of the SIS junction over the entire operating band, eliminating the need for mechanical backshort and E-plane tuners. Figure 8 is a picture of one of the PoleStar mixers. Each mixer is extremely compact, with a small, square cross-section allowing easy stacking in recilinear arrays. A novel magnet probe design with a rear-mounted electromagnet spool allows the mixers to

be packed directly against each other. These mixers are prototype designs for the KOSMA effort to build mixers for Herschel HIFI instrument's band 4. Developments pushed by this effort promise to reduce mixer noise temperatures to below 300K at 800 GHz in the next few years.

2.2.3.3 Pole Star IF Processing

Figure 9 provides a global schematic of the IF processing in Pole Star. The 1.5 GHz output of each mixer is amplified ~30 dB by a low-noise, 1-2 GHz amplifier mounted to the cryostat's 12 K radiation shield (Figure 6). The amplifiers are balanced and have a Lange coupler on their input, effectively eliminating the need for an isolator (Kooi 1998). Each signal is then amplified an additional 35 dB by room temperature Miteq amplifiers mounted on the dewar frame. After passing through a 3.6m cable run the array IFs enter a 4-channel total power box. The total power box provides 60 db more amplification and contains a bandpass filter and crystal detector that permits the total power of each receiver channel to be measured either manually or under computer control. Once through the total power box, the 4 IFs enter an up/downconverter box which translates the 1.5 GHz IFs to 14.5 GHz and then down to 2.075 GHz, the center frequency required by the array Acousto-Optical Spectrometer (aAOS) (see the next section).

2.2.3.4 Pole Star Array AOS

The Array AOS (aAOS) built by KOSMA provides four independent spectrometer channels, each with ~1 MHz of spectral resolution over a 1 GHz bandwidth. At 810 GHz, these numbers translate to 0.37 and 370 km/s respectively. It uses a single laser, a 4-channel, lithium niobate Bragg cell, and a custom CCD to achieve its performance parameters. The aAOS has been successfully tested on the IRAM 30m and CSO. This spectrometer also benefits from KOSMA's contribution to the Herschel HIFI instrument, through their contract to provide a multi-channel spectrometer system for the instrument (Schieder et al. 2003).

2.2.3.5 Pole Star Bias Control Hardware

The SIS junctions, the electromagnets used to suppress quantum-generated mixer noise, and the Low Noise Amplifiers (LNAs) all require noise-free, accurate electrical biasing for reliable operation. On single-pixel receivers, providing the appropriate biasing voltages and currents is handled adequately by individual boxes with manual potentiometers and LCD panels on the front. With the advent of array receivers, however, the sheer number of boxes required makes this kind of control impractical. The PoleStar bias system uses proven circuit design used on single pixel receivers at AST/RO and the Heinrich Hertz Telescope. We replace the manual potentiometers in these designs with a Xicor digital potentiometer, and package 4 channels of bias on a single Euro 96 card. These modular 4 channel cards can be plugged into a backplane in a 19" equipment rack, allowing

easy extensibility. All digital communications with the bias system are done through a bi-directional optically isolated connection with the control computer. The I^2C bus used for digital communications has a separate clock line. The digital lines, including the clock, are only active when changing a bias setting. The voltages and currents for the SIS junctions, magnets and amplifiers, the total power from the 4 channel total power box and the cryostat temperature information are read through a A/D card in the control computer. Signals from the bias system are multiplexed with Burr-Brown analog multiplexers, and read through a single BNC output. This design eliminates any clocks or digital signals in the bias rack except when changing to a new bias value. A block diagram of our bias control system is shown in Figure 10. This design can support up to 16-channels with no modifications, and is extensible to over 100 channels in its current configuration using a single control computer.

2.2.3.6 Software

The philosophy of compactness and flexibility, seen in the design of the computer controlled bias electronics, carries into the software design as well. The I^2C signals needed by the electronics is generated at the parallel port of an otherwise normal rack mounted PC running the Linux operating system. The excellent documentation of system internals, tight use of system resources, remote accessibility via X-Windows, and free compilers and programming tools make Linux an excellent choice for this design. An Intelligent Instrumentation PCI-20428W multi-purpose Data Acquisition (DAQ) card is

used for non-I^2C control of the instrument. The array software is highly modular and the source code, written in C and supplemented by Perl CGI is nearly independent of the hardware. The actual graphical user interface takes advantage of the open source, popular and highly capable GTK+ X-Windows toolkit. All bias control functions can be accessed remotely. The mixer bias control window is shown in Figure 11. The current Pole Star PC is powered by a 75 MHz AMD K5 processor, comparable to a 75 MHz Pentium, with only 32 MB of RAM.

2.3 Receiver Performance Measurements

2.3.1 Noise and stability measurements

Figure 12 shows the LO pumped IV curves of each of the three mixers currently functioning as of summer 2003, together with IF power sweeps. The fourth mixer has developed a super short and will be replaced during the Austral summer of 2003-2004. The red curve shows the IF power output when a HOT (290K) load is placed in front of the receiver. The blue curve shows the response with a COLD (77K) load After two seasons of upgrades, PoleStar is now working with noise temperatures close to those measured in the lab at Cologne with an optimized test receiver. After the installation of the new LO system with Mylar diplexer, the crystalline quartz window and properly leveling input power to both the total power box, up/down converter and aAOS, mixer noise temperatures are between 625K and 640K. Even with three pixels, the receiver is almost 15 times faster for mapping than WANDA, the single pixel 810 GHz facility receiver. Receiver stability mea-

surements on Pole STAR were made by monitoring the IF output power of two of the receivers over ~1000 sec. The IF power variation was about 1 part in 1000 over this period.

2.3.2 Beam pattern measurements

A computer controlled antenna test range was constructed to measure the 4 Pole STAR beams. We used a liquid nitrogen load with a 10 mm aperture as the signal source. The signal was chopped and synchronously detected using a lock-in amplifier connected to the receivers total power output. Maps of the 4-beams and their relative placement are shown in Figure 13. To within the measurement errors the beams have the right size and shape. One beam (from Mixer 3) had a small squint angle compared to the others. On warm-up, the horn on this mixer was found to be out of alignment and was readjusted.

2.3.3 First Light on AST/RO

Pole STAR was installed on AST/RO during a three week period from mid November to early December 2000. Figure 14 shows the First Light spectra obtained toward NGC 6334. Two CO J=7-6 and [CI] $^3P_2$ lines were observed. Figure 15 shows spectra taken with PoleSTAR in its latest configuration, with all upgrades. Spectra from the three functioning mixers are shown, also towards NGC 6334. The instrument has been at the South Pole continuously since the Austral summer of 2000.

2.4 Lessons Learned

In the process of building, deploying and operating PoleSTAR, we have learned several lessons that we can apply to all our future designs of heterodyne array receivers. Several components in the initial PoleSTAR design did not work as expected, and advances in technology have allowed us to improve receiver performance and reliability.

2.4.1 Local Oscillator and LO Injection Optics

Initially, one of the most pressing problems in developing an array for high frequency operation was the difficulty of obtaining LO power. At the time PoleSTAR was deployed, our LO source produced only 40 μW of power. This forced us to use a MPI LO diplexer since we could not afford to waste any LO power. While theoretically capable of delivering 100% of both the LO and sky power, small optical misalignments destroy their performance. While other solutions exist, especially for a fixed tuned receiver (Silicon etalons, meandering waveguide feeds), advancements in LO technology made this problem moot. We have benefited from the enormous development effort created by work for the Herschel HIFI instrument, which has increased available LO power by almost an order of magnitude since PoleSTAR was deployed (See Section 2.2.2). The new, more powerful LO is easier to align and use, is more robust, and the optics simplifications allowed for an improvement of more than 500K in receiver noise temperature.

2.4.2 Vacuum Windows

PoleSTAR also went through three iterations of vacuum windows before we found one with suitable performance. Anti-reflection coated crystalline (z-cut) quartz has the lowest loss of any material suitable for large diameter vacuum windows. Optimally, Teflon is used for the AR coating because its dielectric constant is the closest to the square root of the quartz. At the time of deployment, no company we could find would coat a vacuum window with Teflon. We decided to make a window out of high density polyethylene (HDPE), 0.5 in thick with pockets milled out for each beam. A solid window would have unacceptable loss at 810 GHz. By milling pockets leaving a membrane of 2λ thickness behind, the window spanned the 4 in. window aperture, with acceptable loss. While this window did work, it added ~200K to the receiver noise temperature and was subject to cracking. We next tried a window made from ZoteFoam PPA-30 nitrogen blown Teflon foam. This low dielectric constant material holds a vacuum, and has very low loss at 350 GHz. No measurements existed at 810 GHz, but the resulting window was very inexpensive and more robust than the HDPE window. We found the loss to be less, but this window still added ~150K to the receiver noise temperature. As shown in Figure 16, the loss of a slab of ZoteFoam rises rapidly above 400 GHz, possibly due to scattering off the foam cells. We finally chose a z-cut crystalline quartz window with polyethylene AR coating as discussed in section 2.2.3.1. This vacuum window cost over $3000 US, but is the only solution that offers good performance at 800 GHz over a 4 in. cryostat window aperture.

2.5 Summary

We have constructed a 2x2, 810 GHz array receiver for the AST/RO telescope. The array utilizes a common set of re-imaging optics, an efficient 4-way quasi-optical LO power splitter, a solid-state LO, low noise mixers, a flexible computer controlled bias system, and an array AOS. A state-of-the-art planar, tunerless LO chain with W-band power amplifiers can easily pump all the mixers with only a 0.5 mil Mylar LO diplexer. Upgrades and repairs have reduced the receiver noise temperatures to between 625K and 640K per mixer, making the system ~15 times faster for mapping than the previous 810 GHz system on the AST/RO telescope.

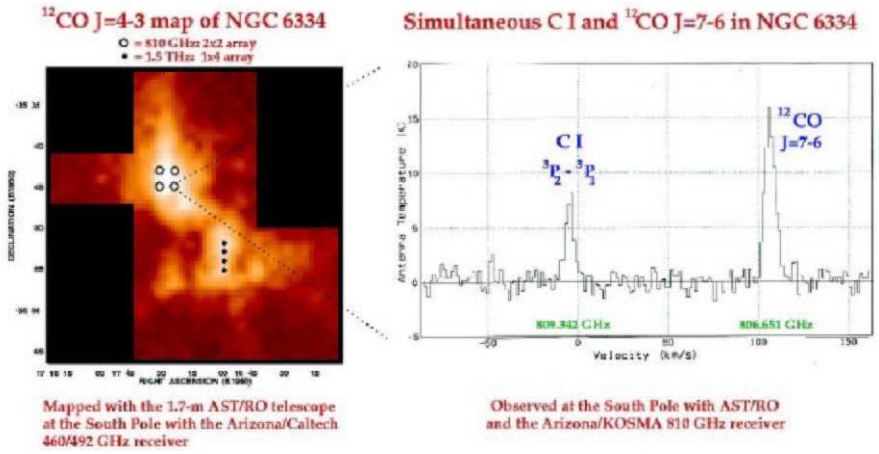

Figure 1: A map and spectra of NGC 6334.
This map was taken from the South Pole with a receiver built by SORAL. Superimposed on the map is the 2x2 beam footprint of PoleStar. The spectrum is of [CI] $^3P_2$ and CO(7-6) observed simultaneously with one line in each sideband.

Figure 2: PoleStar in the lab during front-end testing.
All system electronics fit into a single transportable equipment rack. A He-Ne laser is mounted on the optics plate here for optics alignment.

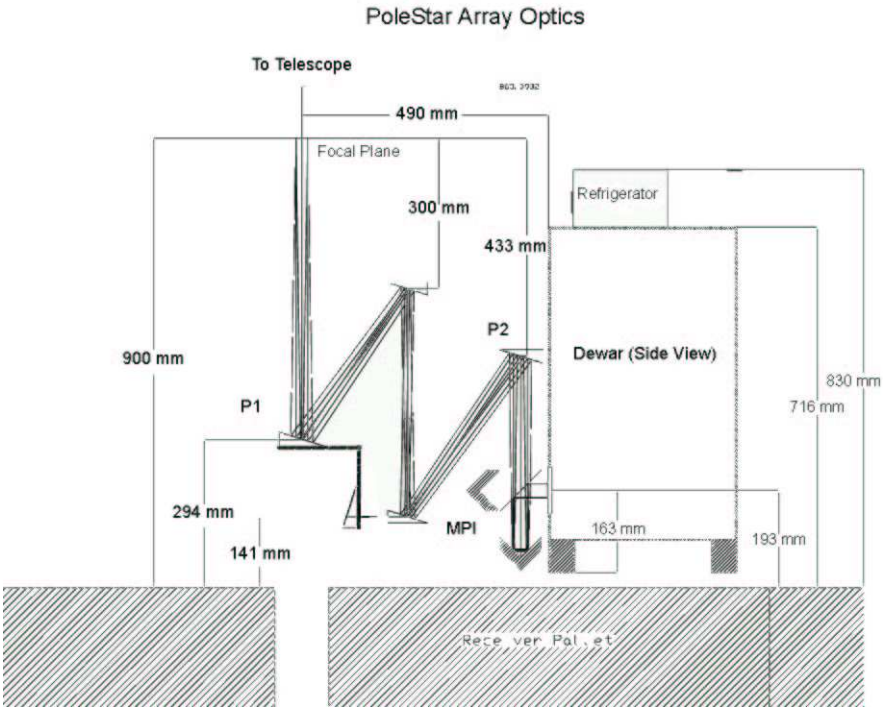

Figure 3: A optical diagram of the PoleStar re-imaging optics. All AST/RO receivers must re-image the focal plane to allow easy switching between the 4 receivers on the palate. MPI LO diplexer was later replaced with a Mylar beamsplitter.

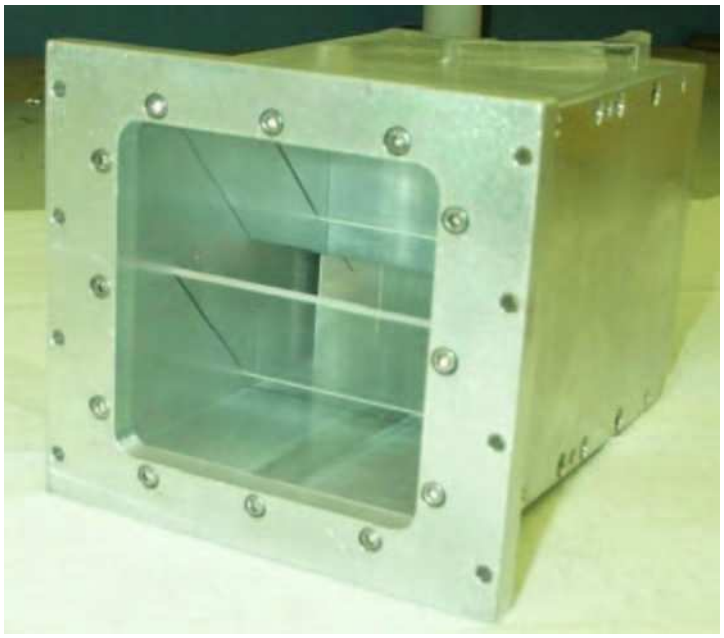

Figure 4: The PoleStar LO power splitter module. Two quartz plates and two mirrors split the single LO beam into a 4 beam array. Since PoleStar is fixed-tuned, this solution is simple and effective.

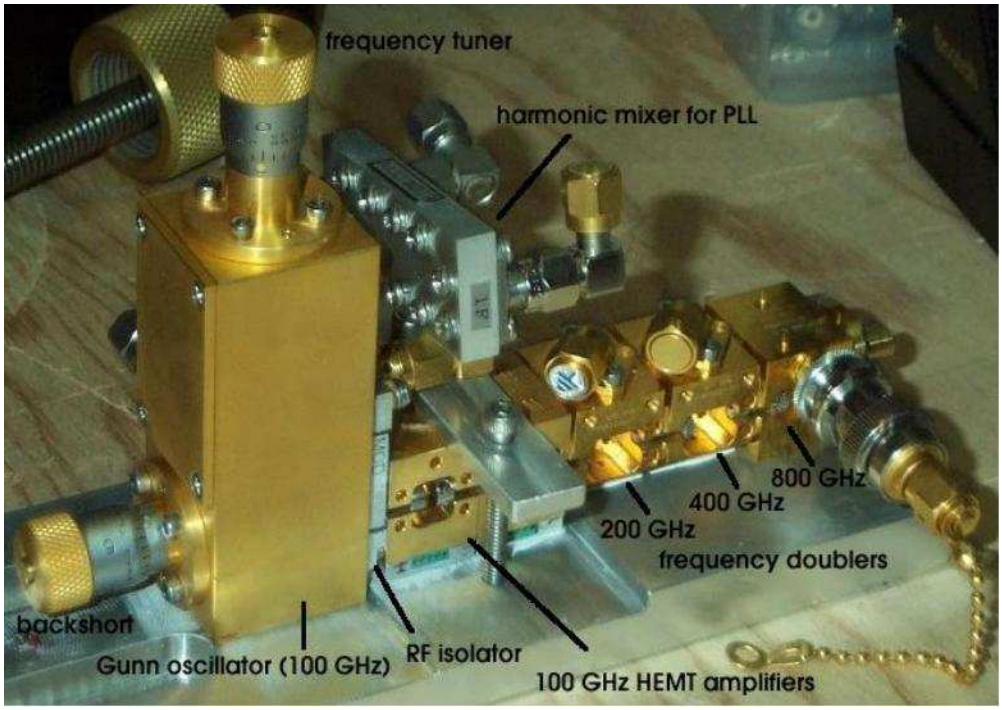

Figure 5: The JPL/UMass LO chain added to PoleStar.
This was added during the Austral summer of 2001. This chain puts out 0.25 mW at 807.3 GHz, enough to saturate all the mixers with a 0.5 mil thick Mylar LO diplexer. This LO chain is based on Herschel HIFI technology, using planar tunerless multipliers and 100 GHz power amplifier modules. Figure courtesy Craig Kulesa.

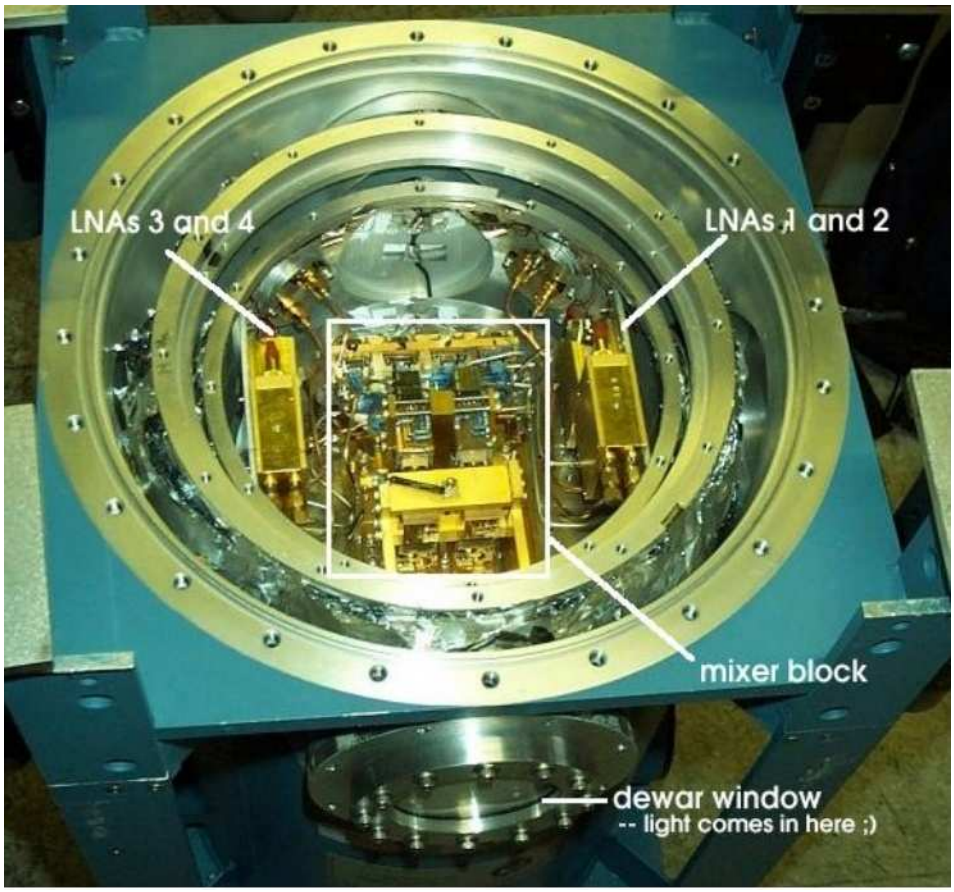

Figure 6: The inside of the PoleStar cryostat.
The 4 L-band Low-Noise IF amplifiers are mounted on the 15K radiation shield, and the mixers, lenses and bias tees are mounted on the 4K working surface. Figure courtesy Craig Kulesa.

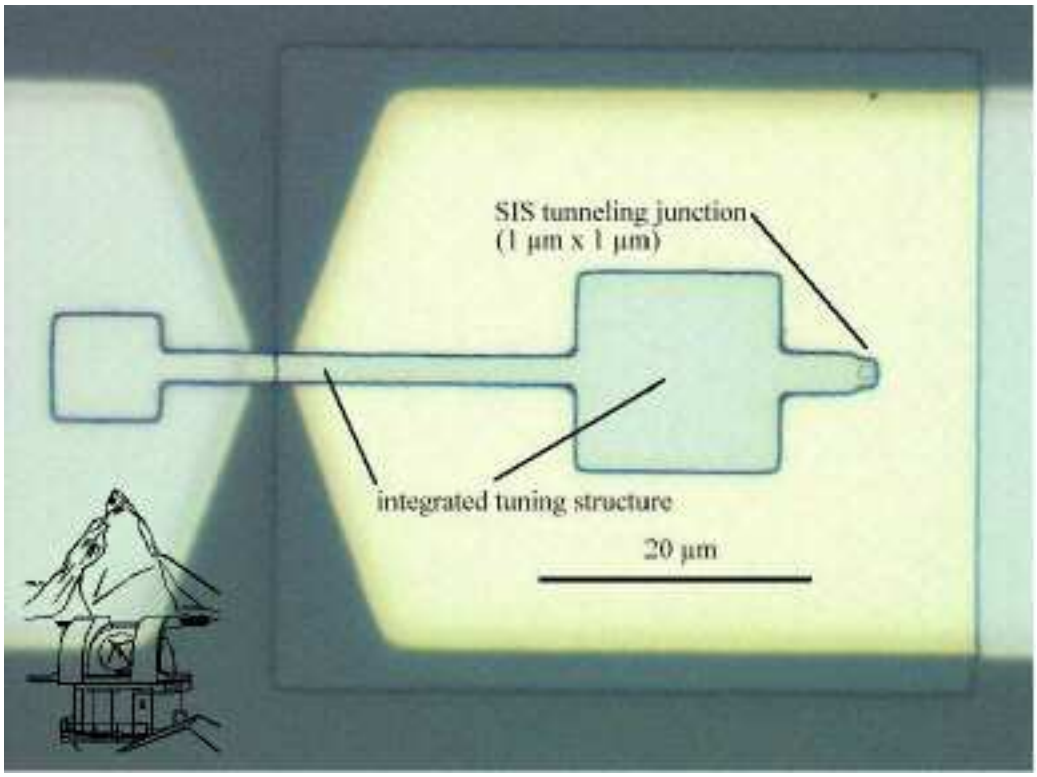

Figure 7: A SEM image of the SIS junction and on-chip tuning structure. The junction and tuning structure are fabricated at the center of a bowtie antenna and cross-guide choke structure on a quartz substrate. Figure courtesy Karl Jacobs.

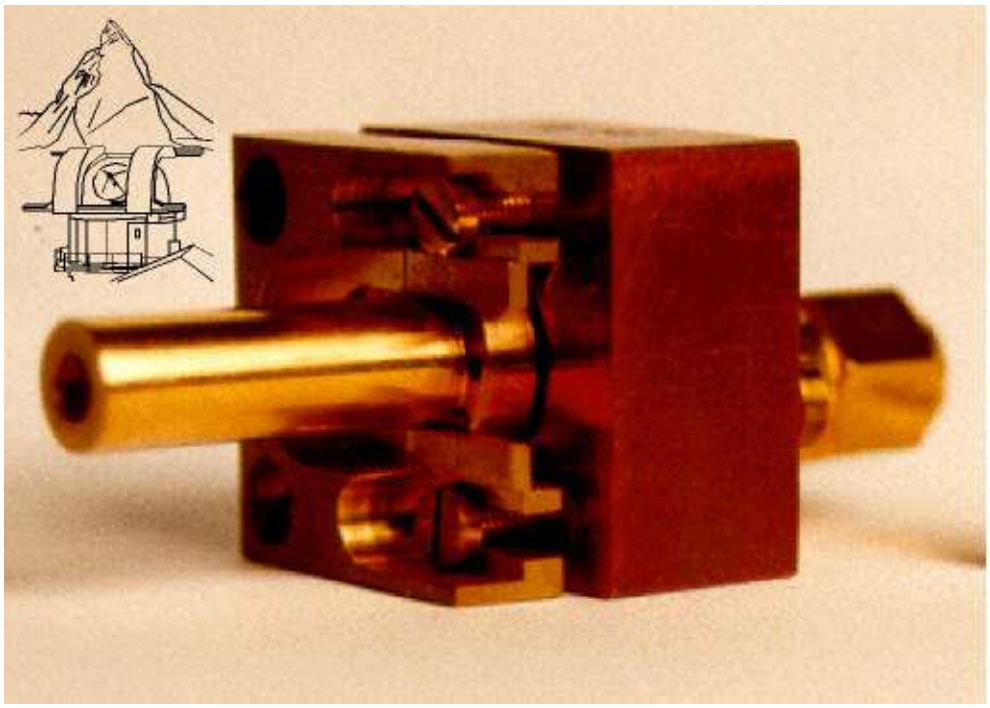

Figure 8: An image of a PoleStar mixer.
Unlike the SORAL designed mixer in DesertStar, the KOSMA mixers use separate bias tees to decrease the size of the mixer. With the separate cut-away horn, it is possible to inspect the junction and IF wire bond without removing the horn. Figure courtesy Karl Jacobs.

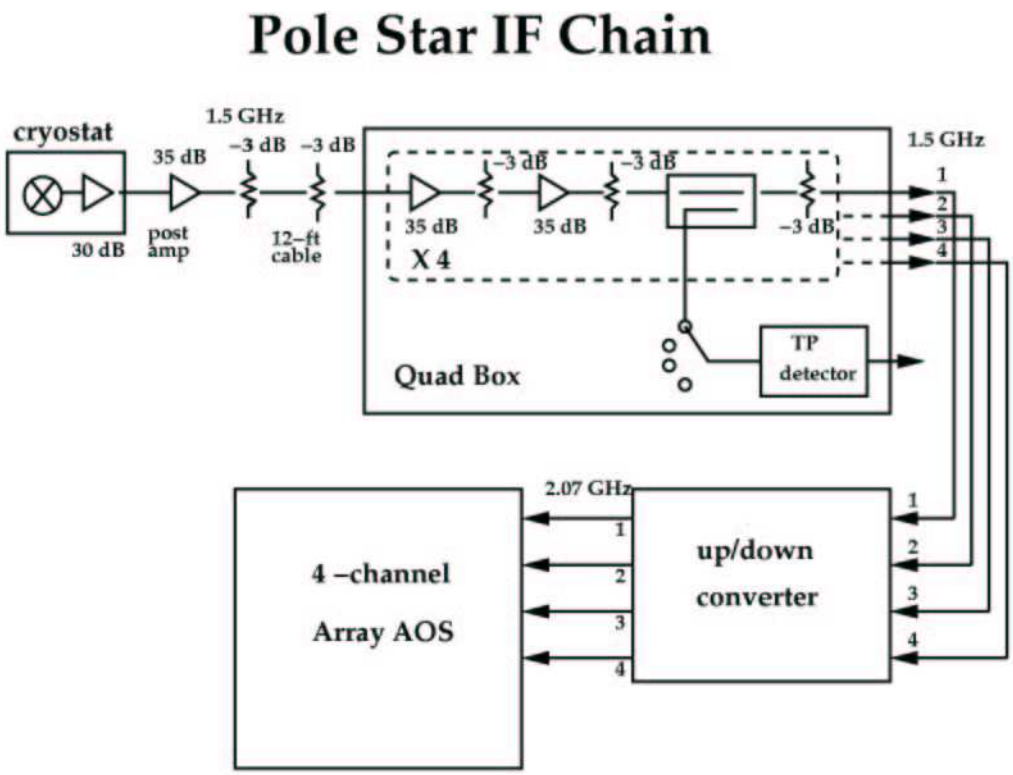

Figure 9: A block diagram of the PoleStar IF chain.
The box has a switch array to allow a single TP detector to monitor all 4 IF channels. A SAO built up/down converter translates the L-Band IF to the 1.1-2.1 GHz AOS input band.

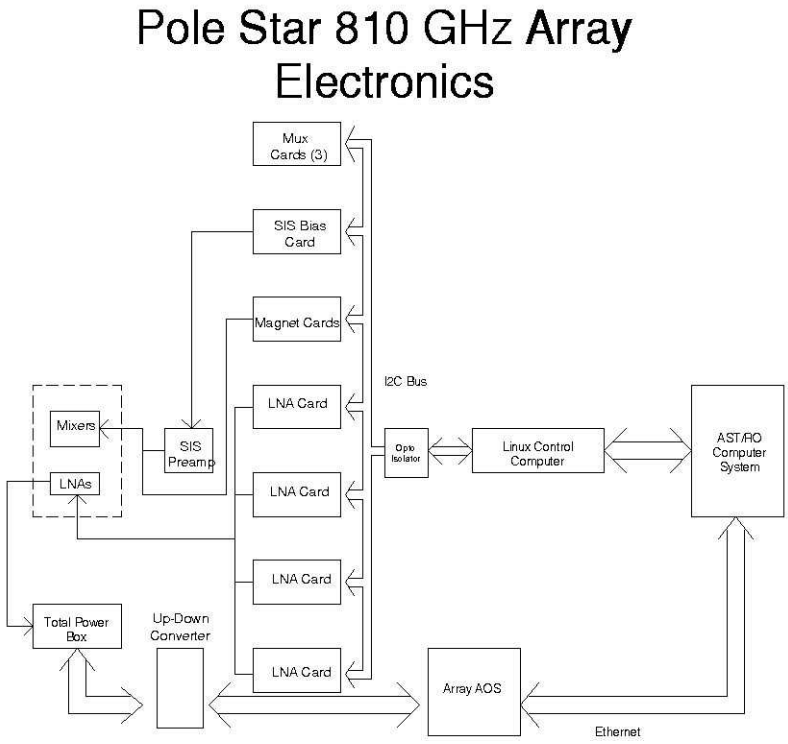

Figure 10: A block diagram of the PoleStar bias electronics system. All digital signals are isolated from the bias electronics during operation.

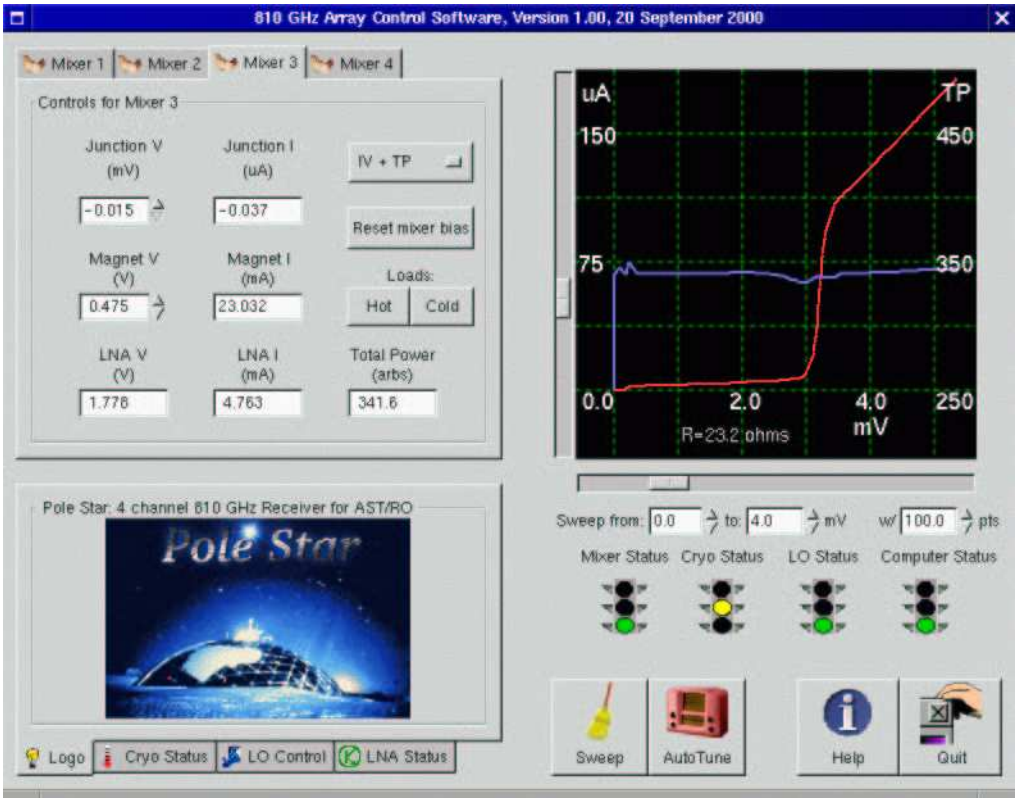

Figure 11: A screenshot of the PoleStar software interface.
The receiver can be controlled from the receiver room, or from a remote terminal. The software also writes a status webpage for remote performance monitoring.

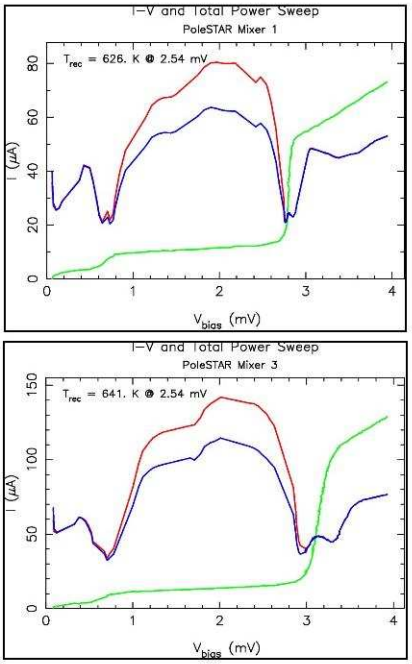

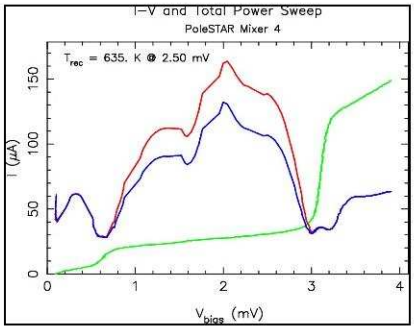

PoleSTAR IV & Total Power Curves

- T_{rx} of 625-640K
- One mixer developed a supershort in 2002.

Figure 12: Post-upgrade IV and total power curves.

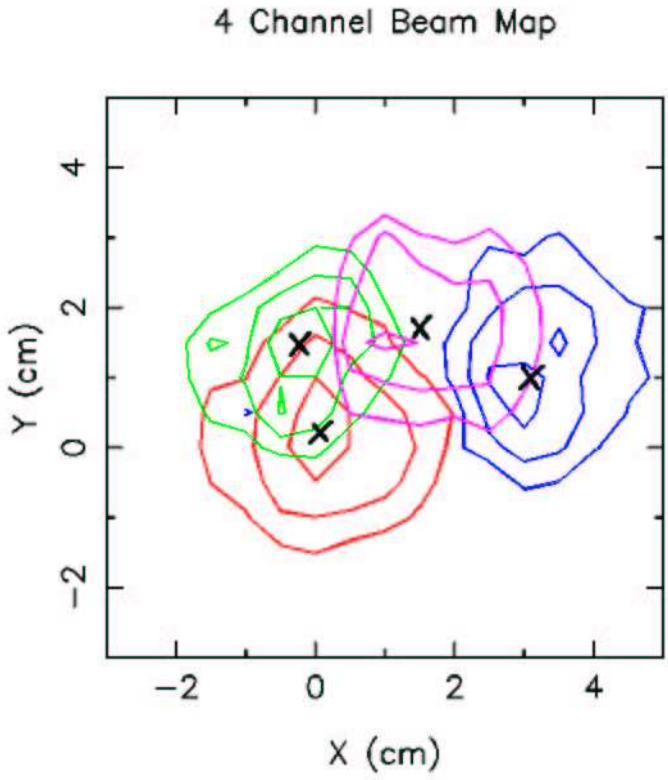

Figure 13: A beam map of the PoleStar beams.
These beam patterns were measured with the SORAL antenna test range. 3 of the 4 beams are in the proper location, and are the right size. The 4th beam was measured to be off, but was later corrected at the telescope by adjusting the mixer feedhorn. Figure courtesy Craig Kulesa.

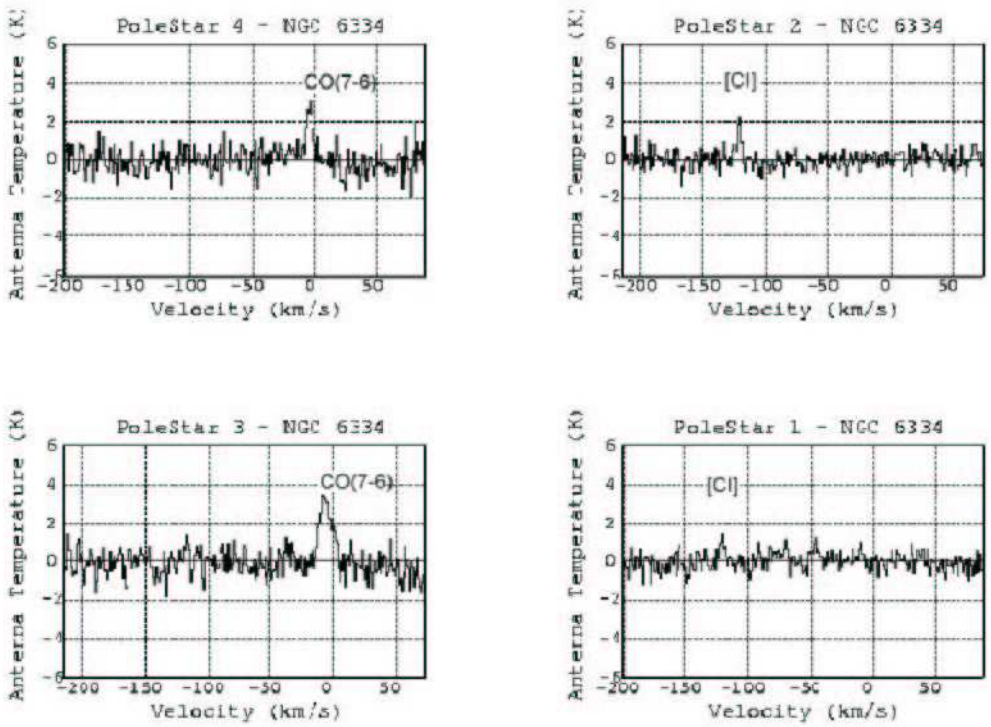

Figure 14: PoleStar first light spectra of NGC6334.
These data were taken during the Austral Summer of 2000. While the weather conditions were not optimal during this observation ($\tau_{810\ GHz}$~2.0), the receiver still did detect both [CI] $^3P_2$ and CO.

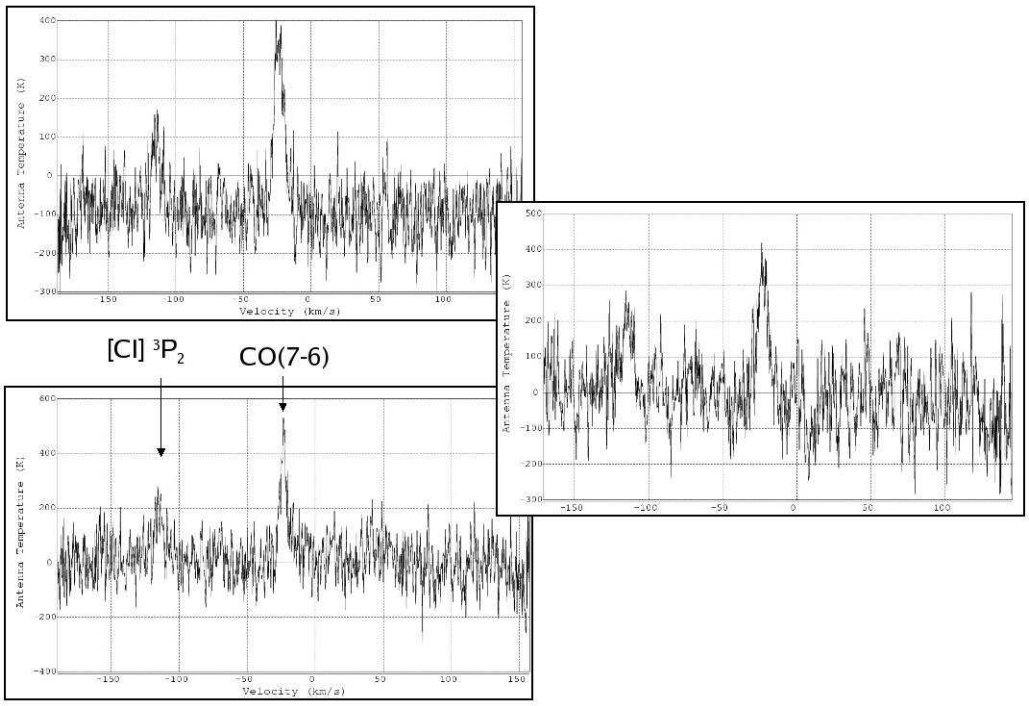

Figure 15: PoleStar spectra after upgrades.
Both [CI] and CO(7-6) are visible in all three spectra, taken during the Austral summer of 2002 toward NGC6334. Since no measurement of beam precession had been done, pointing is not known well for this observation. Figure courtesy Craig Kulesa.

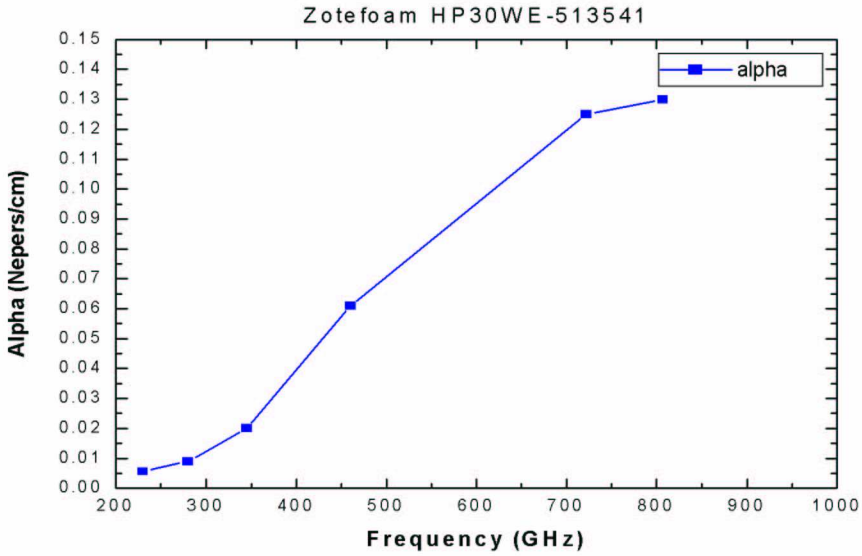

Figure 16: Zotefoam loss per unit length.
Loss (Np/cm) as a function of frequency for a 1” thick slab of Zotefoam PPA-30. These measurements were made by Jacob Kooi at the CSO using the CSO facility receivers with the Hot/Cold/Cold+Zotefoam method.

3. DESERT STAR: A 7 PIXEL 345 GHZ HETERODYNE ARRAY RECEIVER FOR THE HEINRICH HERTZ TELESCOPE

3.1 Introduction

While the standard for heterodyne receivers at millimeter and submillimeter-wave telescopes around the world is still a single pixel, many multibeam receivers are currently in use (BEARS (Sunada et al. 2000), CHAMP (Gusten 2000), SMART (Graf 2000), Pole-Star (Groppi et al. 2000) & HERA (Schuster et al. 2000)) and being developed (HARP-B (Dent 2000)). Given that ~55% of the time available at the HHT is suitable for 345 GHz observations, we have concentrated our array development for this atmospheric window. Array receivers can dramatically increase the speed of mapping, making difficult projects easier and bringing impossible projects into reach. SCUBA and SHARC revolutionized submillimeter continuum observing. Heterodyne arrays have the same promise for high resolution spectroscopy. Heterodyne focal plane arrays with modern, tunerless mixers can increase observing efficiency in imaging mode by more than an order of magnitude over the previous generation of single pixel receivers with tuners. DesertStar will increase imaging speed at the HHT by a factor of ~15 compared to the current MPIfR dual polarization 345 GHz receiver. For many projects, like the proposed HHT Galactic plane CO survey lead by John Bieging, this is enabling technology. Heterodyne arrays make the most efficient use of good weather, increasing the observing efficiency of telescopes even at sites with weather that is not optimal.

3.2 Mapping Speed

While it seems obvious that an array receiver will be faster than a single pixel receiver, the answer to the question is not straightforward. What is better, a fully optimized, dual polarization single pixel receiver or an array? For the mapping speed advantage of a small, single polarization array to be realized, the performance of each pixel in the array must be very close to the performance of an optimized single pixel instrument (this holds for array sizes of ~10 pixels or less). The ~60K receiver noise temperature of DesertSTAR will result in ~15 times faster mapping of large areas than the dual polarization 345 GHz receiver currently in use on the HHT. Compared to a fully optimized, dual polarization, single sideband receiver with a state of- the-art noise temperature, DesertSTAR should be ~4 times faster. Combined with the On-The-Fly mapping technique, we expect to increase observing throughput by a factor of ~100 compared to traditional position-switched maps made with a single pixel receiver. When OTF mode is used for both receivers, with the same number of offs per row, and with map sizes significantly larger than the array size of 108”, the gain in speed is simply

$$\frac{time_{array}}{time_{single}} = \frac{n_{pixels}}{n_{pol}} \cdot \left(\frac{t_{sys,single}}{t_{sys,array}} \right)^2$$

where n_{pol} is the number of polarizations in the single pixel receiver. This simple formula does not take into account single sideband operation, which can increase the complexity of the calculation significantly. Gains from Single Side Band (SSB) operation depend on the losses in the SSB filter, the temperature of the filter and sideband dump, and the atmo-

spheric quality at the time of observation. Notes in the ALMA memos series show that a lossless SSB filter with a 4K dump can improve the system temperature of a receiver by 20%-30%, but if the filter has appreciable loss, these advantages are quickly lessened (Jewell et al. 1997, Thompson et al. 1997, Lamb 2001). While we have designed a Martin-Pupplet single sideband filter with 40K optics and a 4K dump, we have chosen to omit it initially in favor of increased simplicity. Table 2 summarizes the On-The-Fly mapping speed performance of the facility MPIfR dual polarization receiver currently at the HHT, DesertStar, and the expected performance of the dual polarization 345 GHz channel of the HHT multifrequency system, now in development.

3.3 Atmospheric Conditions

With all the effort put into the development and construction of an array receiver, it should be used as much as possible. With this in mind, we chose the 345 GHz atmospheric window. This window exhibits ~75% transparency from 310-380 GHz, and offers a huge number of astrophysically important lines, as shown in Figure 17. A spectral survey by Groesbeck shows hundreds of lines in the tuning range, ranging from simple CO to extremely complicated organic molecules. Figure 18 shows a composite spectrum over the entire 345 GHz window (Groesbeck 1995). Hundreds of molecular lines are evident, and are useful in many areas of astronomy, from astrochemistry to the study of the ISM in external galaxies. In addition, weather at the HHT is friendly to 345 GHz observations. Figure 19 shows the cumulative atmospheric opacity distribution for the 1999 observing

season, measured by a 225 GHz tipping radiometer mounted on the HHT building three times per hour. The percentage of time per year with τ_{225} GHz<0.15 is ~55%, comparable with other sub-mm telescope sites, especially considering the HHT can observe 24 hours per day, while the Caltech Submillimeter Observatory and James Clerk Maxwell Telescope cannot observe during daylight hours.

3.4 Instrument Description

3.4.1 Overview

DesertSTAR was designed for use as a facility instrument for the Heinrich Hertz Telescope, located at 10,500 ft. on Mt. Graham in southeastern Arizona. The telescope is a 10m Cassegrain design with Carbon Fiber Reinforced Plastic (CFRP) primary reflector panels and backup structure. The quadrupod and the subreflector are also CFRP. The CFRP construction provides very good stiffness, plus the temperature stability necessary to operate 24 hours per day (Baars et al. 1999). The surface of the main reflector has an RMS roughness of ~13 μm, measured with holography. The HHT is currently the most accurate large radio telescope in existence. DesertSTAR will be mounted on the right Nasmyth platform, bolted directly to the telescope flange. Figure 20 is a photograph of DesertSTAR on the right Nasmyth flange of the HHT during an engineering run in June, 2003. The flange opening itself limits the maximum number of pixels. With the 2Fλ spacing of the pixels in DesertSTAR, the outer beams clear the flange at the 3ω level. The beams on the sky, as shown in Figure 21, are 22” FWHM, with 44” center-to-center spac-

ing, arranged in a close packed hexagonal arrangement. This configuration maximizes the number of beams through the telescope flange on the HHT, while still preserving ~20 dB isolation between pixels.

DesertSTAR uses fixed-backshort Superconductor-Insulator-Superconductor (SIS) mixers with a broadband waveguide probe. Instantaneous bandwidths of 2 GHz can be achieved over the entire 345 GHz atmospheric window. A cryostat with a Joule-Thompson (JT) mechanical refrigerator allows continuous operation and 1.8W of cooling capacity at 4K, and provides the needed temperature stability for low-noise operation. Local Oscillator (LO) distribution is accomplished with a novel phase grating that yields high efficiency and power uniformity in a hexagonally symmetric geometry. The computer controlled bias system is an evolution of a proven design that is simple, portable to any computer platform, and readily extensible to over 100 channels. It provides bias control of the mixers, IF amplifiers and magnets as well as monitoring of temperature and vacuum. It can be operated from any X-windows capable machine and writes an instrument status web page visible with any web browser. The 2 GHz Intermediate Frequency (IF) bandwidth allows the future addition of a wideband backend optimized for extragalactic observations, with ~1700 km/s of velocity coverage.

3.4.2 Optics

Given that an array receiver is already a very complicated system, we chose to make the optics of DesertSTAR as simple as possible. Experience with the PoleSTAR 810 GHz array at the AST/RO telescope on the South Pole has shown that in practice, complex optical circuits are difficult to implement in practice with array receivers. An example is the Martin-Pupplet interferometer, which can be used as a quasi-optical LO diplexer or single sideband filter. Even a 0.5 degree misalignment of a beam propagating through the interferometer will cause a 3 dB loss in coupling. With an array architecture based on individual mixers mounted in the focal plane, it is difficult to control the beam boresight to the required tolerances. Other arrays, like CHAMP (Gusten 2000) and SMART (Graf 2000) have gone through great pains to ensure alignment of optical components and mixers. We have chosen to eliminate all optics from the system that require extremely tight tolerances on mixer beam boresight, and minimize the number of lenses and mirrors. The beam from each diagonal horn is matched to the telescope with separate High Density Polyethylene (HDPE) lens mounted directly to the mixer housing, decreasing the chances of mixer squint due to horn-lens misalignment. The beams then reflect off a single, cold 45˚ flat mirror and directly illuminate the flat tertiary of the telescope. Most designs use a curved mirror to cross the beam bundle at the location of the vacuum window to minimize window size and then use another curved mirror to parallelize expanding beams. We chose to keep the beams parallel throughout at the cost of increased vacuum window size. A new material, ZoteFoam PPA-30, made it possible to construct a 4.5 in. clear aperture vacuum

window with extremely low loss and good vacuum properties. ZoteFoam PPA-30 is a closed-cell polyethylene foam blown with dry nitrogen gas. A 1” thick window 8” in diameter (1.75” glue surface, 4.5” clear aperture) is sufficient to hold vacuum with no other materials present, with acceptable deflection under vacuum, and no noticeable helium permeability or outgassing problems. Figure 16 shows a measurement of the loss of a 1” thick slab of ZoteFoam PPA-30 as measured by Jacob Kooi at the Caltech Submillimeter Observatory. While loss is significant at high frequencies, the performance from 300-400 GHz is quite good. The transmission of the DesertStar window is 96%-98% from 300-400 GHz, adding noise of ~10K. This is about twice the added noise of a 0.5 mil Mylar window or a Polyethylene coated crystalline quartz window. Zotefoam was chosen as the best option, since Mylar cannot span a window opening that large, and a quartz window would cost more than $8000. It has been in use as a window material in an instrument at the South Pole (AKBAR) for over two years with no reliability problems (Kuo et al. 2002).

3.4.3 Local Oscillator

Local oscillator power delivery is another difficult problem for array receivers. LO power must be efficiently and equally divided into each pixel. While many waveguide techniques are available, they are complicated, difficult to implement and lossy at high frequencies. Quasi-optical techniques can also be lossy and complicated, with difficult alignment issues. Recent work by the Cologne and MPIfR groups in Germany have lead to the

development of both transmissive and reflective phase gratings that form multiple LO beams from a single input beam through diffraction. Our LO distribution system uses a novel reflective grating design from the University of Cologne (Heyminck et al. 1998). This design creates a 7 beam array with hexagonal symmetry with 80% efficiency and is superimposed on a parabolic mirror. This optic then acts as a collimating mirror for the LO beam, and also forms the 7 beam array. The phase grating has an operational bandwidth of ~10% centered on 345 GHz. A simple Mylar beamsplitter acts as the LO diplexer. Figure 22 is a cutaway CAD drawing of the LO optics and receiver optics. Figure 23 shows the measured beam pattern of the LO phase grating at 345 GHz, with insets at other frequencies. This measurement was made at the University of Cologne by Urs Graf with a facility 350 GHz receiver system.

3.4.4 Cryogenics

DesertSTAR was designed to allow for cooled optics and have room for a second sub-array. To achieve these goals, we designed a cryostat, with a 28” cold plate, a large 4K volume for cold optics, and a large 4K cooling capacity. The cryocooler is based on the proven NRAO JT refrigerator, used for the facility receivers at the NRAO 12m telescope. The unit has a 180W capacity at 77K, a 1.8W capacity at 4K, a 20K helium precooler stage and a self-cleaning JT expansion valve. The refrigerator is mated to a commercial Balzers cold head, and driven by a custom NRAO compressor. Cooldown tests show stable 4K operation is achieved in ~13 hours. In addition, we have used a resistive heater on the

4K cold plate to measure a cooling capacity of 1.44W (Figure 24). This measurement was made with full infrared (IR) loading on the cold plate. Calculations show that the total heat load including amps and infrared loading is 0.9W. The IR heat load is dumped to the 77K shield with a Gore-Tex GR IR filter. Figure 25 shows an image of the receiver's JT refrigerator outside the cryostat during service. Since cryogenic testing began in 2000, we have experienced no failures of the cryogenic system. Table 3 summarizes typical operating temperatures for a variety of points in the receiver.

3.4.5 Mixers and Cold Electronics

DesertSTAR uses 7 independent single ended mixers, each mounted together with a HDPE lens, isolator and amplifier in a modular rocket, which is cooled by the JT refrigerator via a cold finger. The mixers were designed in collaboration with Gopal Narayanan at the University of Massachusetts and Jacob Kooi at Caltech. The mixers were machined at UMass, and the SIS junctions fabricated at the University of Virginia by Art Lichtenberger.The simple, single ended waveguide design uses a diagonal feedhorn to couple the telescope beam through a multi section impedance transformer to half height waveguide. The waveguide backshort is fixed and there is no E-plane tuner. The cross-guide probe uses the proven suspended stripline design of Blundell & Tong (Blundell et al. 1995). The Nb SIS junctions were designed with an on-chip tuning structure for low return loss across the atmospheric window, permitting a fixed backshort. High Frequency Structure Simulator (HFSS) simulations of the junction return loss assuming a 40-j20 Ω waveguide embed-

ding impedance are shown in Figure 26. Junction performance was also simulated using the embedding impedance determined from scale model measurements, with similar qualitative performance. The optimum backshort position was also determined via HFSS modeling. The diagonal horn was chosen since it could be readily made with the UMass micro milling machine. While their coupling to the fundamental Gaussian mode is less than a scalar corrugated horn, diagonal horns still provide adequate broadband performance at a fraction of the cost (Johansson et al. 1992). Figure 27 shows an Agilent HFSS simulation of the diagonal horn. The beam pattern is gaussian, but the diagonal horn has about 14% crosspolarization, lowering it's efficiency when used in combination with a linearly polarized input signal. A 4-wire bias tee is mounted in the mixer block, and monitors junction voltage and current with a precision current-sense resistor. Figure 28 is a Agilent ADS simulation of the performance of the IF matching network. The plot shows return loss, insertion loss, and leakage out the bias terminals. Return loss is better than -20 dB from 4-6 GHz and leakage is less than -40 dB. Insertion loss is a fraction of a dB. The mixer produces a 4-6 GHz IF, and is connected via a Pamtech cryogenic ferrite isolator to a Miteq 4-6 GHz cryogenic low noise amplifier (LNA). Losses of the bias tee and isolator are less than 1.5dB from 4-6 GHz, as measured via vector network analyzer. The Miteq amplifiers have 27 dB gain, less than 1 dB passband ripple, 30 mW power dissipation and a measured noise temperature of 7K at 4K operating temperature. The amplifiers require only a single, unipolar 0.6V bias, greatly simplifying the wiring and bias supplies. A simple superconducting coil electromagnet provides the necessary magnetic flux to minimize Josephson noise with soft iron field concentrators embedded in the mixer block. Figure 29 is a close-

up photograph of a prototype mixer, showing the diagonal horn, waveguide and junction channel. Figure 30 shows the mixer array inside the cryostat with 3 mixers installed.

3.4.6 DC Electronics

Array receivers present a new challenge to the DC bias electronics necessary to provide power to the SIS junctions, magnets and LNAs. Simple boxes with manual controls are far too cumbersome to implement with a large number of pixels. To solve this problem, we have developed a computer controlled bias system. The electronics are based on the design used with single pixel receivers at the HHT, but replace manual potentiometers with digital potentiometers that communicate via the Philips I^2C bus. Each bias card contains 4 channels of electronics. The DesertSTAR system uses two SIS bias cards. The LNA and magnet bias system each use 4 cards. Two analog multiplexer cards select monitor signals. Both the I^2C input from the control computer and the DC monitor voltage outputs are optically isolated, eliminating any electrical connection between the bias rack and computer. A simple data-IO card in the computer digitizes the monitor signals. The Linux control computer runs a graphical interface written in C/GTK+, which provides a user-friendly interface to the bias parameters. Cryogenic, vacuum and LO status are also available on-screen. The X-windows interface allows the receiver to be optimized from any X-windows capable machine, which will allow the instrument builders to diagnose and fix tuning problems remotely. The software has been written in a hardware independent man-

ner, allowing easy hardware changes with a minimum of new code development. Figure 31 is a screenshot of the DesertStar software interface.

3.4.7 Backends

The HHT is currently upgrading the telescope control system and backend electronics for all receivers. As a part of this effort, a modern, flexible filterbank spectrometer with a 2x1 GHz bandwidth and 1 MHz resolution is being constructed. The IF processor for this backend can support 8x256 MHz IF sub-bands for use with DesertSTAR. This bandwidth and velocity resolution is adequate for a large variety galactic astronomy projects. The filterbank should provide extremely high stability without the platforming problems often associated with hybrid correlators. In the future, we hope to obtain a 7x2 GHz digital autocorrelator. This will allow extragalactic observing with the full 2 GHz IF bandwidth of DesertSTAR with 8 MHz resolution. The flexibility of the correlator also allows for widely variable resolution via an adjustable system clock. During the fall 2003 season, we will operate the receiver in three pixel mode using the existing facility acousto-optical spectrometers and chirp transform spectrometers. The existing IF processor system for the new HHT multifrequency receiver will be modified to accept three simultaneous 4.6 GHz IF channels.

3.5 Receiver Performance

3.5.1 Preliminary Results

Initial tests of a single array mixer/IF chain have been conducted in an IR Laboratories $LN_2/^4He$ cryostat. The test system uses a 0.5 mil Mylar LO diplexer, a 1.0 mil Mylar cryostat vacuum window, and a single layer of Zitex A for IR filtering. The mixer beam is launched with an unmatched HDPE lens mounted directly to the mixer housing. The first prototype mixer has a very long backshort channel, that is then shortened to the proper length with aluminum shim stock. This allows some adjustability of the backshort position. All other mixers were fabricated with a machined, non-adjustable backshort. A room temperature total power box and a Hewlett-Packard power detector were used for the Y-factor measurements. The bias control system interrogates the output of this meter to allow total power vs. bias voltage sweeps. Before mounting a device in the mixer block, we tested ~20 devices using a dipstick inserted into a liquid helium storage dewar. Figure 32 shows the I-V sweeps of 4 representative devices. The noise in the Josephson region is due to noise pickup in the test setup, and is not a characteristic of the devices themselves. Of the ~20 devices tested, only 3 were nonfunctional, and the remaining devices appeared to be virtually identical. The device mounted in the test block was randomly selected from the good devices.

3.5.1.1 Test Receiver Performance

Figure 33 shows a pumped I-V curve of the test mixer, along with hot and cold total power curves. The bias system uses the slope of the supercurrent at 0V to measure the contact resistance, and then remove it from the I-V curve. We measured R_n~48.5 Ω, a leakage current of ~3 μA and a transition voltage of ~2.3 mV. Optimum bias voltage for the highest Y-factor was ~1.6 mV. Uncorrected receiver noise temperatures as a function of LO frequency are plotted in Figure 34. From the waveguide probe simulations shown in Figure 26, we would expect T_{rx} to remain fairly constant from ~300 GHz to ~390 GHz. Preliminary measurements indicate receiver temperatures between ~55K and ~65K across the available band, with fairly flat response, as shown in figure 20. These are uncorrected noise temperatures, and include the losses of the LO diplexer, window and unmatched lens, along with noise from the IF chain. At this bias point, we measured total power stability to be better than 0.5% over 10 minutes. Figure 35 shows the 4-6 GHz IF bandpass with a hot and cold load. The Y factor is approximately constant across the entire passband. The LO source used in the test was unable to tune below 326 GHz or above 356 GHz, so we could not measure the receiver temperature over the full band of the waveguide probe.

3.5.2 Instrument Performance Characterization

After characterizing the performance of a single mixer in the test system, we installed the prototype mixer, and two additional mixers with fixed, machined backshorts

into the JT cryostat. We repeated the same tests done in the test setup, and found that the mixers behaved identically, but with receiver noise temperatures of 60-70K. It is not uncommon for the noise of a mixer in an array dewar to be slightly higher than in a highly optimized single pixel test system. We believe that losses in the cryostat window material and IF losses in the long runs of semi-rigid coaxial cable are responsible for the increase in noise temperature. We measured the loss of the window material by inserting a slab of ZoteFoam in the beam and observing the change in Y-factor. We found that the ZoteFoam contributed ~5K to the receiver noise temperature.

3.5.2.1 Stability Analysis

We performed an Allan variance stability analysis of the receiver to determine if microphonics from the large Balzers cryo-head would negatively effect receiver stability. We used a Hewlett-Packard power meter, sampled every 50 ms with a data acquisition card in the computer control system. Data was taken for more than 1.5 hours, and folded every 5 minutes to lower the noise due to the short integration time. We measured the total power over the entire 4-6 GHz IF for this test, and then scale the result to a 100 MHz post-detection bandwidth, since we did not have a narrow-band 5 GHz center frequency filter on hand. The data were analyzed following Kooi et al. (2000), with the help of an algorithm from Narayanan (2003). We assume a power law noise spectrum proportional to t^2. Then the Allan time scales like

$$T_A \propto B_{IF}^{-\frac{1}{2}}$$

The results in Figure 36 show an Allen variance time of ~3s for a 100 MHz bandwidth. This translates to an Allan variance time of ~30s with a 1 MHz post detection bandwidth. This stability time is adequate for all observing modes at the HHT.

3.5.2.2 Beam Pattern Measurement

Using a computer controlled XY stage system, we measured E and H plane cuts of the receiver beam pattern. The source was a liquid nitrogen cold load behind a sheet of room temperature absorber. A small hole in the absorber created a strong, negative source which could be detected using a lock-in amplifier and room temperature chopper wheel. The 3cm source size allowed adequate sampling of the receiver beam, and provided sufficient signal. Several scans were co-added and then fit with a 5 component gaussian. Results showed the beam to be gaussian in shape, but the beam was more broad and elliptical than expected. The horn lenses were designed based upon the analytical prediction of the horn's emergent beam (Johansson et al. 1992). However, our later HFSS simulations show the actual horn beam to be wider than predicted. The over illumination of the lens results in a emergent beam 15% too broad. We are currently redesigning the lens mounts to compensate for this effect. Figure 37 shows the E and H plane cut data as well as the fitted beam patterns. Note that these patterns are measured after the mixer lenses, and are therefore much narrower than the beam emergent directly from the diagonal horn as shown in Figure 28.

3.6 Telescope Performance and Initial Results

In early June, 2003 DesertStar was taken to the HHT for a 6 day engineering run. The goal was to identify areas of difficulty in using the receiver on the telescope, and to perform as many performance tests and verifications of the central mixer as possible. Overall, the results were good with some minor disappointments. Initial installation and cooldown were trouble free, but the receiver's mount proved to be inadequate. The weight of the receiver caused the mount to deform under load, and it was obvious that the mount was not rigid enough to prevent the receiver oscillating due to the cold-head cycle. The mount was reinforced as a stop-gap measure, and we continued to align the receiver to the telescope. Within two days, we had the central beam of the array on the sky, and had easily achieved receiver noise temperatures of ~90K. Measurements with a laser level proved the cryostat was indeed oscillating with a peak to peak amplitude of more than 40." This oscillation prevented us from making fine pointing or focus measurements. We used spectra and maps from extended regions to coarsely point the telescope. On centrally concentrated sources, peak line temperatures were diluted since the receiver beam was not on-source for all the integration time. Spectra were obtained from a variety of sources including IRAS16293, IRC+10216, DR21, CepA and S140. This data was used to verify the proper operation of the receiver system. Representative spectra and maps are shown in Figure 38 and Figure 39. We also measured the telescope's beam coupling efficiency to the moon,

η_{moon}. Calculation of the η_{moon} is essentially identical to the calculation of main beam efficiency with the assumption that the source size is large:

$$\eta_{mb} = \frac{T_A^*}{T_{source}}\left[1 - e^{\left(-\left(\frac{\theta_{beam}}{\theta_{source}}\right)^2 \ln(2)\right)}\right]^{-1}$$

The term in the square brackets goes to 1 with the above assumption.

$$T_A^* = T_{Hot} \cdot \frac{V_{Moon} - V_{Off}}{V_{Hot} - V_{Off}}$$

where T_{Hot} is the temperature of the ambient load, V_{moon} is the total power voltage on the moon, V_{Off} is the total power voltage on sky, and V_{Hot} is the total power voltage on the ambient load. Assuming a 105K temperature for the new moon, we calculated a moon efficiency of 78%, which is not an unrealistic number taking into account the error in the mixer lens illumination. The 40” pointing oscillation due to the movement of the instrument mount prevented us from performing measurements of the main beam efficiency. Since the engineering run, we have constructed a new, much stiffer instrument mount,

3.7 Summary

We have completed the first phase of constructing and testing a 345 GHz heterodyne array receiver for use on the Heinrich Hertz Telescope on Mt. Graham in Arizona. The instrument uses fixed backshort, suspended stripline SIS mixers with 2 GHz IF bandwidth. Cooling is provided by a high capacity closed cycle refrigerator in a large, expandable cryostat. We have demonstrated proper operation of the cryogenic system and computer con-

trolled bias system. Preliminary measurements indicate the prototype array mixer can provide uncorrected receiver noise temperatures of ~60K-70K from 326-356 GHz. Performance has been verified in the JT cryostat with 3 mixers, and the instrument has had a engineering run on the HHT, where it successfully collected data. The instrument will go into regular operation on the HHT in October 2003 with 3 pixels. The remaining 4 mixers will be added to the system in the summer of 2004, bringing the array up to its full compliment of 7 pixels. DesertStar is the first operational 345 GHz array receiver.

	MPIfR 345 GHz	**DesertStar**	**HHT Multi-frequency**
$\mathbf{T_{rx}}$	130 K	60K	60K (expected)
$\mathbf{n_{beams}}$	1	7	1
$\mathbf{n_{pol}}$	2	1	2
Relative OTF map speed	1	16.4	4.7 (expected)

Table 2: Relative OTF mapping speed for current and future HHT receivers.

Location	**Temperature**
JT Cold Stage	3.8K
Mixer Plate	3.9K
1^{st} stage heat exchanger	36K
2^{nd} stage heat exchanger	8.5K
Radiation shield	42K

Table 3: Typical stable operating temperatures for DesertStar

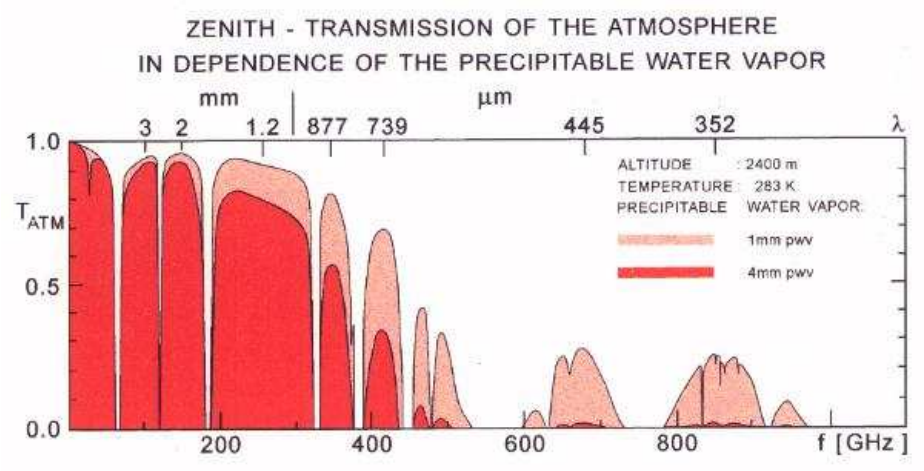

Figure 17: Submillimeter atmospheric transmission vs. frequency. The 345 GHz atmospheric window has the highest transmission of any sub-mm window, especially in marginal weather.

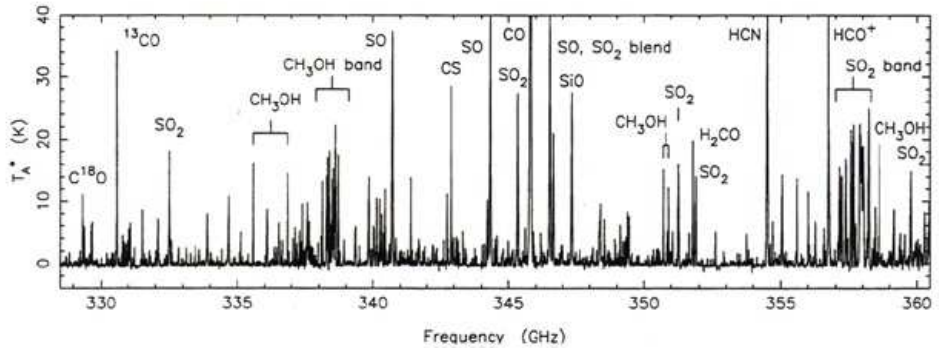

Figure 18: A spectral line survey of the 345 GHz atmospheric window. This plot, from Groesbeck, shows the large number of astrophysically important lines in this spectral region.

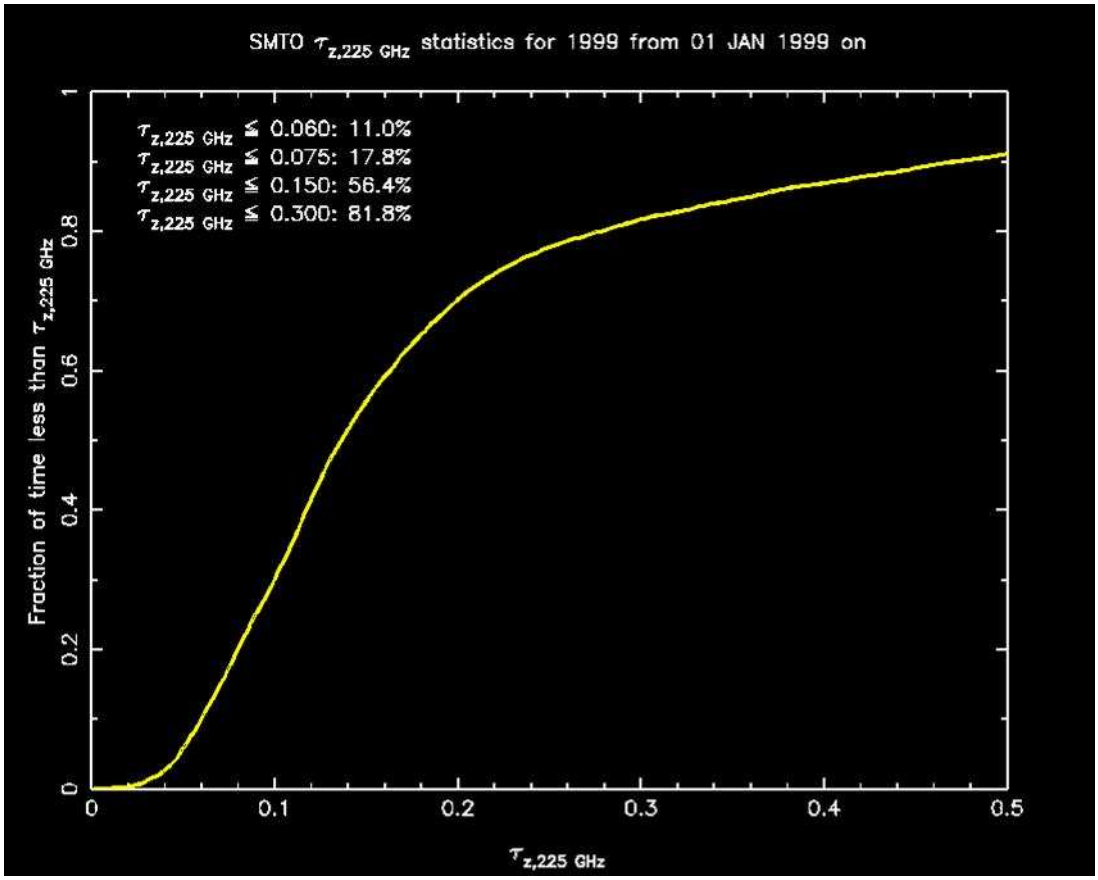

Figure 19: Cumulative atmospheric opacity at the HHT.
The opacity, measured by a tipping radiometer at 225 GHz, is less than 0.15 (the threshold for effective observing at 350 GHz) about 55% of the time.

Figure 20: A picture of DesertStar mounted on the HHT.
This photograph was taken during an engineering run in June, 2003.

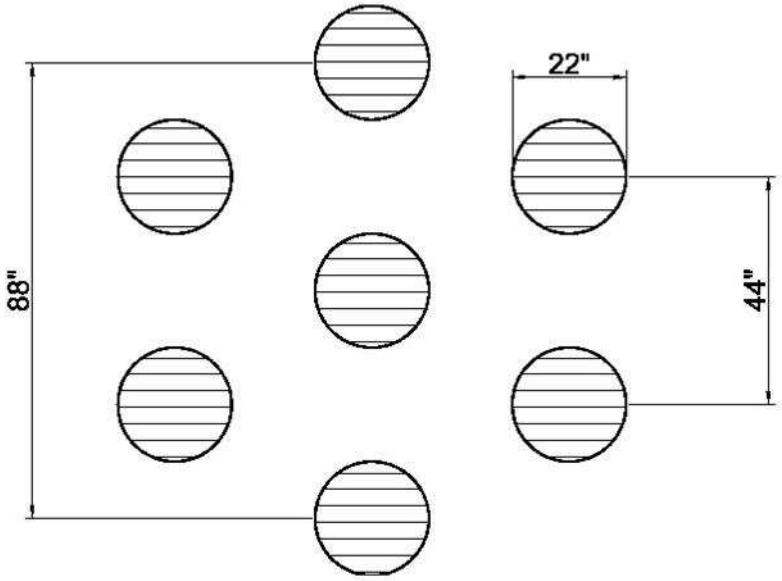

Figure 21: The beam footprint of DesertStar on the HHT.
Each beam is 22” at FWHM with 44” spacing. The 2Fλ spacing gives better than 20dB isolation between pixels.

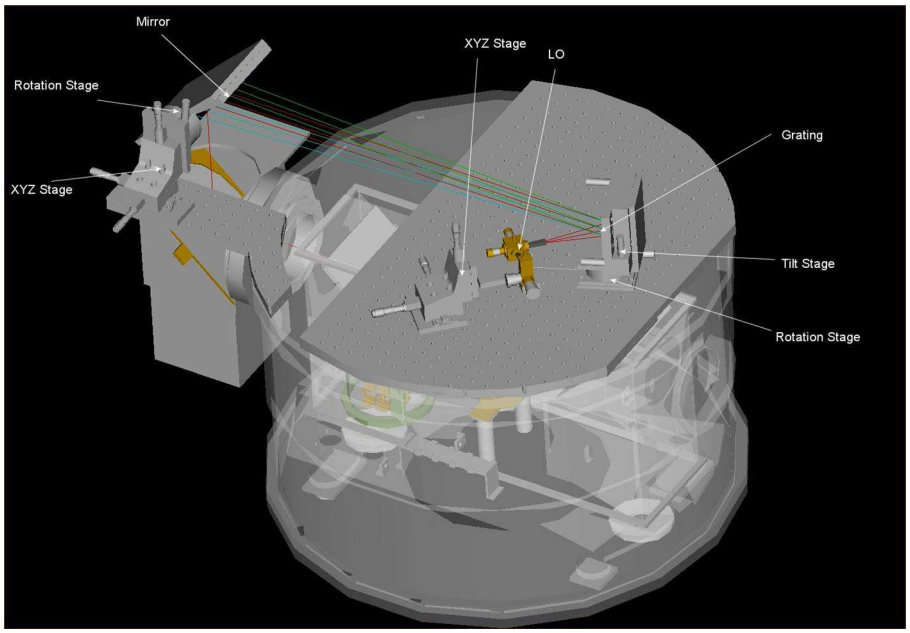

Figure 22: A cutaway CAD drawing of DesertStar.
This shows the LO distribution optics, mixer array and internal flat mirror. Since the beam bundle is not crossed anywhere in the system, optics complexity is minimized. Figure courtesy Dathon Golish.

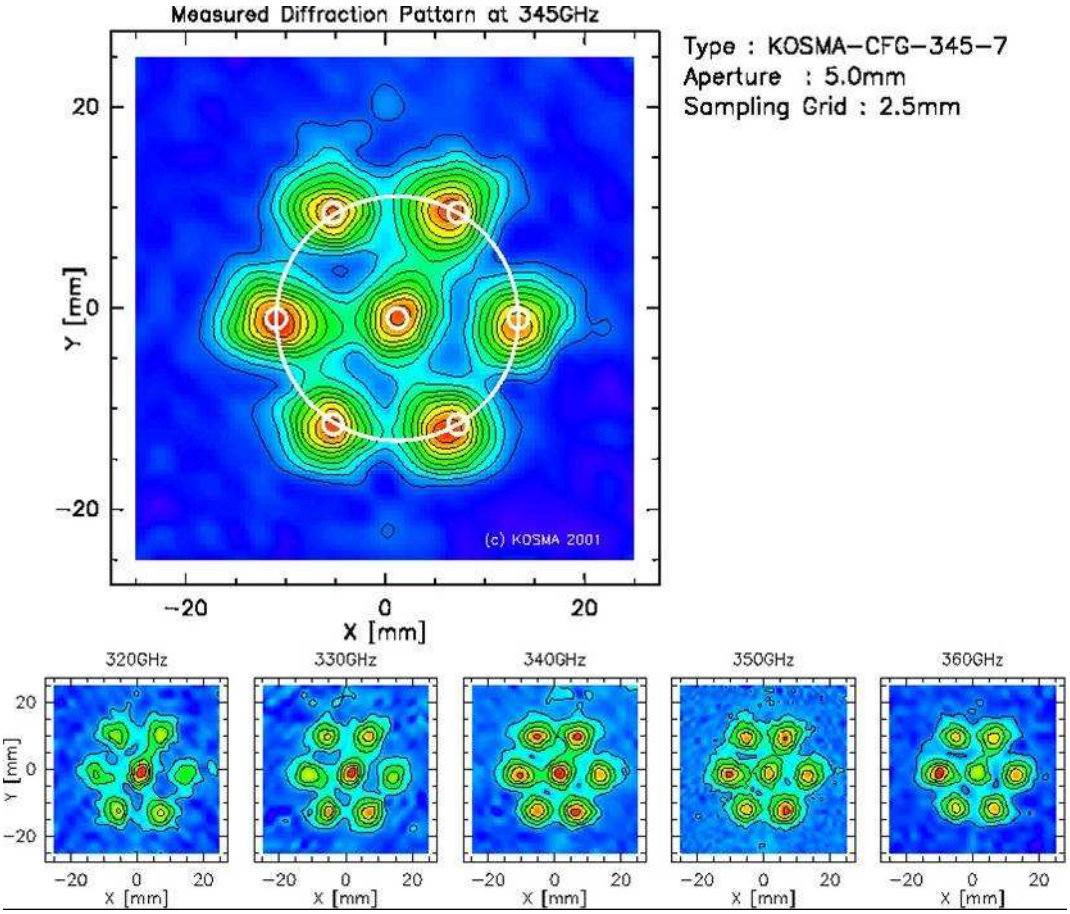

Figure 23: A beam pattern map of the DesertStar LO phase grating. Pattern measured by Urs Graf at the University of Cologne. At 345 GHz, LO power is extremely well balanced. The effective bandwidth of the grating is ~10%, after which LO power is unbalanced by more than 3 dB.

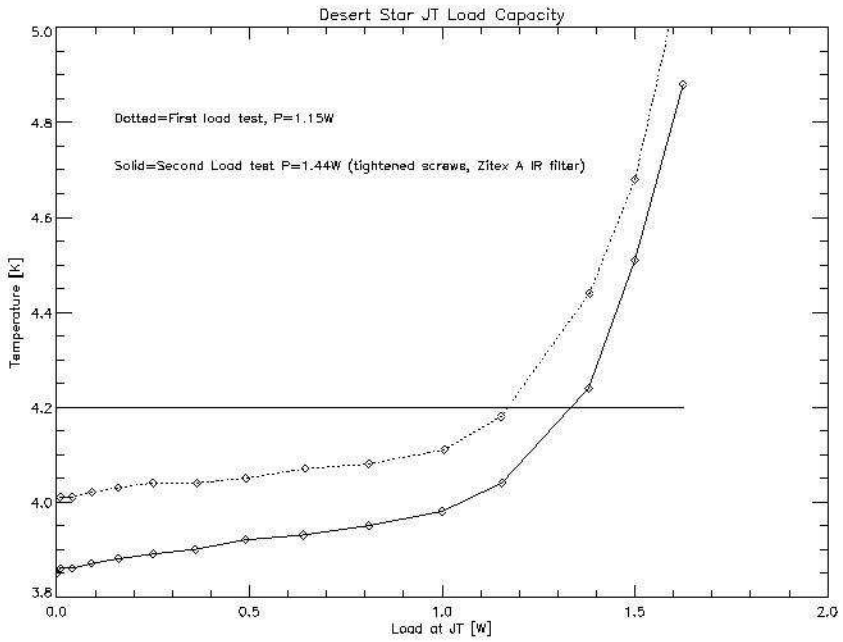

Figure 24: JT refrigerator temperature as a function of thermal load. This measurement was done with full IR loading on the system. The upper curve is the first cooldown, the lower after tightening all fasteners in the cryogenic system. Measured load is 1.44W at 4.2 K.

Figure 25: A photo of the DesertStar JT refrigerator. The small gold cylinder at the top of the refrigerator is the helium collection pot.

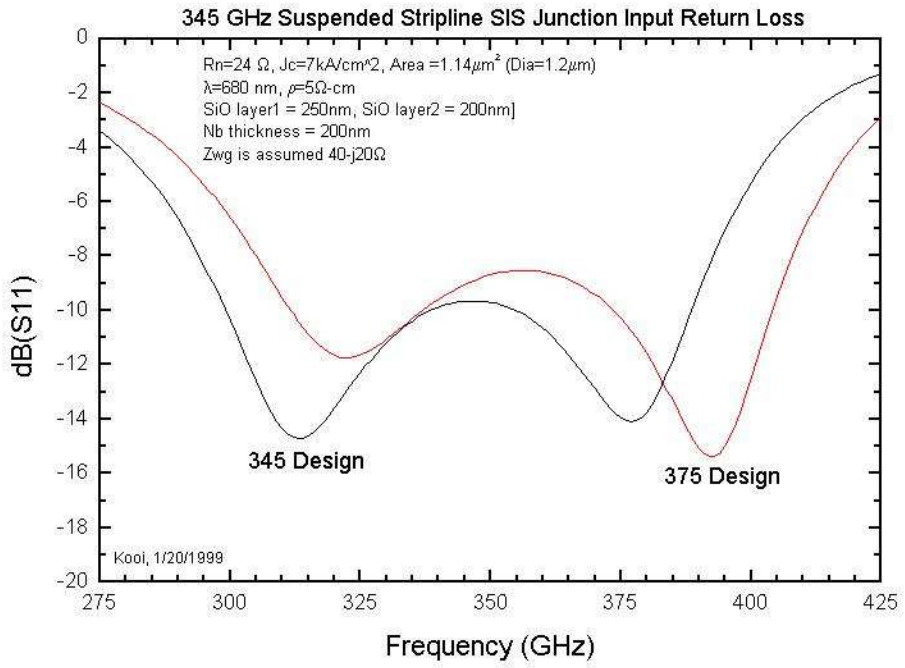

Figure 26: HFSS simulation of the SIS junction input return loss.
The probe offers good performance from 300-390 GHz. The qualitative shape is similar using a Supermix simulation of the device impedance. Simulation & figure by Jacob Kooi.

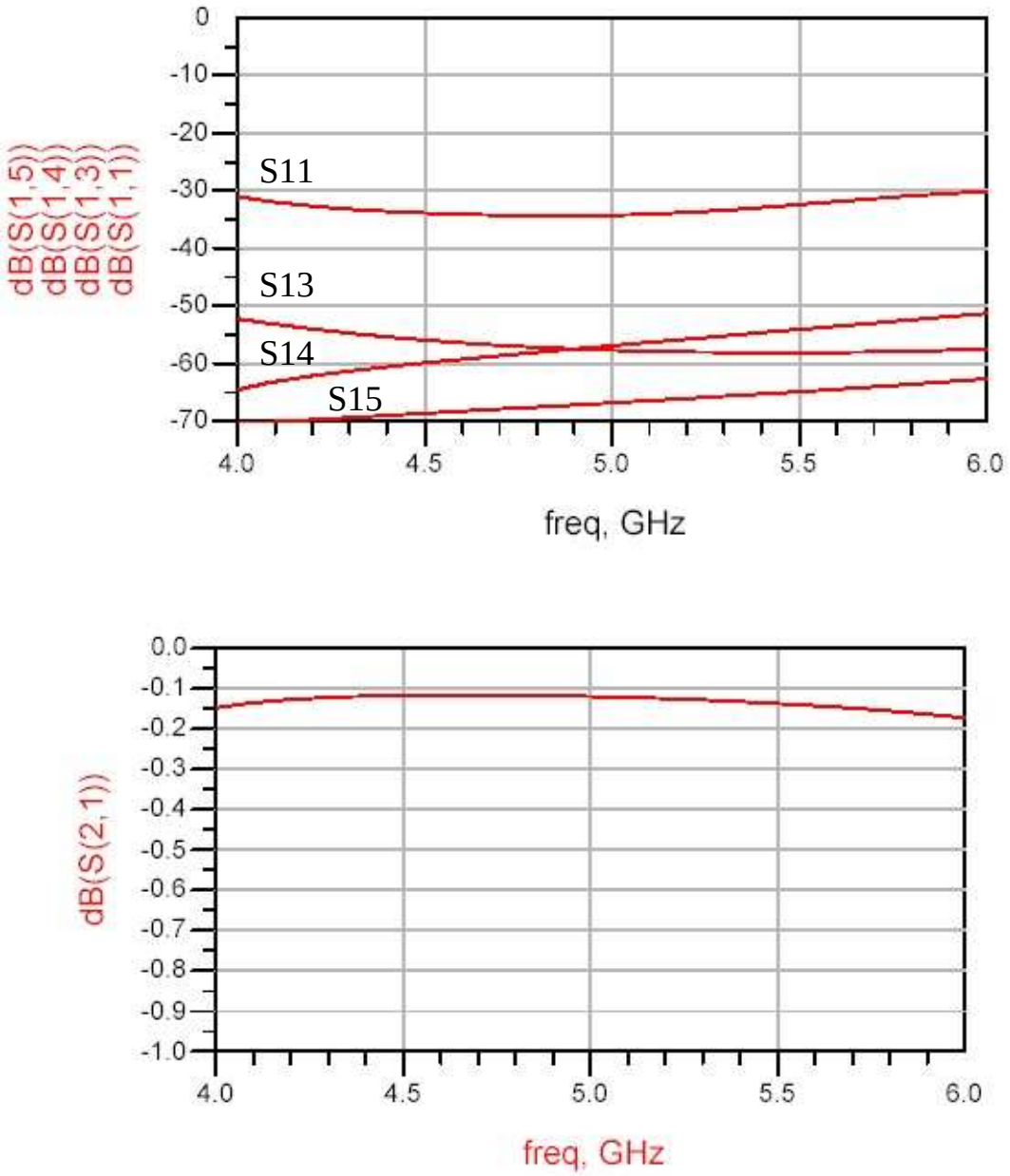

Figure 27: Agilent ADS simulation of the DesertStar bias tee.
The top plot shows return loss less than -30 dB across the band, and leakage out the bias terminals less than -50 dB across the band. Bottom is the insertion loss, about -0.1 dB.

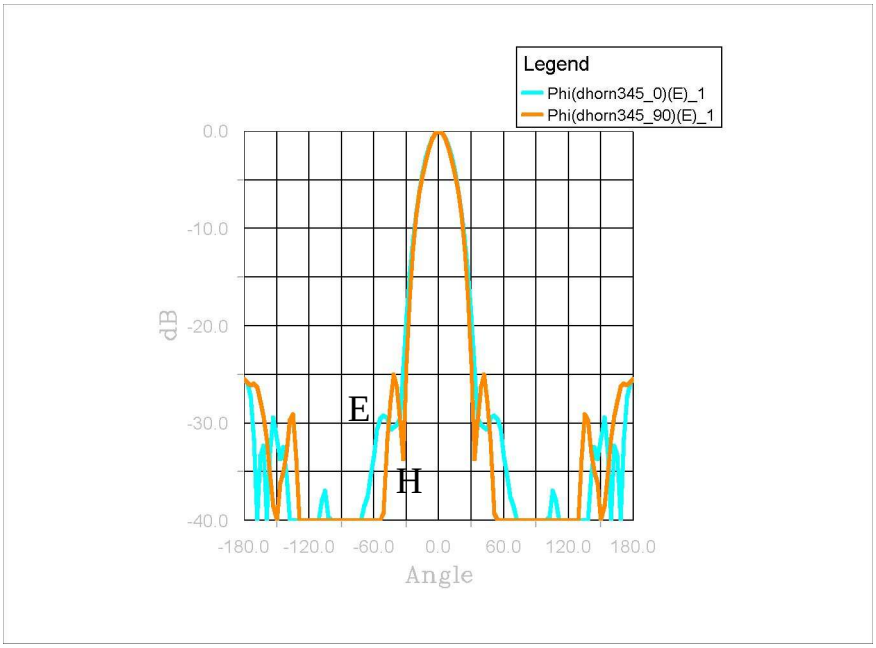

Figure 28: Agilent HFSS simulation of the DesertStar diagonal feedhorn.
E plane and H plane cuts are shown. The beampattern has side-lobes of about -30 dB, and is quite gaussian, but has ~10% cross-polarization. Figure & simulation courtesy Dathon Golish.

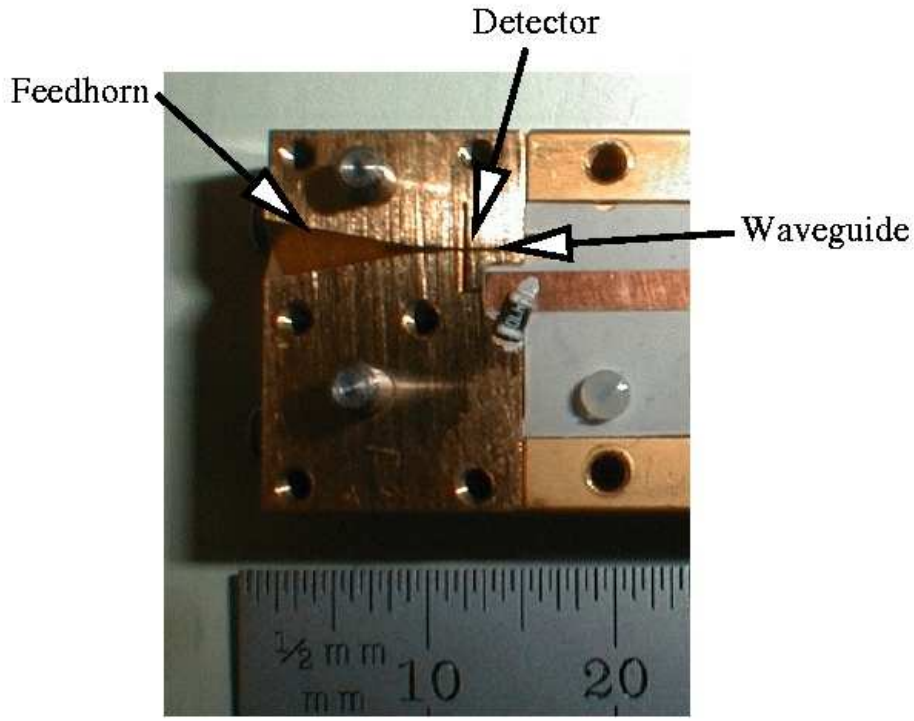

Figure 29: A close-up picture of a prototype mixer block.
The backshort is machined to the end of the block, and is then filled with aluminum shim stock to allow for some adjustability on the prototype mixers.

Figure 30: A photograph of three mixers installed in the JT cryostat.

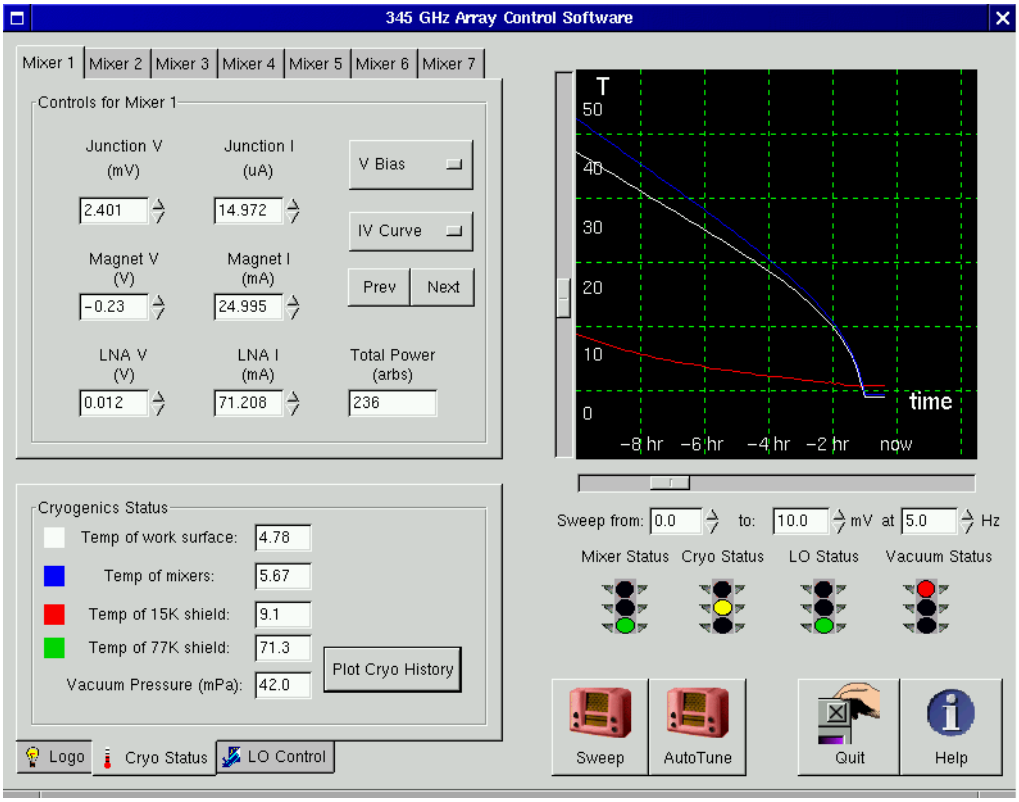

Figure 31: A screenshot of the DesertStar control software.
The interface allows the user to monitor and modify all receiver parameters including cryogenic and vacuum data, either at the control computer or from a remote terminal.

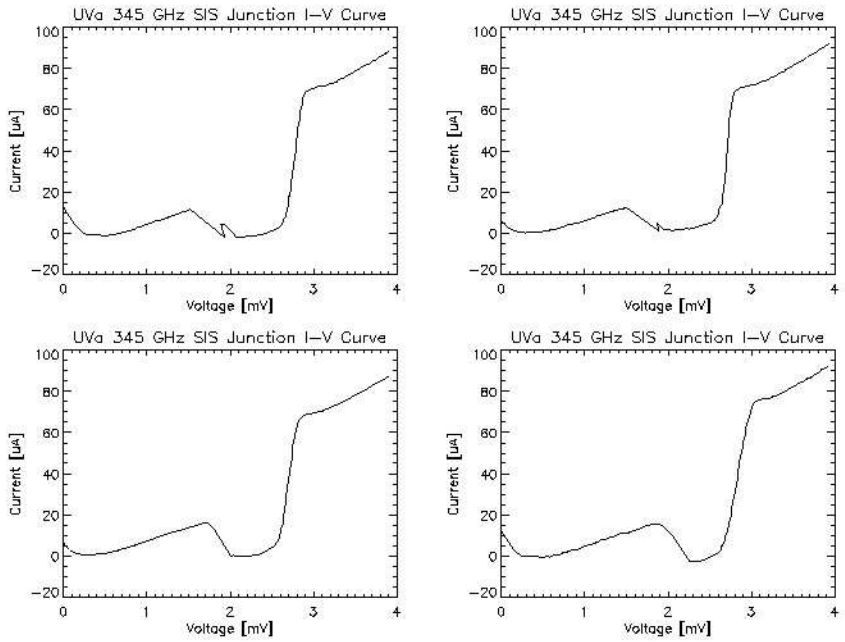

Figure 32: IV curves from 4 SIS junctions, measured via dipstick.
The curves are remarkably similar for randomly selected junctions. The current between 1 and 2 mV is due to noise pickup in the test setup, and is not a characteristic of the devices themselves.

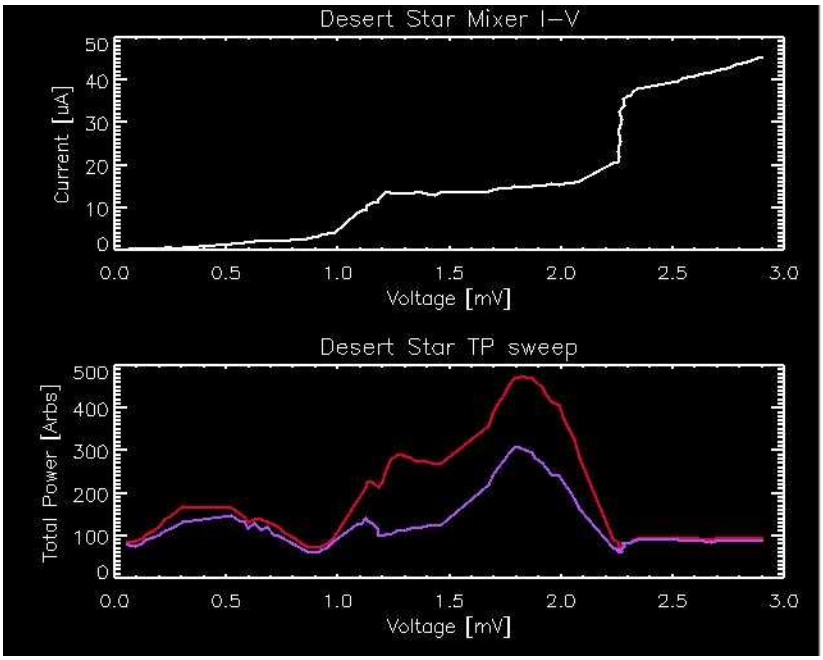

Figure 33: Representative IV and hot/cold total power curves.

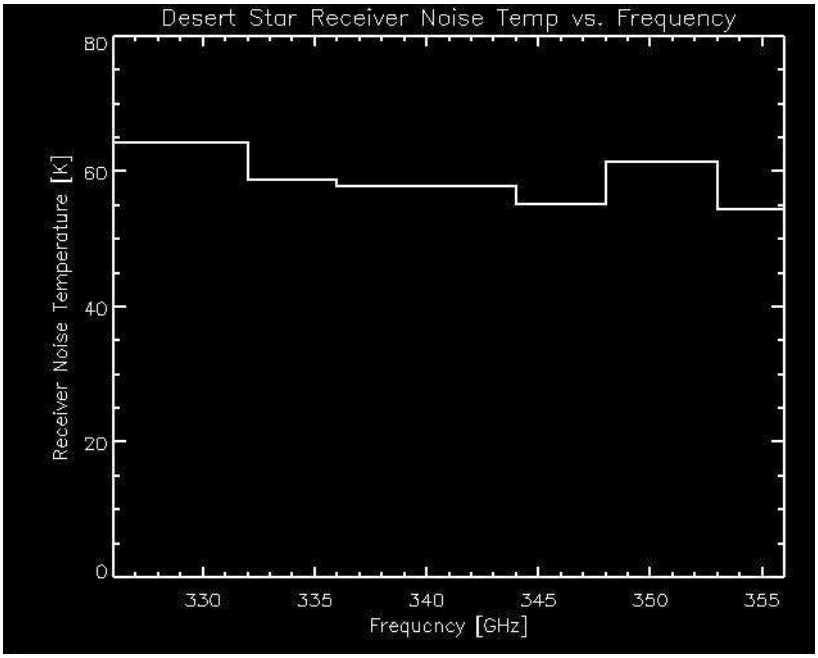

Figure 34: Receiver noise temperature vs. LO frequency. Noise temperature is relatively flat from 326-356 GHz, as expected from simulation.

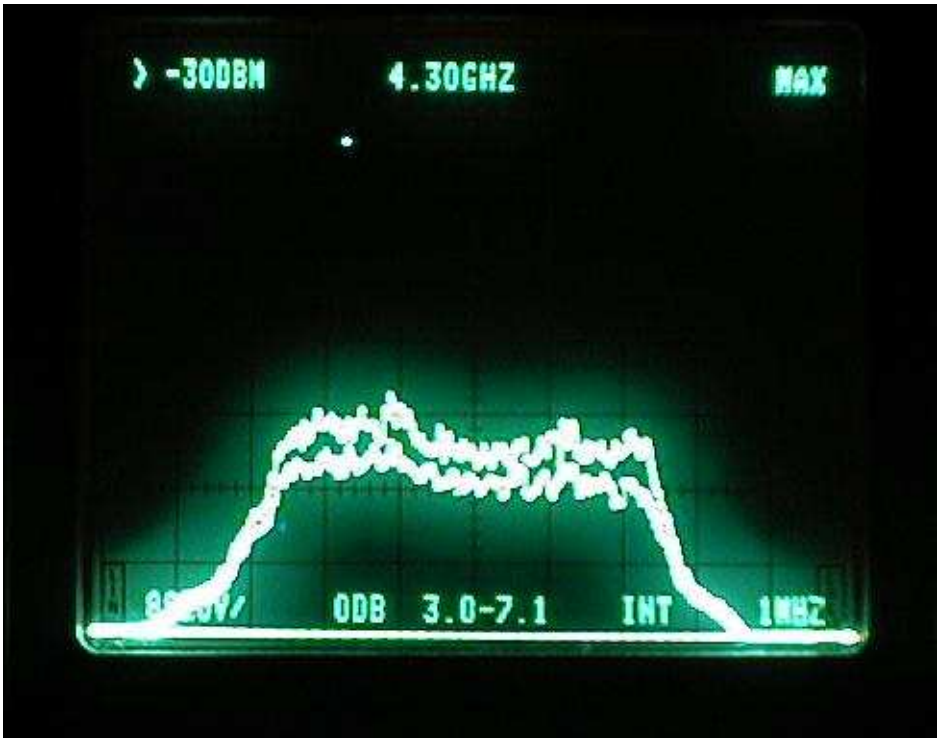

Figure 35: Hot/Cold IF bandpasses for Mixer 1.

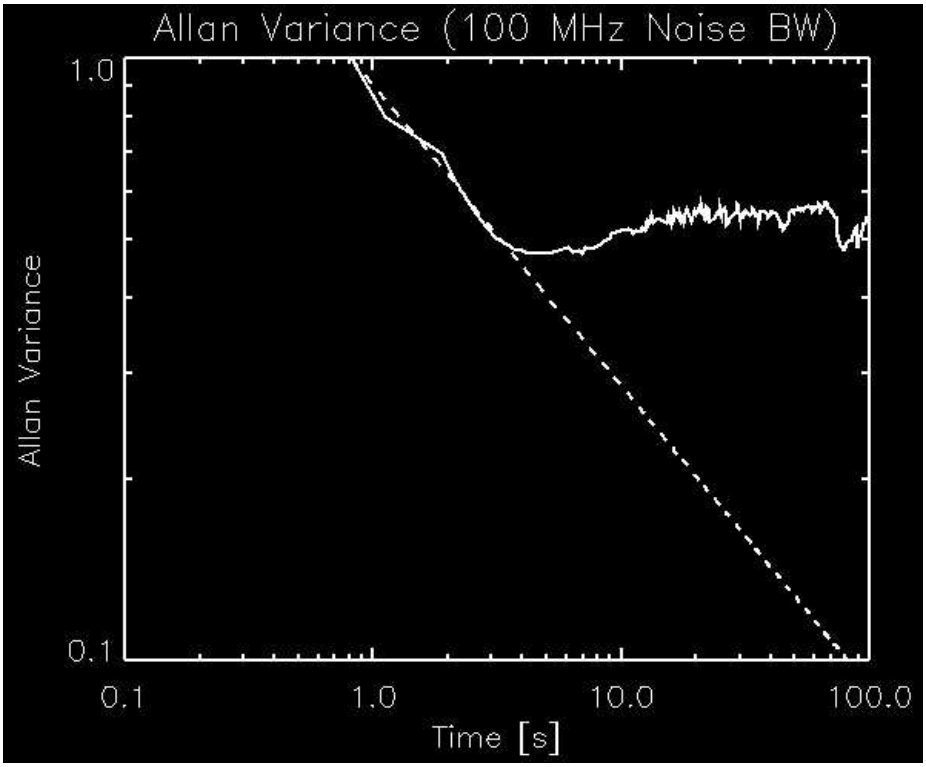

Figure 36: An Allan variance plot for mixer 1.
This result has been scaled to 100 MHz post-detection bandwidth from the measured data taken with a 2 GHz post-detection bandwidth. The dotted line represents a $t^{1/2}$ decrease in noise with time as theoretically expected.

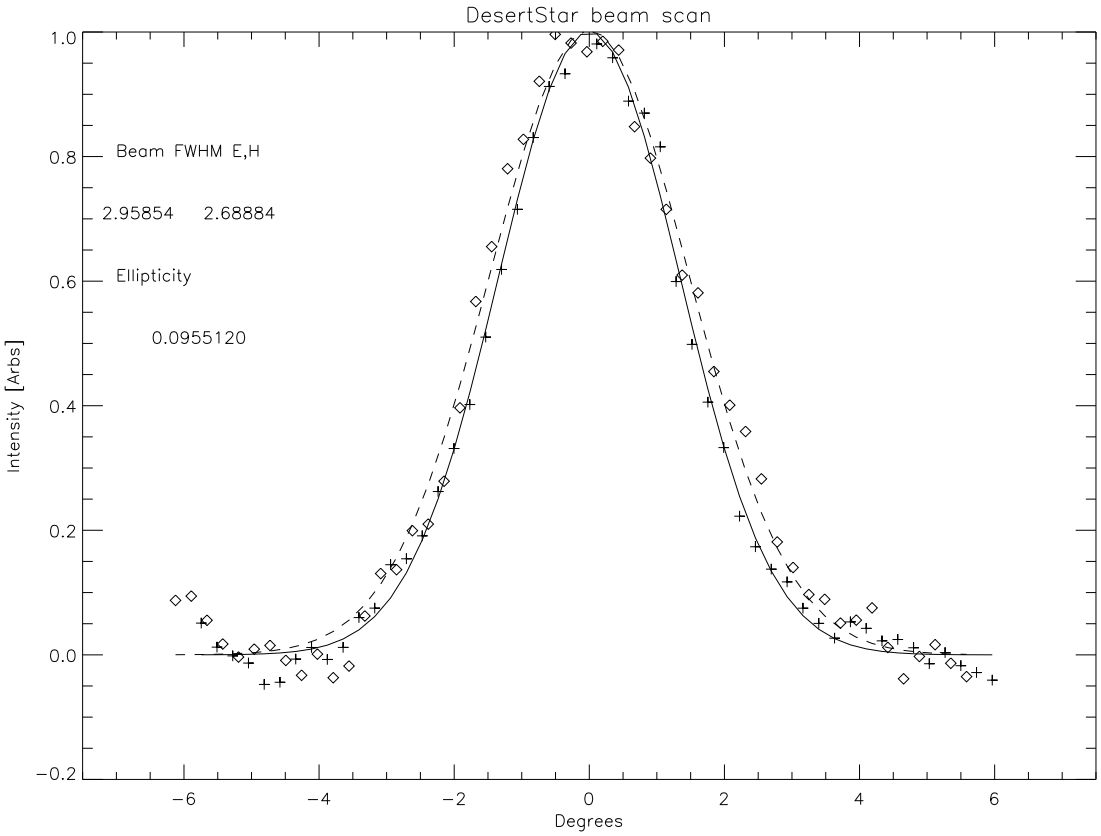

Figure 37: Measured E and H plane beam pattern cuts from the SORAL test range.

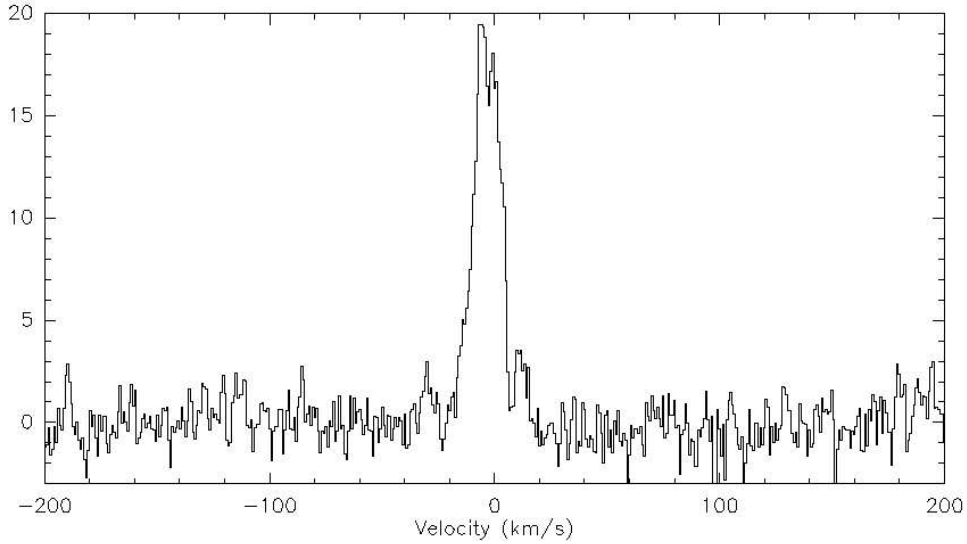

Figure 38: ^{12}CO (3-2) Spectrum of the star forming region DR21. This observation was made in position switched mode with an off position of 30’ in azimuth. A *linear* baseline has been fit and subtracted.

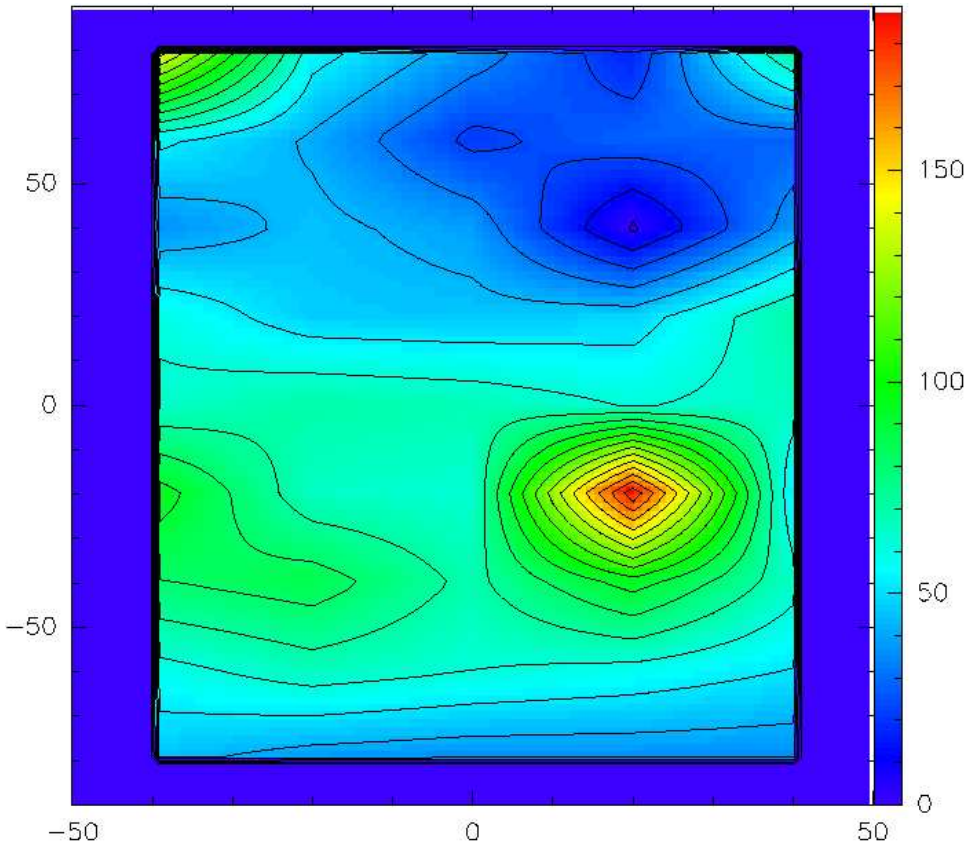

Figure 39: A ^{12}CO(3-2) integrated intensity map of the DR21 region. The problems with the mount have smeared out detail in the map, but no other instrument related artifacts are visible. The map was made with in position switching mode with τ~1.0 at the observing frequency of 345 GHz (LSB).

4. MILLIMETER AND SUBMILLIMETER SURVEY OF THE RCRA REGION

4.1 Introduction

R CrA is one of the most nearby active star forming regions, at 126pc (Maraco and Rydgren 1981). This close proximity allows for high spatial resolution observations, even with single dish millimeter wave and submillimeter wave telescopes. This cloud is home to many Herbig Ae/Be and T Tauri stars that have been studied extensively in the near infrared (Wilking et al. 1997). Recent observations in millimeter wave continuum (Henning et al 1994) and in molecular lines (Harju et al. 1993, Anderson et al. 1997, 1&2) have shown the existence of active, embedded star formation not directly associated with R CrA or any of the other pre-main sequence stars, but most likely associated with the class I source IRS7 (Taylor & Storey 1984).

R CrA was first studied in CO by Loren in 1979. His fairly low spatial resolution maps, 2.4', showed large amounts of CO peaking at the general location of R CrA, with high velocity wing emission throughout the map. The wing emission was later interpreted as a molecular outflow by Levreault (1988). His higher spectral and spatial resolution data revealed a large bipolar outflow with an extent of over 10'. Levreault also suggested that two outflows might be responsible for the morphology he observed, and that the embedded source IRS7 might be responsible for the outflow, not R CrA itself.

In 1985, Wilking et al. used the Kuiper Airborne Observatory to map R CrA in 100 μm and 50 μm continuum emission. The spatial resolution was not adequate to determine if R CrA or IRS7 was the driving source for the continuum and molecular line emission. Since these are both thought to be high mass sources that are not deeply embedded, there is a possibility the source is neither of these objects. At both 50 and 100 μm, the emission was found to be extended, with a flux density of 570 Jy/beam at 100 μm. These FIR continuum observations were supplemented by Henning et all. (1994) when they mapped the region using the 19 channel 1.3mm facility bolometer array at SEST. This 23" resolution map spatially resolved the region, and showed that the peak of the FIR emission is not associated with R CrA, but is much closer to the infrared source IRS7.

In 1993, Harju et al. performed a large area (40'x10') survey of the entire R CrA molecular cloud in $C^{18}O$. They estimated that the entire cloud complex contains more than 120 $M_{\odot}$ of molecular gas. The densest part of this core, centered around IRS7 and R CrA contains ~60 $M_{\odot}$ of molecular gas. Their kinematic analysis showed evidence for rotation around IRS7, and also clearly identified outflow lobes in the area. Follow-up work by Anderson et al. in 1997 (1997-1) concentrated on the outflow and rotational motions, and identified a large molecular disk around IRS7, which shows the kinematic signature of rotation. This work mapped the region around R CrA in multiple transitions of HCO^{+} to trace the dense gas. In this dense gas tracer, the outflow lobes have an extent of 4', but show no evidence for the multiple outflows suggested by Levreault. Unfortunately, con-

verting HCO^+ column densities to H_2 column densities is uncertain due to the widely varying abundance of HCO^+ throughout the Galaxy (Hogerheijde et al. 2002). HCO^+(3-2) was used to obtain high spatial resolution maps of the central 2'x2' region centered on R CrA with the intent of studying the possibility of a molecular disk. The data show an elongated structure, with three peaks to the northwest, southeast and south of IRS7. A slice in centroid velocity through IRS7 at a position angle of 135 degrees shows signs of rotation. Anderson et al. (1997-2) then followed up their previous wirk witih HCO+(4-3) mapping of the central 2'x2' around IRS7, providing improved spatial resolution and kinematic information. The integrated intensity map shows a structure elongated in the N-S direction, unresolved in the E-W direction, peaking on IRS7. The multi-lobed structure visible in HCO^+(3-2) is not present, which they explain as the effect of self-absorption on the line profiles. Velocity centroid maps show a strong velocity gradient near IRS7, and a slice orthogonal to the gradient at a position angle of about 135 degrees revealed the unmistakable fingerprint of rotational motion. They fit this rotation curve with a disk+central point source model and derived a central mass of 0.8 $M_\odot$. This result points towards the conclusion that IRS7 is a young, deeply embedded protostar of fairly low mass.

Our work is based on a data set consisting of ^{12}CO(1-0), ^{13}CO(1-0) and $C^{18}O$(1-0) mapping from the Kitt Peak 12m telescope, CO(4-3) and [CI] $^3P_1$ mapping from the 1.8m AST/RO telescope, both at moderate spatial resolution, supplemented by higher spatial resolution 870 μm continuum mapping, and $H^{12}CO^+$(4-3) and $H^{13}CO^+$(4-3) mapping

from the 10m Heinrich Hertz Telescope. These data trace the mass and kinematics of the molecular outflow over a 10'x10' region, and provide several methods of determining the mass and energetics of the outflow system, and the morphology, kinematics and mass associated with the molecular disk structure. Combined with the work by previous authors, we are closing in on building a coherent and consistent picture of the protostars in the R CrA molecular core.

4.2 Observations

Observations for this study were performed with a variety of mm-wave and submm-wave telescopes between April 2001, and April 2003. We have combined 100 square areminute maps of 0.04-0.06 pc spatial resolution and sub-km/s velocity resolution in various transitions and isotopes of CO and atomic carbon, with higher resolution mapping of the central region around IRS7 in CO(3-2) and the high density molecular tracer HCO^+(4-3) and its isotopic form $H^{13}CO^+$(4-3). Using the queue priority observing mode at the HHT, we have also obtained a fully sampled 10'x10', 870 μm continuum map of the region at 23" resolution. These multi-frequency, multi-transition data give a more complete picture of the active, young and heavily embedded star formation in the R CrA region than have been available before. A summary of the observations is given in Table 4. Figure 40 shows spectra in all our transitions at the position of IRS7. The spectra were generated by interpolating all the data cubes to the same number of spatial pixels (25x25) then convolving them to match the 95" beamsize of AST/RO at 460 GHz.

4.2.1 HCO^+(4-3) and CO(3-2) Mapping

In April, 2001 we made fully sampled 120”x80” maps centered on the embedded infrared source IRS7 in ^{12}CO(3-2), $H^{12}CO^+$(4-3) and $H^{13}CO^+$(4-3), at the HHT. Data were taken in the On-The-Fly mode with the facility dual polarization 345 GHz receiver built by the Max-Plank-Institut fur Radioastronomie in Bonn, Germany. Typical system temperatures at 15 degrees elevation were T_{sys}~2500K. The beamsize was 23”, and the telescope efficiency was η_{tel}~0.7 (for extended sources). RMS noise for the completed maps was 0.18K, 0.14K and 0.14K respectively. Backends were 62.5 kHz, 250 kHz and 1 MHz resolution filterbank spectrometers. The 250 kHz data was used for this work. Calibration was done with an ambient temperature and liquid nitrogen load, using the Hot-Sky-Cold method. Baselines were subtracted using a linear fit, and data was gridded and convolved to a 23” beam using the GILDAS software package. Data cubes were then exported in the FITS format for further processing using the IDL data processing package.

4.2.2 CO(4-3) and [CI] $^3P_1$-$^3P_0$ Mapping

CO(4-3) and [CI] $^3P_1$-$^3P_0$ observations were performed at the 1.8m Antarctic Submillimeter Telescope and Remote Observatory (AST/RO) between November, 2001 and January, 2002 (Stark et al. 2001). For the remainder of this chapter we will omit the lower level of the atomic fine structure transition for brevity. Maps were 10’x10’ in size, fully

sampled and centered on IRS7. Data were taken with the facility 490/810 GHz receiver, WANDA, in the position switched mode. Normally, CO(7-6) and [CI] $^3P_2$ are simultaneously observed along with CO(4-3) or [CI] $^3P_1$, but these data were taken in the Austral summer. While weather conditions were adequate for 460 and 490 GHz observations, the atmospheric opacity was too high to effectively observe in the 850 GHz atmospheric window. System temperatures ranged between 1500K and 9000K with typical values of ~4000K. Facility AOS spectrometers with 1 GHz bandwidth and 1 MHz resolution were used. Calibration was done using the Sky-Cold 1-Cold 2 method using actively cooled cold loads at 15K and 60K. Efficiency was measured to be η_{tel}~0.81, with a beamsize of 95” (Stark et al. 2003). Data were exported with the facility COMB software tool to individual FITS spectra. These were then compiled into a single CLASS format data file. The data were then fit with linear baselines and baseline subtracted. Processed data cubes were then exported in FITS format for further processing with IDL. Typical RMS noise for the reduced data cubes is 0.19K and 0.20K for CO(4-3) and [CI] respectively. Note that isotopic observations of CO were not made. ^{13}CO(4-3), C^{18}O(4-3) and C^{17}O(4-3) all occur at frequencies that are not observable from the ground, as they are all obscured by pressure broadened atmospheric water lines.

4.2.3 ^{12}CO(1-0), ^{13}CO(1-0) and C^{18}O(1-0) Mapping

CO(1-0) observations were performed at the Kitt Peak 12m telescope in April, 2003. The fully sampled maps are 10’x10’, centered on IRS7. Data were taken with the facility

3mm-hi dual polarization, single-sideband receiver in On-The-Fly mode. The MACS hybrid digital autocorrelation spectrometer was used, with 600 MHz bandwidth and 300 kHz resolution. System temperatures varied between 250K and 1000K. Several OTF maps per transition were co-added to produce the final data cube. Raw data had linear baseline fits subtracted, and were gridded and convolved to a 60” beamsize using AIPS software with the standard OTF reduction tools included with the latest AIPS release. Baseline subtracted and gridded data cubes were then exported via the FITS format for further processing with IDL. Typical RMS noise levels are 0.08K, 0.01K and 0.03K for ^{12}CO, ^{13}CO and C^{18}O respectively.

4.2.4 870 μm Continuum Mapping

870 μm continuum observations were made at the 10m HHT in March, 2003. Maps were 10’x10’ centered on IRS7, and fully sampled. Mapping was done with the facility 19-channel ^{3}He bolometer array used in the On-The-Fly mode. Beamsize was 23”, with a typical efficiency of η_{tel}~0.70. This is the identical instrument used by Henning et al. for their 1300 μm map on SEST, with a different bandpass filter. Data consists of a single OTF map made in less than one hour. Weather was exceptional, with the zenith atmospheric opacity measured at 225GHz of less than 0.05. Opacity at the observation frequency and azimuth was determined via skydips. Fits to this data show opacity at 343 GHz to be 0.260. Absolute calibration was done using Mars, assuming a flux at 343 GHz of 741.8 Jy, determined with the GILDAS ASTRO task. Reductions were performed using the GIL-

DAS NIC package. Scans were despiked, gridded and restored using standard NIC tools. Reduced and calibrated maps were exported via the FITS format for further processing with IDL. RMS noise in the map is 0.3 Jy/beam, assuming the worst case noise at the edge of the map.

4.3 Analysis

4.3.1 Morphology

Our survey concentrates on the central 10x10 arcminutes centered around IRS7. This encompasses the peak of the sub-mm continuum emission near IRS7, and is a local maximum for the molecular gas emission. Since optical depth effects severely effect the morphology of the ^{12}CO measurements, we use our 870 μm continuum map, along with the optically thin tracers of ^{13}CO(1-0) and C^{18}O(1-0) to trace the dust and gas mass in the region. Both the gas and dust show the same qualitative morphology, peaking around IRS7, with extended emission towards the northwest. The continuum emission is very strongly peaked around IRS7, with extended emission at flux levels ~10 times lower than the peak. Emission in optically thin CO isotopes peaks at the same location, but is much more extended, with a second peak ~200” to the northwest. Emission above the 3σ detection limit extends throughout most of the mapped region, but is generally oriented from the SE to NW. Features in the CO emission do not tend to correlate with the positions of the brightest infrared point sources in the region. A map of the central 120”x80” in the

high density tracer HCO^+(4-3) at 23” spatial resolution reveal the “molecular disk” detected by Anderson et al. (1997-1). The high density gas traces a structure elongated in Dec relative to RA with an aspect ratio of about 3:1. The continuum data, with the same spatial resolution, also clearly shows this elongated structure in the central region of the map. A hint to the structure is also seen in the CO maps, but the larger 60” beamsize of these data mask the disk. Maps of these data are presented in Figure 41.

4.3.2 Far Infrared Spectral Energy Distribution

We have combined our measured flux for the peak of the 870 μm emission with 1.3mm data from Henning et al. (1994) and IRAS 100 μm, 60 μm, 25 μm and 12 μm fluxes from the IRAS point source catalog to produce a FIR Spectral Energy Distribution (SED) of the R CrA core. The 1.3 mm and 870 μm measurements were done via OTF mapping with virtually identical beam sizes. The IRAS beam is much larger (~100”), but given the mm and sub-mm emission is strongly peaked at the central position, we estimate only 10%-20% contamination results from the inclusion of extended emission in the larger IRAS beam. We consider only the 100 μm and 60 μm fluxes when fitting a single diluted blackbody to the SED, since the two shorter wavelength bands are likely to contain contamination from hot dust. The SED shape bears this out. Since we are only concerned with the cold dust associated with the mm and sub-mm line emission, we do not attempt to fit a second blackbody component. We fit the FIR spectral energy distribution with a function of the form:

$$F_\nu = \Omega_s B_\nu(T)(1 - e^{-\tau_\nu}).$$

where $B_\nu(T)$ is the Planck function, Ω_s is the source size, and τ_ν is the dust optical depth modeled as:

$$\tau_\nu = \left(\frac{\nu}{\nu_0}\right)^\beta$$

where β is the spectral index of the grain emissivity and ν_0 is the frequency at which the dust becomes optically thick. This is generally assumed correspond to the peak in the FIR spectrum (Walker et al. 1990). The fit is a non-linear least squares fit to the flux, varying the parameters of source size, temperature and spectral index. Figure 42 shows the SED with our fit to the four lowest frequency points. We determine the fit parameters to be Ω_s=3.05x10^{-9} Sr, T=36.4 K and β=1.66. Formal errors in the fit are insignificant compared to the uncertainties involved in the simple model for the SED and the later estimates of dust and gas masses. The temperature and spectral index are comparable to other dust cores (Walker et al. 1990) but the beam filling factor is rather large at 0.31. This is explained by the close proximity of R CrA, only 126 pc. We then measure the FIR luminosity by integrating under the fit:

$$L = 3.1 \times 10^{-10} D^2 \int F_\nu d\nu$$

where L is the luminosity in solar luminosities, D is the distance in pc (126 pc), F_ν is in Janskys and ν is in GHz. We determine the luminosity to be 21.1 $L_\odot$, typical for a low mass, young protostar.

We can also use these data to estimate the dust and gas mass in the core, if the dust is optically thin. We can estimate the optical dust using the following relation:

$$\tau_d = F_\nu[\Omega_s B_\nu(T)]^{-1}$$

The dust opacity at 870 μm is 0.016, allowing us to follow Hildebrand (1983) to estimate the dust mass:

$$M_d = \frac{F_\nu D^2}{Q_\nu B_\nu(T)} \frac{4a\rho}{3}$$

where

$$Q_\nu = 7.5 \times 10^{-4} \left(\frac{125\mu m}{\lambda} \right)^\beta$$

and a and ρ are the grain radius and density. We assume 0.1 μm for a and 3 g cm^{-2} for the grain density. Assuming a gas to dust ratio f of 100, we can estimate the molecular hydrogen mass and column density.

$$M_{H_2} = M_d f$$

$$N_{H_2} = \tau_\nu \left(\frac{4a\rho f}{3 m_{H2} Q_\nu} \right)$$

We calculate a H_2 mass of 0.6 $M_\odot$, and a H_2 column density of 7.3x10^{23} cm^{-2} for the central 23” region centered on the peak of the FIR emission. Using the dust opacities of Draine and Lee (1984) the results are lower by about 30%. Given the large uncertainty in the gas to dust ratio, and dust properties, these estimates are probably reliable within only

a factor of several, but give some clue as to the properties of the dust core, especially when combined with mass and column density measurements obtained through other methods.

4.3.3 Core Mass and Kinematics via HCO^+(4-3)

Using the higher spatial resolution (23") 120"x80" $H^{12}CO^+$(4-3) and $H^{13}CO^+$(4-3) maps of the IRS7 region, we have determined the central mass of the FIR emission peak through LTE estimates of the gas column density and through the kinematic signature of the rotation of the molecular disk. Anderson et al. (1997-2) determined the central mass using HCO^+(4-3) observations using the kinematic method. This gives four independent measures of the central mass of the dust core, giving us some confidence in determining the properties of the central source.

With both $H^{12}CO^+$ and $H^{13}CO^+$ measurements at the central position, we can estimate the column density of HCO^+, and then estimate a column density of H_2 assuming an abundance for HCO^+. While the abundance of HCO^+/H_2 can vary by factors of several, and the assumption of LTE may not be good, this estimate still gives some handle on the gas mass at the peak of the FIR emission. We will assume the gas is in local thermodynamic equilibrium, and follow Walker et al (1988). The line shape of $H^{12}CO^+$ clearly shows the effects of self-absorption, so the LTE formalism will overestimate optical depth and therefore overestimate the column density and mass. Effects of self absorption on the

optically thick line's integrated intensity is unlikely to be more than a factor of two, overestimating the mass by a factor of a few. More complicated microtubulent methods can be used to take the effects of self absorption into account, but many more assumptions are necessary. We calculate the optical depth from the ratio of the optically thick to optically thin species:

$$\frac{I_{thick}}{I_{thin}} = \frac{(1 - e^{-r_a \tau})}{(1 - e^{-\tau})}$$

where I_{thick} and I_{thin} are the integrated intensities of the optically thick and thin species, respectively, r_a is the abundance ratio of the optically thick to thin species, and τ is the optical depth of the optically thin species. We assume an abundance ratio of 60 for the abundance of $H^{12}CO^+$ to $H^{13}CO^+$ (Kulesa 2003). We solve this equation numerically using a graphical-method root finding algorithm. We then assume the excitation temperature is the peak $H^{12}CO^+$ line temperature divided by the telescope efficiency of 0.7. This underestimates the excitation temperature, which partially counters the effect of the overestimate in optical depth. It is possible to solve for the excitation temperature, but this method grossly underestimates the excitation temperature when self absorption is present. Given the optical depth and excitation temperature, we can then calculate the column density of the optically thin species $N_{\nu,thin}$:

$$N_{\nu,\,thin} = T_{ex}\tau\Delta\nu\frac{6k}{8\pi^3\nu\mu^2}\left(\frac{2l+1}{2u+1}\right)\left(\frac{e^{\left(\frac{l}{2}\frac{h\nu}{kT_{ex}}\right)}}{1 - e^{-\frac{h\nu}{kT_{ex}}}}\right)$$

where l is the lower rotational level, u is the upper rotational level, μ is the dipole moment of the molecule and Δν is the frequency region over which the integrated intensity is measured. At the peak of the map, we calculate an excitation temperature of 15K, an optical depth for $H^{13}CO^+$ of 0.04, and a column density of H_2 of $2.2x10^{23}$ cm^{-2}. This translates to a gas mass in the central beam of 0.5 $M_{\odot}$, assuming an abundance ratio of $H^{12}CO^+$ to H_2 of 10^{-9}.

We can also calculate the central mass using the motion of the gas by making a map of the centroid of the line velocity calculated over the line core. If bulk rotation is present, a slice through the source orthogonal to the velocity gradient will result in the kinematic signature of rotation (a rotation curve). We simply measure the amplitude of the positive and negative velocity peaks, and the projected distance between them assuming a distance to the source of 126 pc. We then calculate the central mass assuming circular motion around a point mass, and a massless disk. We also assume the disk is viewed edge-on. This provides a kinematic lower limit to the enclosed mass.

We calculate the velocity centroid of each map position following Adelson et al. (1982):

$$V_c = \frac{\sum_i (V_{Dopp})_i (T_A)_i}{\sum_i (T_A)_i}$$

where V_{Dopp} is the velocity offset from line center and T_A is the line brightness at the offset velocity, indexed by velocity channel i. The result is a map of line centroid velocity, where the line centroid is the velocity at which the integrated intensity redward and blueward of the centroid velocity is the same. This gives a measure of the kinematics of the object averaged over the line. We compute the centroid velocity over the range -3.0 to +2.5 km/s, which encompasses the entire line core at the central position, and averages over self-absorption effects.The resulting map is shown in Figure 43. We take a slice at a position angle of 120 degrees, orthogonal to the velocity gradient. The map has been interpolated by a factor of 3 in both dimensions. A slice centered on IRS7 was averaged over three columns to produce the rotation curve. We then assume circular motion around a point mass to determine an upper limit for the central mass:

$$M_c = \frac{v^2 r}{G}$$

where we define v as the half-amplitude of the rotation curve, and r as half the distance between peaks in the curve. We determine a rotational velocity of 0.47 +/- 0.04 km/s, a radius of 0.015 +/- 0.001 pc and a derived mass of 0.75 +/- 0.15 $M_\odot$, assuming a 3” pointing error, and errors in the velocity centroid according to Narayanan et al. 2000. This is consistent with the result of Anderson et al. of 0.8 $M_\odot$.

4.3.4 Outflow

In the convolved spectra of Figure 40, it is clear that the optically thick species show extended wing emission at high velocities. We made outflow maps by calculating the integrated intensity in the line wings for ^{12}CO(1-0), ^{13}CO(1-0), ^{12}CO(4-3) and [CI] $^3P_1$. We use the convolved spectra to determine the velocity range of the wing material. We use the maximum observed redshifted and blueshifted emission in all cases to determine the outer velocity boundaries, and use the maximum and minimum velocity of C^{18}O(1-0) as the inner boundary. Figure 44 shows the resulting outflow maps, and the location of known infrared sources in the area. Optical depth effects alter the morphology of the ^{12}CO maps as compared to the ^{13}CO map. In [CI], only the red outflow lobe is clearly visible.

Over the velocity range -4 to 3 km/s and 8 to 15 km/s, we can use both the ^{12}CO(1-0) and ^{13}CO(1-0) outflow data to compute the column density of CO as in section 4.3.3. We can see from Figure 40 that the peak antenna temperature for CO(1-0), CO(3-2) and CO(4-3) are all similar. This points to a reasonably thermalized population, so the assumption of LTE is probably valid. In this analysis, we assume the peak line temperature, corrected for efficiency, is the excitation temperature in the outflow. In addition, the abundance of CO/H_2, while certainly not exactly known, varies less across the galaxy than the HCO^+/H_2 abundance ratio (Hogerheijde 2002). As is clear from the ^{12}CO(1-0) spectrum at the center position, the optical depth to the blue wing is much higher than the red,

either through foreground obscuration or self-absorption. We find blue wing and red wing masses of 0.36 $M_\odot$ and 0.29 $M_\odot$, respectively, assuming an abundance ratio of ^{12}CO to ^{13}CO of 60 and a $^{13}CO/H_2$ abundance ratio of $2.5x10^{-6}$. We can also calculate a characteristic age by dividing the extent of the outflow by the maximum observed velocity from line center, v_c. We take 300" as the outflow extent, and 17 km/s as the maximum velocity, which gives a characteristic age of 10^4 years. We can also calculate the characteristic values for the momentum, Mv_c, the kinetic energy, $0.5Mv_c^2$, the outflow mechanical luminosity, KE/Age, and the mass outflow rate, M/Age. Outflow mass and energetics are summarized in Table 5.

For the ^{12}CO(4-3) map, it is impossible to use isotopic data and the assumptions of section 4.3.3 to determine the CO column density and therefore the outflow mass. All the isotopic forms of CO(4-3) are not observable from the ground because of atmospheric absorption due to water and molecular oxygen. For this transition, we must assume the line wings are optically thin to determine outflow mass and energetics. Making this assumption will underestimate (possibly severely) the mass in the outflow. We again assume the excitation temperature is the peak CO line temperature divided by the telescope efficiency, 0.81 for AST/RO at 460 GHz (Stark et al. 2001). We follow Snell et al. (1984) to determine the column density of ^{12}CO assuming the emission is optically thin:

$$N_{CO} = \frac{4.2 \times 10^{13} T_{ex} \int T_R(CO) dV}{\exp\left(-\frac{h\nu}{E}\right)} cm^{-2}$$

We can then translate this to H_2 column density assuming an abundance ratio of 10^{-4}. This gives a lower limit to the column density and mass of the outflow. This approach results in masses of about half that as determined by the optically thick estimates for the CO(1-0) data. This is not surprising, since the ^{13}CO optical depth was calculated to be ~0.6, which translates to a ^{12}CO(1-0) optical depth in excess of 30. We can also apply the same approach to the ^{12}CO(1-0) data to see the effects of taking optical depth into account. Masses are calculated to be 0.21 $M_\odot$ and 0.06 $M_\odot$ for the red and blue wings respectively, assuming a $^{12}CO/H_2$ abundance ratio of 10^{-4}. The value for the red wing is within 30% of the value obtained by the LTE analysis, but the blue wing mass is 6 times lower. This is due to the self absorption effects on the blue wing of the ^{12}CO(1-0) lines. Given the effects of the LTE analysis, which overestimates optical depth in the case of self-absorption, and the optically thin assumption which underestimates the optical depth, the two methods most likely bracket the possible mass and energetics of the outflow system, if the assumption that the rotational level populations are in LTE is adequate.

4.4 Discussion

4.4.1 A Possible Class 0 Source Driving the FIR Emission

While our data is consistent with previous work, the sum of the data points toward a somewhat different conclusion than previous work. Initially, most research assumed the molecular line and FIR emission in the region was directly associated with R CrA. Work by Harju et al. and Anderson et al. suggested the embedded class I source IRS7 as the most likely driving source for this emission. We believe that the source of the molecular line and cold dust emission is a deeply embedded class 0 source about 10” south of IRS7, with a mass of about 0.5 $M_{\odot}$.

One interesting feature of all the data is that the peak of the emission is south of the location of IRS7 by ~10” in all cases (Figure 41). While this is less than a single beam in offset, the fact that it exists in all the maps, taken at two different telescopes over the course of two years suggests that it is significant. Kinematic evidence also points to a source farther south. The center of the velocity gradient in the area of IRS7 is south of the infrared source by approximately 10”, as shown in Figure 43. Previous attempts at FIR continuum mapping (Wilking et al. 1985) and spectral line measurements (Levreault 1988, Loren 1979) did not have adequate spatial resolution to address this question short of suggesting that R CrA itself was not the source of the FIR continuum or line emission. Harju et al. (1994) also find that the optically thin CO emission is not exactly centered on

IRS7, but Anderson et al. (1997 1 and 2) find no offset between IRS7 and the HCO^+(3-2) and (4-3) emission. Henning et al. (1994) mapped the IRS7 region at 22” spatial resolution in 1.3mm continuum emission, and found the peak of the mm-wave continuum to also be ~10” south of the position of IRS7. The possibility exists that the peak of the mm-wave and sub-mm wave emission, and the driving source for the molecular outflow(s) in the region might not be IRS7, but a more deeply embedded source not detected in infrared surveys as a point source.

Other evidence exists, independent from the astrometric evidence, that points to the conclusion that driving source of this emission is not a class I source, but a class 0 source. Our mass estimates for the core come from both a kinematic measure (Figure 43) of the total mass of the protostar and surrounding gas, and the measure of the mass of the gas alone via measurement of the FIR continuum flux and measurement of the column density of HCO^+. All three of these measurements have considerable uncertainty, but taken together point towards a deeply embedded source of about 0.5 $M_\odot$ with a gaseous envelope of similar mass. The kinematic measurement from the centroid velocity of HCO^+(4-3) shows a velocity gradient strongly suggestive of rotation. If we interpret this as rotation, we measure a lower limit of the enclosed mass in the 0.015 pc radius volume about the center of the motion as 0.75 $M_\odot$. This assumes all the mass is concentrated at the center. We also estimated the gas mass in the central 22” (about half the distance between velocity peaks in the velocity gradient) via continuum observations in section 4.3.2. We used the

continuum flux to compute the expected gas mass, assuming silicate dust in 0.1 μm grains, and a Hildebrand (1983) dust emissivity that varies like λ^{-2}. We then assumed a gas to dust ratio of 100 to compute a total gas mass of 0.6 $M_{\odot}$. While this method makes many simple assumptions, it is probably correct to within a factor of a few.

The measurement of the H_2 mass via HCO^+ also gives a similar answer. We used $H^{12}CO^+$ and $H^{13}CO^+$ measurements with a 22" beamsize to estimate the column density of H_2 (Section 4.3.3). Both the varying abundance of HCO^+ to H_2 and the effects of self absorption are uncertain. Self-absorption will cause us to overestimate the amount of HCO^+ present. In addition, we assumed an abundance ratio of HCO^+/H_2 of 10^{-9}. This ratio has been shown to be as high as 10^{-8} in some regions (Hogerheijde et al. 2002). Keeping our nominal assumptions, and neglecting the effects of self absorption, we estimate a gas mass of 0.5 $M_{\odot}$. While uncertain, both these measures point to a total envelope mass that is on the order of the mass of the central source, given the kinematic estimate of the total mass of source+envelope. In addition, the somewhat small FIR luminosity of 21 $L_{\odot}$ similar to other low mass protostars of about 0.5 $M_{\odot}$ (Walker et al. 1990).

4.4.2 Infall

Class 0 protostellar objects usually show the enhanced blue peak signature of infall motion. As seen in Figure 46, spectra near the center position of the map show this

enhanced blue peak. In addition, the centroid velocity map in Figure 43 shows the “Blue Bulge” signature of infall motion developed by Narayanan et al. (1998). This is expected from the spectra themselves, since at the central position, the blue peaked infall line shape dominates over the effects of rotation, causing a “Blue Bulge” in the centroid velocity plot at the position of the source. North and south of the central position, rotation begins to dominate the kinematics. At about 30” east and west of the source at the edges of the HCO^+ map, the outflow dominates. In our CO maps, and in the CO maps of others, the outflow completely masks all signs of rotation and infall. Only in dense gas tracers do all the intertwined motions reveal themselves near the source. Convolving spectra to larger beamsizes, we continue to see a line shape suggestive of infall. In Figure 47, the HCO^+ spectrum has been convolved in half beam increments from 22” to 77”, which is essentially the entire HCO^+ map. The infall lineshape is still clearly visible in all the spectra, suggesting that infall is occurring over the entire central region around the protostellar source. This points toward an infall region of at least 6000 AU in radius. Using our measurements of FIR luminosity and temperature, we can estimate the mass infall rate for this object. If all the FIR luminosity is generated through accretion, then

$$L_{FIR} = \frac{GM\dot{M}}{r}$$

where r is the radius of the protostar and M is the mass of the protostar. We assume $2x10^{11}$ cm for the radius, about 3 $R_\odot$ (Stahler, Shu & Taam 1980), and 0.5 $M_\odot$ for the mass of the central object, given our mass estimates of the source+envelope and envelope masses.

This gives a mass accretion rate of 4×10^{-6} $M_{\odot}$/yr, uncertain to within a factor of a few. We can also assume a uniform sphere of gas undergoing free, gravitational collapse. We assume a soundspeed due to only thermal pressure, and ignore magnetic and turbulent support (Shu 1977).

$$a = \sqrt{\frac{kT}{m_{H_2}}}$$

Then the mass accretion rate is estimated by:

$$\dot{M} = \frac{0.975 a^3}{G}$$

Here, we estimate a mass accretion rate of 1×10^{-5} $M_{\odot}$/yr. Both these estimates are consistent with a low mass, class 0 source.

4.4.3 Atomic Carbon Distribution

In the canonical picture of carbon in a molecular cloud, an “onion-skin” model is used whereby the carbon is ionized in the outer layer of the cloud as [CII]. Further in the cloud where the carbon is more shielded, it is in atomic form as [CI]. Deeper in the cloud, the carbon forms CO. In some cases, where the cloud material is very clumpy, this same picture holds, but now each clump acts as a small cloud, causing [CII] and [CI] to appear well mixed throughout the cloud. We see evidence for both these effects in our carbon observations. To reveal enhancement of [CI] relative to $C^{18}O$, we calculated the column

density of both species, assuming they are both optically thin. CO was treated as in section 4.3.4 for CO(4-3). We estimated the column density of the atomic carbon following Walker et al. (1993-2):

$$N_C = \frac{N_1}{3}\left(e^{\frac{23,6}{T_{ex}}} + 3 + 5e^{\frac{-38.8}{T_{ex}}} \right)$$

where

$$N_1 = 5.94 \times 10^{15} \int T_{mb} dV (cm^{-2})$$

We then plotted the ratio of [CI]/C^{18} O column density normalized to the average over the map to look for enhancement/depletion of atomic carbon relative to CO, considering only locations were both the [CI] and CO integrated intensities were larger than the 2σ noise level. The results are shown in Figure 48. As expected from the canonical picture, [CI] is enhanced at the edges of the cloud, and depleted towards the center. We have plotted the contours over an optical image of the region from the Palomar Sky Survey. The regions of low relative [CI] abundance correlate with the regions of high optical extinction, and the region with strong FIR continuum emission.

In the outflow map of Figure 44, we see that carbon is observed throughout the red wing of the outflow. Only a small amount of carbon is visible in the blue wing, possibly due to foreground absorption. While the [CI] is not as ubiquitous as ^{13}CO in the outflow, it is still visible, and does not appear to be in a shell configuration. This leads us to believe that while atomic carbon is enhanced at the edge of the cloud, some atomic carbon is still

mixed throughout the cloud, pointing to clumpy structure even in the outflow. This is the same conclusion as Walker et al. 1993 in their pioneering work on atomic carbon in outflows, and shows that someultraviolet photons can make their way to the heart of molecular clouds, even with very high visual extinctions.

4.4.4 System Configuration

The kinematic signs of rotation, infall and outflow, combined with the distribution of CO, HCO^+ and submillimeter continuum emission all combine to produce a picture of star formation in the R CrA molecular core. Due to the proximity of R CrA, and the high physical spatial resolution we have, the kinematic signatures of infall, rotation and outflow are all well defined and relatively easy to separate. We propose the configuration shown in the cartoon representation of Figure 49, overlaid on the centroid velocity plot of HCO^+. We believe a highly embedded class 0 protostellar source (Section 4.4.1) is the driver for the FIR emission in the area. Kinematic and morphological evidence point to a location about 10” south of the class I source IRS7. This source is surrounded by a rotating molecular disk, first discovered by Anderson et al. (1997 1&2). Our HCO^+(4-3) measurements point to a similar conclusion, with an enclosed mass of 0.75 $M_\odot$ +/- 0.15 $M_\odot$, but we believe the source at the center of this molecular disk is not IRS7. Other mass estimates of the molecular gas envelope through 870 μm continuum measurements, and HCO^+ measurements suggest a central protostar of less than 0.5 $M_\odot$, with an envelope of similar mass. We postulate the disk major axis is at a position angle of about 120 degrees. This position

angle gives the cleanest rotational signature in the velocity gradient, and the morphology of the HCO^+(4-3) integrated intensity seems to agree. The axis of the molecular outflow is consistent with a position angle orthogonal to this, at about 30 degrees. This molecular disk has a major axis of about 2500 AU, from our kinematic estimate, and is unresolved in the orthogonal direction in all our observations. In the central 20”-30” of the HCO+ map, the line profiles show a strong infall line shape. This shape persists when the spectra are convolved to beamsizes as large as the entire HCO+ map. In addition, the central region of the centroid velocity plot shows the “Blue Bulge” signature of infall motion. This infall region is at least 6000 AU in radius, surrounding the molecular disk. At distances larger that 6000 AU, the kinematics of the molecular outflow begin to dominate the line profiles. At lower spatial resolution, and with more sensitivity to the lower density gas, CO maps are virtually all dominated by outflow kinematics in the optically thick case, and by the material at the systemic velocity of the cloud in the optically thin case.

4.5 Summary

We have observed the molecular core near R CrA in ^{12}CO(1-0), ^{13}CO(1-0), $C^{18}O$(1-0), ^{12}CO(3-2), ^{12}CO(4-3), [CI] $^3P_1$, $H^{12}CO^+$(4-3), $H^{13}CO^+$(4-3) and 870 μm continuum. This varied data set points toward the conclusion that the source for the FIR line and continuum emission, and the driving source for the molecular outflow might be a yet unidentified class 0 source deeply embedded in the cloud, not the class I source IRS7 as previously thought. We use the HCO^+ measurements and the continuum measurements to estimate

the envelope mass at the peak of the FIR emission, and find a gas mass of about 0.5 $M_{\odot}$. We also use the centroid velocity of HCO^{+} to estimate the enclosed mass inside the rotating molecular disk to be ~0.75 $M_{\odot}$. Both these measurements suggest a low mass (0.5 $M_{\odot}$) protostar surrounded by an envelope of similar mass. In addition, the FIR SED yields a luminosity of 21 $L_{\odot}$ from cold dust, which is also consistent with a low mass protostar. These estimates are consistent with a class 0 source. In addition, the peak of the FIR line and continuum emission is not centered on IRS7, but is offset ~10” to the south, as is the center of rotation derived from the HCO^{+} velocity gradient.

The interaction of rotation, infall and outflow are all visible in the high spatial resolution HCO+ map of the central region of the cloud. Lineshapes show evidence for all three motions in the central 60”x60” of the map. A slice through the centroid velocity plot along the major axis of the molecular disk reveals a clean signature of rotation.The HCO^{+} lineshapes and centroid velocity plots also show evidence for infall motions, with blue peaked line profiles at the center of the map, even when convolved to large beamsizes. In addition the centroid velocity plot shows the “Blue Bulge” signature of infall. We calculate a mass infall rate of ~10^{-5} $M_{\odot}$/yr. The molecular outflow is detected in CO(1-0), CO(4-3), HCO^{+}(4-3) and [CI] $^{3}P_{1}$. We trace the outflow to the edge of our 10’x10’ mapped region. In the small 120”x80” HCO^{+} map, we only see signs of outflow at the east and west edges of the map, since infall and rotation kinematics dominate in the central region. We have estimated the outflow mass and energetics using both CO(1-0) and CO(4-

3). These estimates bracket the likely values for these parameters in the outflow system. The outflow mass is ~0.7 $M_{\odot}$, similar to the mass of the protostar we believe is driving the outflow. The energetics are typical for a molecular outflow around a young, low mass protostar, with a mechanical luminosity much less than the FIR luminosity.

The result is a picture that supports the “standard” model for low mass star formation. We believe continued study of this system is important due to the high spatial resolution available. The system shows all the kinematic signatures of a class 0 system, and high spatial resolution allows us to disentangle all the effects normally blurred together in more distant sources. Follow-up with mm-wave interferometers in both continuum and high density molecular tracers could reveal the class 0 source, if present, and allow detailed study of the infall and rotational motions of the molecular disk. Physical resolutions of better than 200 AU are easily obtainable. Observing the R CrA region with interferometers in the northern hemisphere will be difficult, but the test of theories of low mass star formation such observations would provide makes the effort worthwhile.

Line	Map Size	Beam Size	Spectral Resolution	RMS Noise	Telescope
^{12}CO(1-0)	600”x600” 0.4x0.4 pc	60” 0.04 pc	300 kHz 0.8 km/s	0.08 K	KP12m
^{13}CO(1-0)	600”x600” 0.4x0.4 pc	60” 0.04 pc	300 kHz 0.8 km/s	0.01 K	KP12m
C^{18}O(1-0)	600”x600” 0.4x0.4 pc	60” 0.04 pc	300 kHz 0.8 km/s	0.03 K	KP12m
^{12}CO(3-2)	120”x80” 0.4x0.4 pc	23” 0.01pc	250 kHz 0.2 km/s	0.18 K	HHT
^{12}CO(4-3)	600”x600” 0.4x0.4 pc	95” 0.06 pc	1 MHz 0.7 km/s	0.19 K	AST/RO
[CI] $^3P_1$	600”x600” 0.4x0.4 pc	95” 0.06 pc	1 MHz 0.6 km/s	0.20 K	AST/RO
HCO$^+$(4-3)	120”x80” 0.07x0.05 pc	23” 0.01 pc	250 kHz 0.2 km/s	0.14 K	HHT
H^{13}CO$^+$(4-3)	120”x80” 0.07x0.05 pc	23” 0.01 pc	250 kHz 0.2 km/s	0.14 K	HHT
870 μm Continuum	600”x600” 0.4x0.4 pc	23” 0.01 pc	$\lambda/\delta\lambda$=10	0.3 Jy/beam	HHT

Table 4: Summary of Observations

Line Wing	**Mass**	**Momentum**	**Kinetic Energy**	**Mechanical Luminosity**	**Mass Outflow Rate**
	$M_\odot$	**g cm/s**	**ergs**	**$L_\odot$**	**$M_\odot$/yr**
CO(1-0) LTE red	0.29	$1.0x10^{39}$	$8.5x10^{44}$	0.34	$2.8x10^{-5}$
CO(1-0) LTE blue	0.36	$1.2x10^{39}$	$1.0x10^{45}$	0.41	$3.4x10^{-5}$
^{12}CO(1-0) Optically thin red	0.21	$7.2x10^{38}$	$6.1x10^{44}$	0.25	$2.0x10^{-5}$
^{12}CO(1-0) Optically thin blue	0.06	$2.2x10^{38}$	$1.9x10^{44}$	0.07	$6.0x10^{-6}$
^{12}CO(4-3) Optically thin red	0.16	$5.5x10^{38}$	$4.7x10^{44}$	0.19	$1.5x10^{-5}$
^{12}CO(4-3) Optically thin blue	0.13	$4.5x10^{38}$	$3.8x10^{44}$	0.15	$1.3x10^{-5}$

Table 5: R CrA Outflow Energetics

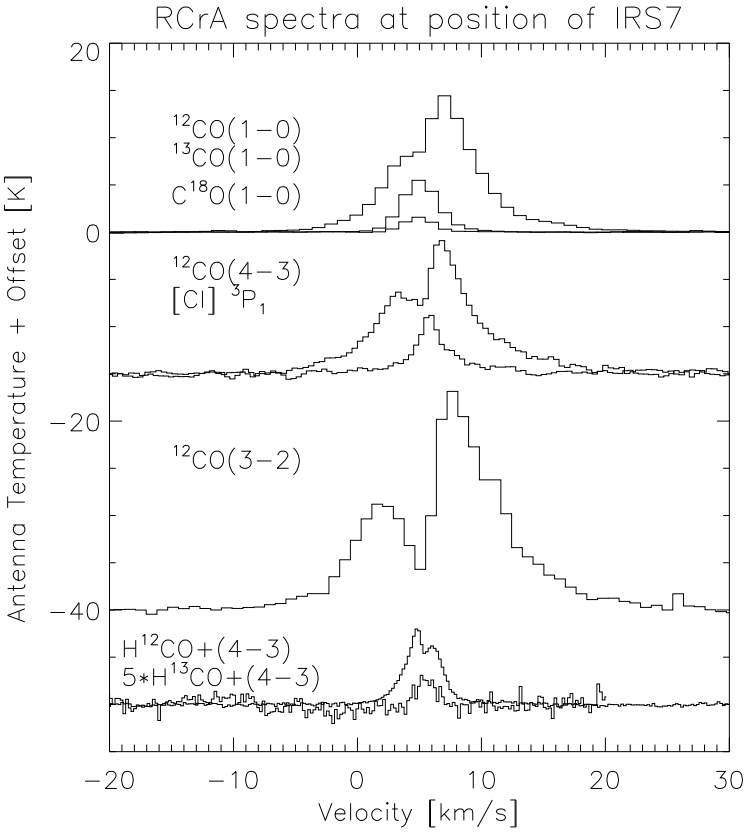

Figure 40: Spectra centered on IRS7 from all our data sources.
Spectra were generated by re-gridding all the maps to the same number of pixels, then by convolving the maps to match the largest beamsize, 95". Optically thick CO transitions are clearly dominated by outflow kinematics, and are subject to significant self-absorption.

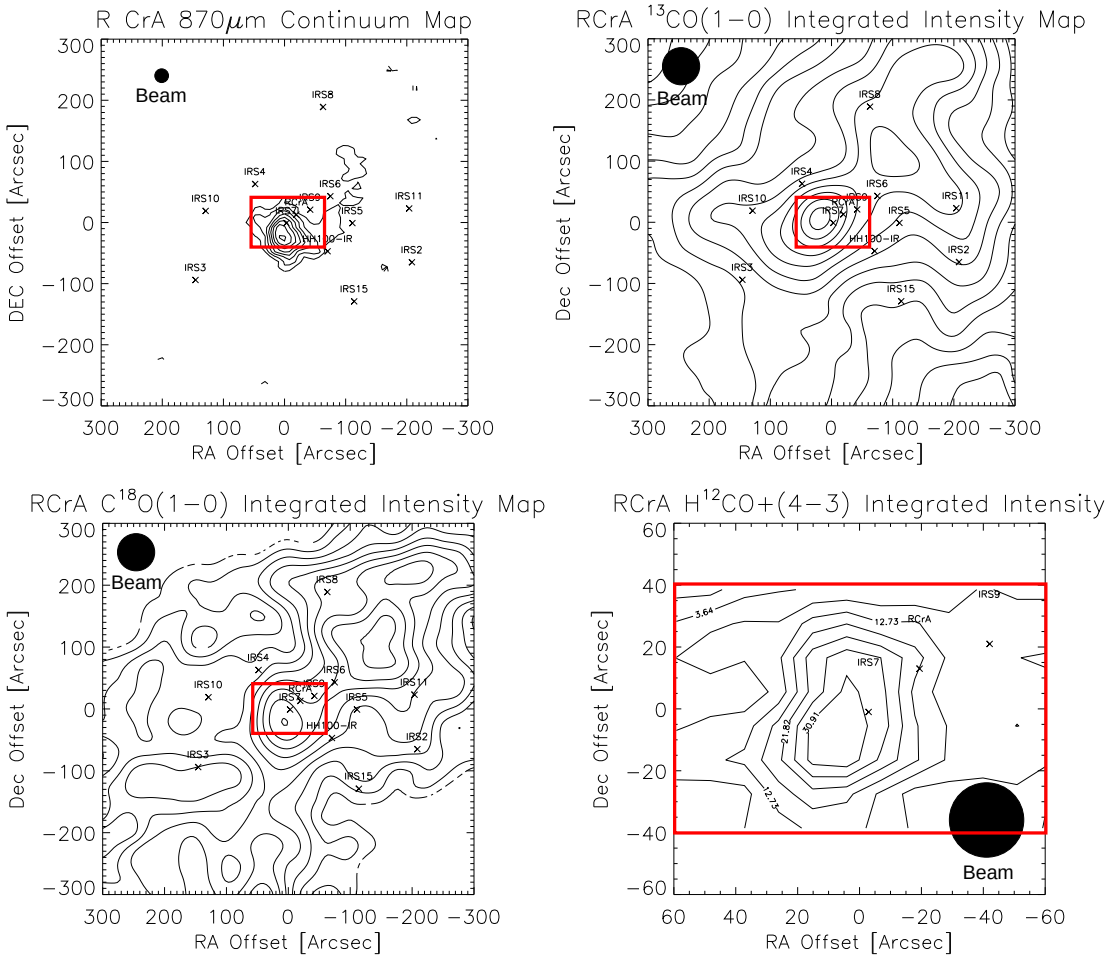

Figure 41: Molecular integrated intensity and continuum maps of R CrA.
10'x10' maps in 870 μm continuum emission, ^{13}CO integrated intensity, C^{18}O integrated intensity, and a 80"x120" map in HCO^{+}(4-3) integrated intensity.Minimum contours are at the 2σ level, with 2σ contour spacing. Beamsizes are specified in each map. The continuum emission from cold dust is well traced by the optically thin CO emission. The HCO^{+} inset shows the "molecular disk" structure reported by Anderson et al. 1997, elongated along the N-S axis.

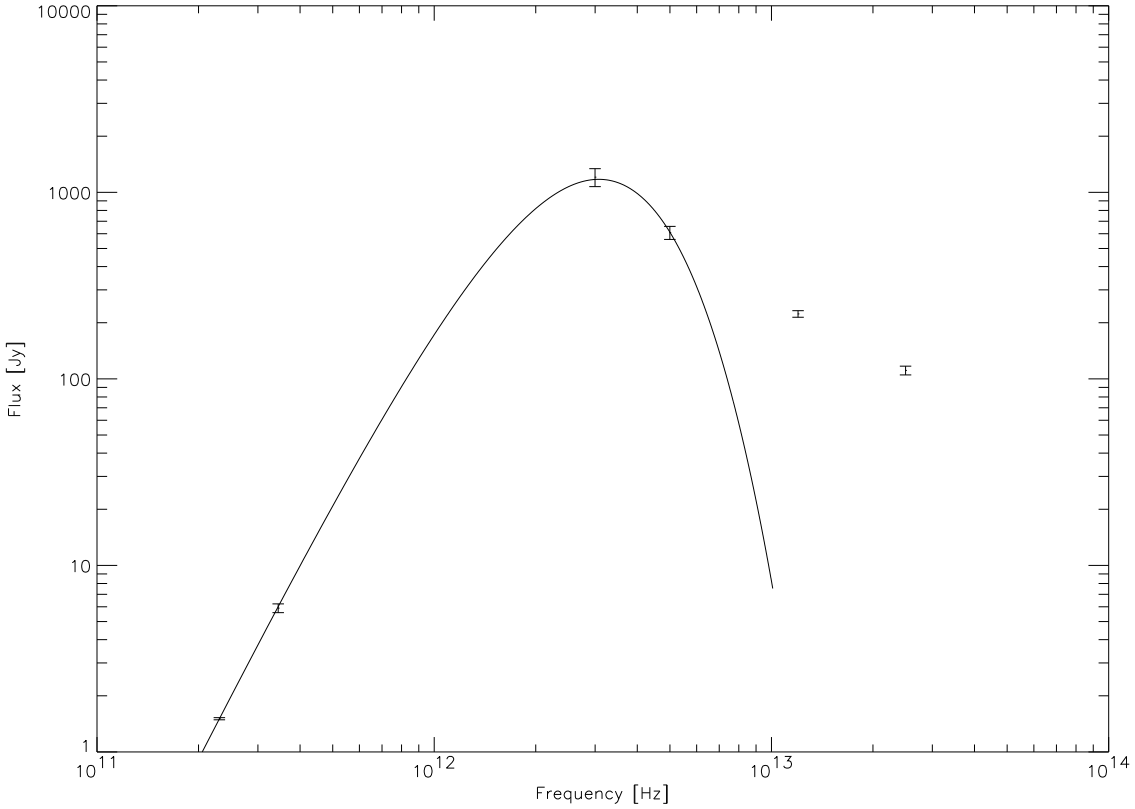

Figure 42: The FIR SED of the R CrA region centered on IRS7.
The 870 μm point is from this work. The 1300 μm point is from Henning et al. 1994, data taken with the 19 channel facility bolometer array at SEST. The FIR data are IRAS measurements of R CrA. Since the IRAS beam is ~100”, some contamination from the surrounding material off the dust emission peaks is present. We fit only the 100 μm and 60 μm points to exclude contamination by hot dust. Error bars are +/- 1σ.

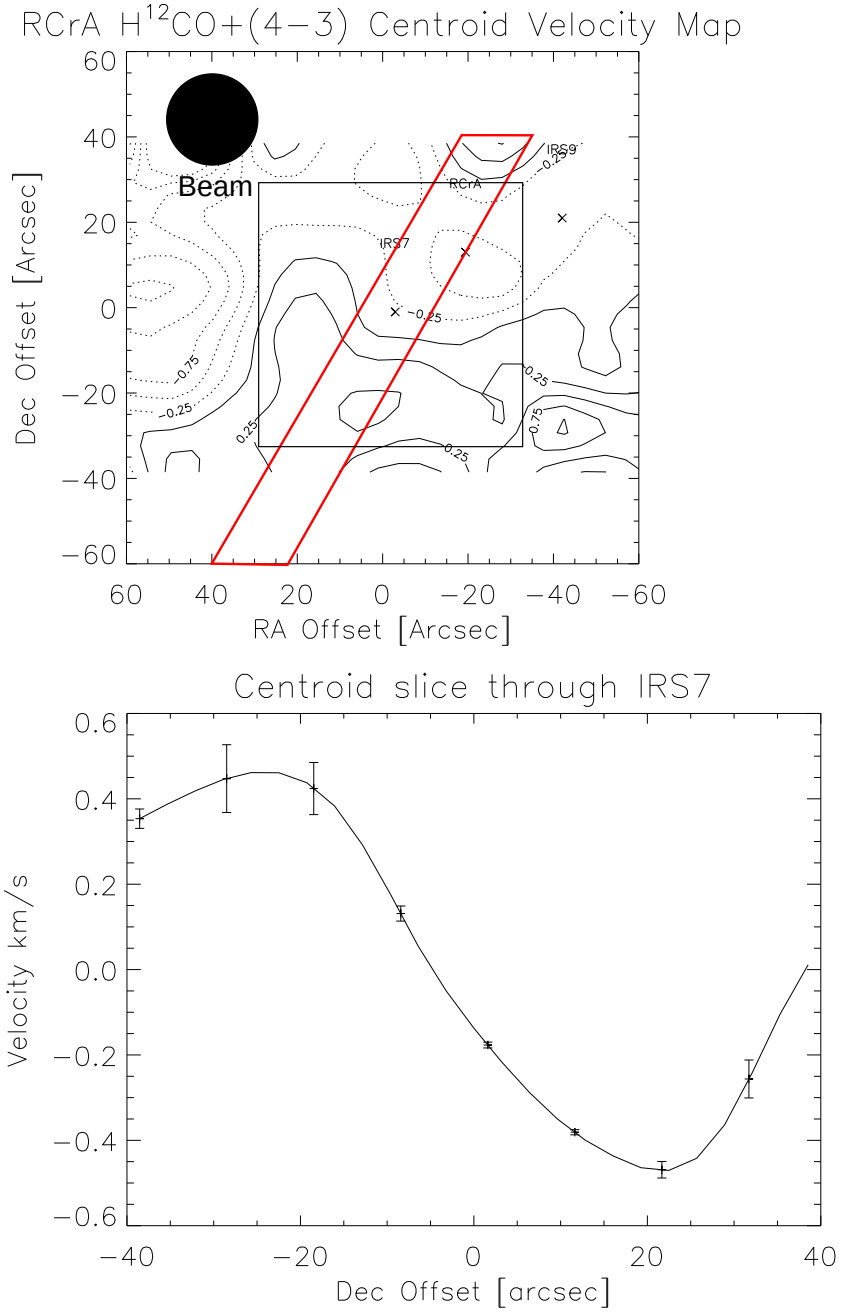

Figure 43: HCO^+(4-3) centroid velocity plot.
Contours are 0.125 km/s, with dotted contours denoting negative velocity. Below is a slice denoted by the box showing the signature of rotation. The centroid velocity plot also shows the “Blue Bulge,” a sign of infall motions.

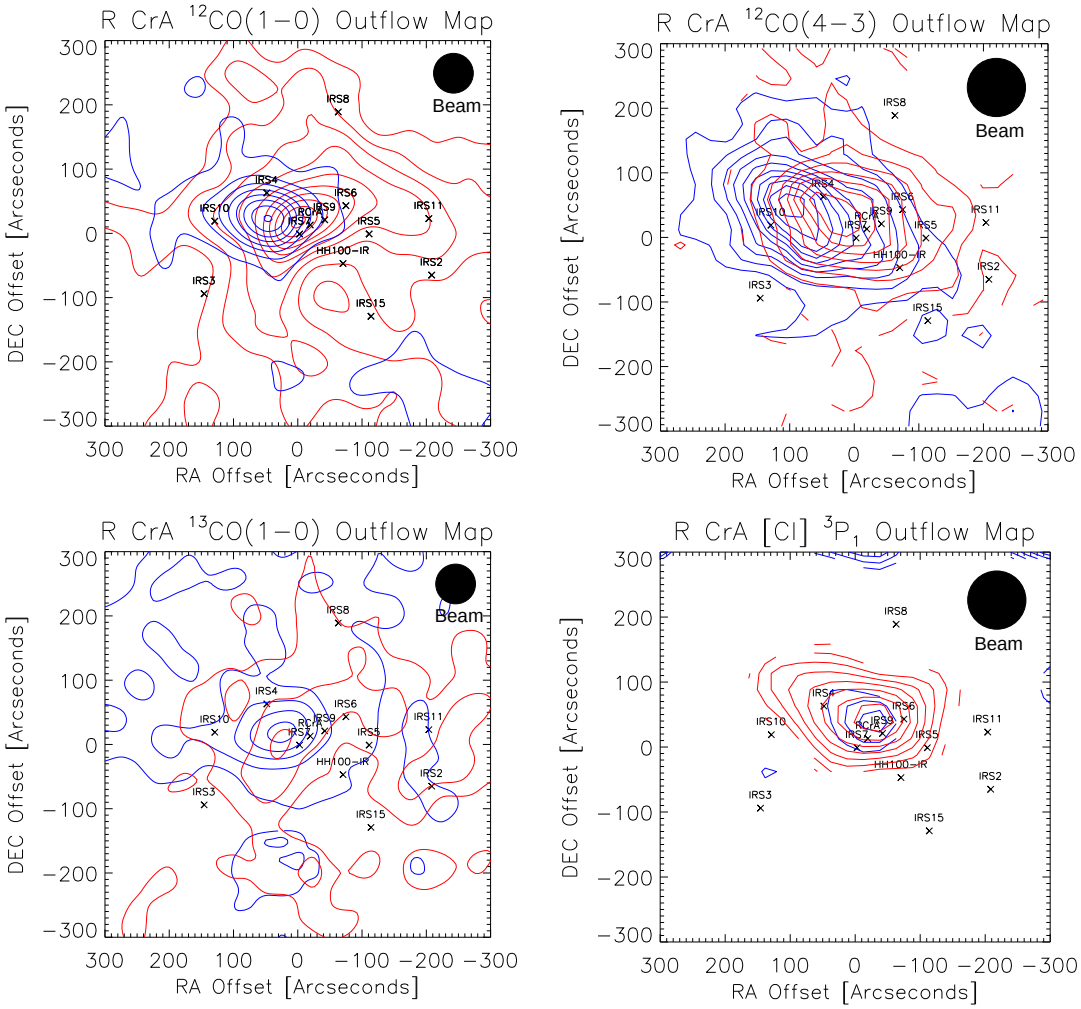

Figure 44: Outflow maps of R CrA..
Panels are ^{12}CO(1-0), ^{12}CO(4-3), ^{13}CO(1-0) and [CI] $^{3}P_{1}$. Minimum contours are 2σ, with 2σ contour spacing. The ^{12}CO(1-0) and ^{12}CO(4-3) blue wing velocity interval is -10 to 3 km/s, while the red interval is 8 to 22 km/s. The ^{13}CO(1-0) and [CI] blue wing interval is -4 to 3 km/s, while the red wing interval is 8 to 15 km/s.

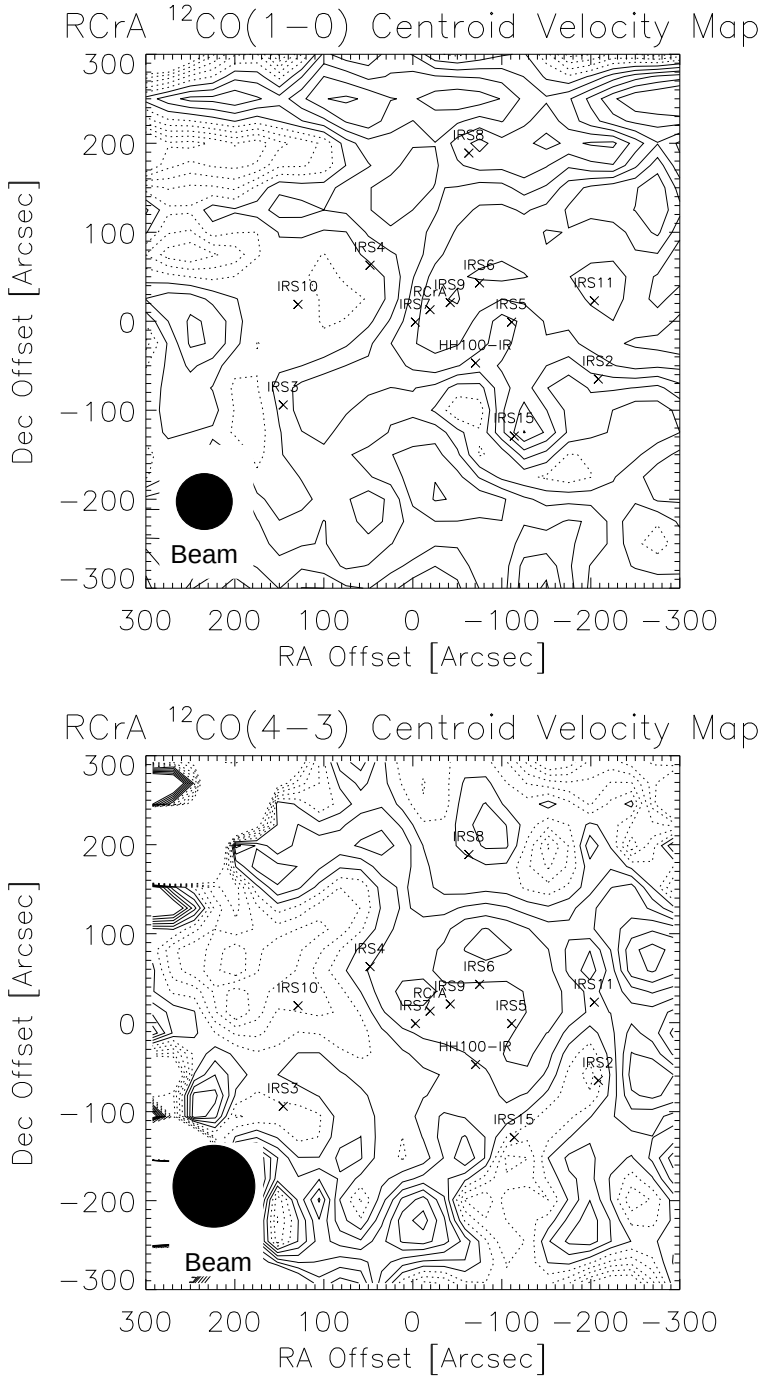

Figure 45: Centroid velocity plots for ^{12}CO(1-0) and ^{12}CO(4-3).
Dotted contours denote negative velocities. Contour spacing is 0.5 km/s.

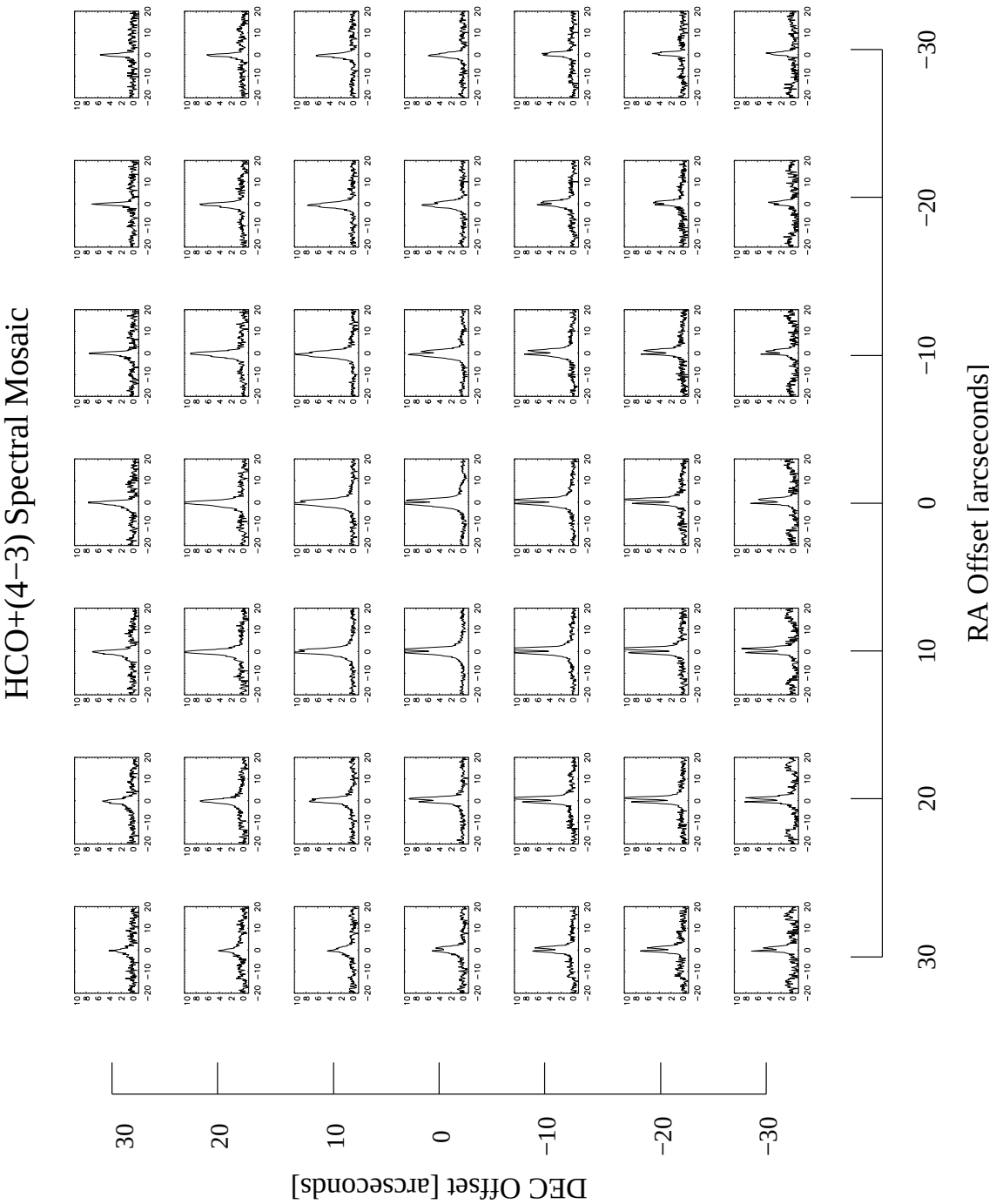

Figure 46: A spectral line mosaic in $H^{12}CO^{+}$(4-3).
Map region is the central 60x60 arcseconds of the region, centered on IRS7. The intensity axis of all the spectra is T_A^* and the y axis is velocity in km/s. The box in Figure 45 marks the location of this mosaic.

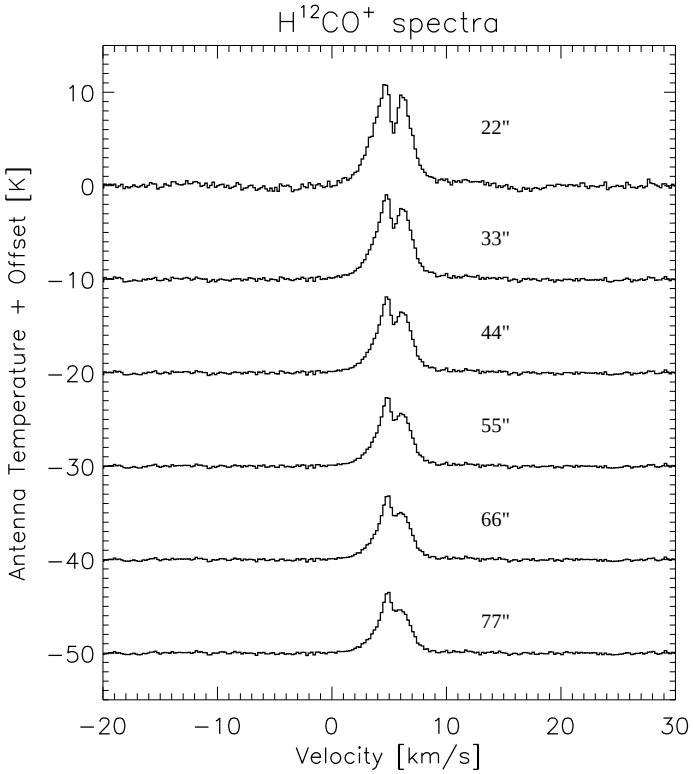

Figure 47: HCO+(4-3) spectra, centered on IRS7.
Spectra were produced from an OTF map, convolved in half beam increments from 22” to 77”.

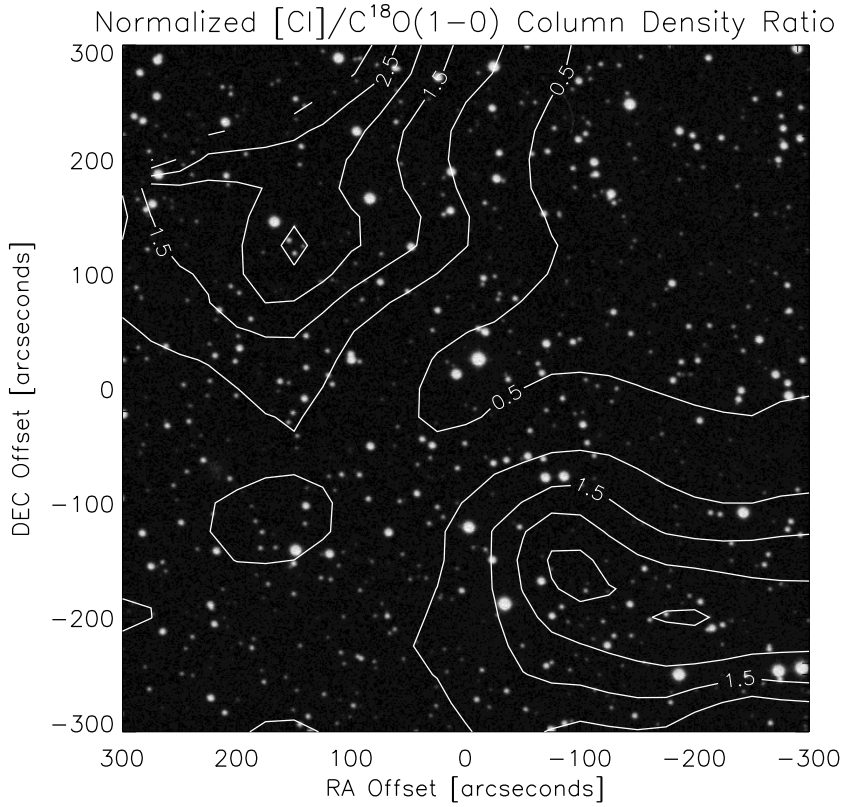

Figure 48: The normalized [CI] $^3P_1$ to $C^{18}O$(1-0) column density ratio. Contours are overlaid on a Palomar Sky Survey image of the region. In areas of high visual extinction, the abundance of [CI] drops relative to CO as expected, with and increased [CI]/CO ratio at the edges of the regions of high visual extinction.

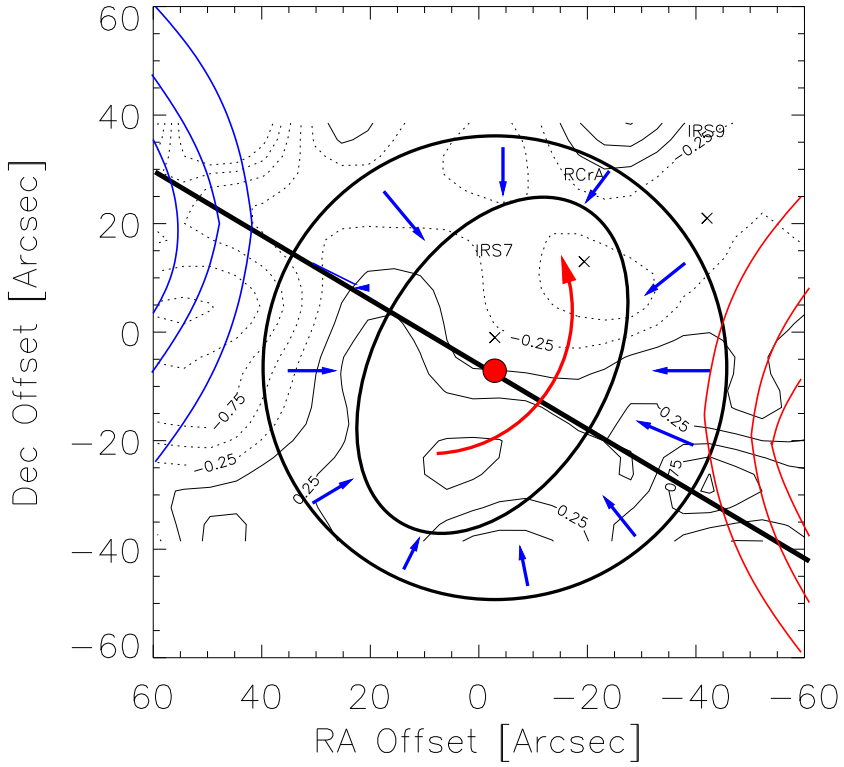

Figure 49: A cartoon of our proposed system configuration.
The contours show the combined effects of rotation, infall and outflow in great detail. We propose a class 0 source about 10” south of IRS7, surrounded by a ~2500 AU radius molecular disk at a position angle of 120 degrees. The envelope surrounding this disk shows the signs of infall kinematics. Toward the east and west edges of the map, outflow kinematics begin to dominate. The diagram is overlaid on the HCO^+(4-3) centroid velocity plot

5. VIBRATIONALLY EXCITED HCN IN PROTOPLANETARY DISKS

5.1 Introduction

The vast majority of the molecular lines observed at millimeter wavelengths are associated with the lowest vibrational state (v = 0). However, several vibrationally excited molecules have been detected in the ISM (i.e. CS, H_2, SiO, HC_3N, CH_3CN, and HCN (Turner 1987; Ziurys and Turner 1986)). For vibrational excitation to occur these molecules must be in regions of hot, dense gas (perhaps associated with a shock) and/or that are penetrated by infrared radiation. Since these excitation requirements are expected to be fulfilled in only a very compact region close to the embedded source, they make vibrationally excited molecules with submm/mm wave rotational transitions excellent probes of the physical conditions very near embedded infrared sources. This would be especially true for those sources which suffer so much extinction that they are unobservable in the infrared (Walker et al. 1994).

Initially, vibrationally excited HCN was used as a probe of physical conditions for astrochemistry studies. In 1994, Walker et al. used the fact that the critical density and energy above ground for the vibrational modes of CS were quite high ($n \sim 10^8$ cm^{-3} and 2000 K respectively) to probe protostellar disk structure. Densities and temperatures that high were unlikely to be encountered in the infalling envelope or the outflow of a protostar, or even in a smooth, quiescent disk. Since this hot, dense gas could be potentially

associated with shocks and/or spiral density waves in the protostellar accretion disk, vibrational molecular transitions could be used as a probe of disk structure and planet formation. Walker et al. detected vibrationally excited CS(7-6) and (10-9) transitions toward the protobinary object IRAS 16293 using the CSO (Walker, Serabyn, and Maloney 1994). The lines have a main beam brightness temperature of 0.13 K and 1.45 K at 340.4 and 486.2 GHz respectively. Radiative transfer calculations based on the observed line ratios and complementary v = 0 CS data indicate the v = 1 level is being collisionally excited over a 50-100 AU region. The gas excitation temperature is 2000 K. Excitation through infrared pumping is ruled out by the relatively low luminosity of the protostellar objects and the presence of a high column density dust disk. The large observed luminosities in the v = 1 lines (i.e., the large inferred size scale of the emitting region) suggest they arise in high density, shocked gas. Unless the infall accretion rate or outflow mass loss rate is extremely high ($> 2 \times 10^{-2}$ $M_\odot$ per year), the requirement of both high temperature and density forces one to the conclusion that the excitation arises within a circumstellar disk. The disk surface area over which the shock occurs is quite small, $\sim 10^{-3}$ to 10^{-4} of the total disk column. A plausible source for such shocks are self-gravitating instabilities in the disk, such as the eccentric m = 1 instability discussed by Adams, Ruden, and Shu (1989). Such instabilities are expected to occur most frequently in system where the disk to star mass ratio is high or in multiple systems where the stellar companions gravitational perturb the disk. In addition, an accretion shock could create the necessary densities and temperatures. A study of such disk instabilities would lead to a better understanding of disk evolution and the con-

ditions which are best suited for the transformation of an accretion disk into a planetary system.

This chapter builds upon that work. We have chosen to observe the v=1 and v=2 vibrational modes of HCN(4-3) rather than CS. For gas at the high temperatures necessary to collisionally excite vibrational lines, we would expect that higher J levels will be preferentially populated (Walker et al. 1994). Thus, the best compromise between atmospheric transparency and line brightness makes HCN(4-3) the best choice for finding vibrationally excited lines when accessible than lower lying rotational transitions. The critical densities of HCN are even higher than CS ($>10^{10}$ cm^{-3}), but the energy above ground for the v=1 modes are only 1050 K, half that of CS. This could make HCN an even better probe of dense material in protostellar accretion disks, probing material farther from the protostellar object. The frequencies and selection rules governing the v=1 and v=2 modes also help with observing efficiency and interpretation. HCN(4-3) v=0, both v=1 lines and the three v=2 lines can all be observed in two tunings of a 350 GHz heterodyne receiver with 1 GHz IF bandwidth. Rotational lines of HCN(4-3) in the (0, 2^0, 0), (0, 2^{2c}, 0) and (0, 2^{2d}, 0) modes, obtained simultaneously with the (0, 1^{1d}, 0) observations, will elucidate the mechanism of excitation. For example, the (0, 2^{2c}, 0) and (0, 2^{2d}, 0) modes are expected to be absent due to $\Delta l = +/-1$ selection rules if purely radiative excitation dominates. If collisional excitation dominates, requiring n ~10^{10} cm^{-3} for thermalization in the absence of radiative trapping, the intensity of (0, 2^0, 0) will clarify the temperature of the gas, since (0, 2^0, 0)

lies 2000K above the ground state, twice that of (0, 1^{1c}, 0). The energy levels and selection rules for the v=0, v=1 and v=2 modes of HCN are summarized in Figure 50. Critical densities and energy levels are also summarized in Table 6. For the collisional excitation case in a protostellar accretion disk, the brightness temperature of the emitting region is likely to be approximately the energy of the transition above ground, about 1000K for the v=1 lines.

If we are to unambiguously interpret the presence of vibrationally excited HCN emission, we need to know the excitation mechanism responsible for the emission. There are two possibilities (or actually any linear combination of these two possibilities):

a. Radiative pumping due to 14μm absorption
b. Collisional excitation in warm gas

It is possibility b that would be a tracer of the structure in accretion disks. We can use the level diagram shown at left to interpret the lines if we are able to observe both the v=1 and v=2 vibrational transitions. With a 1 GHz backend, it is possible to observe v=0 and v=(0,1^{1c},0) with one tuning, and v=(0,1^{1d},0) and all the v=2 lines in another tuning. The 2c and 2d transitions are not permitted to radiative processes, so they are a dead giveaway for extremely high density gas. Also, if the v=1 transitions are observed, and no v=2 transitions are seen, this is also a sign of a collisional process, since near LTE the v=1 level

should be much more highly populated than v=2. If the v=(0,2^0,0) line is observed and is about the same intensity as the v=1 lines, the excitation is probably purely radiative.

The emitting regions are only likely to be a small fraction of the disk. With the large beam of a single dish telescope, the observations are extremely challenging, but serve as valuable precursors to what can be achieved with submm-wave interferometers. This study could ultimately lead to a better understanding of the nature of highly excited gas in protostellar environments.

5.2 Observations

For this pilot project, we chose a sample of protostellar objects that would be likely to have bright vibrational HCN emission, either through infrared pumping, or through gravitational instabilities in a massive accretion disk. We also attempted to observe objects that were nearby. The primary target is IRAS 16293-2422, the object in which Walker et al. detected vibrationally excited CS(7-6) and (10-9) emission. This is a known low mass protobinary system with a circumbinary disk (Walker et. al.1994), and also a multiple outflow system (Walker et al. 1990). In addition we observed high mass star forming regions (AFGL 2591, S140 and Cepheus A), nearby low mass class 0 protostellar sources (L1551 and L1557) and three class I-II sources that have detectable HCN v=0 emission in other transitions (HL Tau, GG Tau and TW Hya).

Observations of the v=0 and v=(0,1^{1c},0) lines were made at the HHT in February, 2000 during a week of exceptional weather conditions. For the 6 days of the run, $\tau_{225\ GHz}$ never exceeded 0.08. We used the facility MPIfR 345 GHz dual polarization SIS receiver, with 1 GHz bandwidth AOS spectrometers with 1 MHz (0.8 km/s) spectral resolution. Observations are summarized in Table 7. Pointing was checked using planets and high flux continuum sources several times per observing session. Calibration was done using the Hot-Sky-Cold method, and observations of Orion OMC-1 were taken to compare with the spectral survey of Groesbeck et al. to compare line strengths and sideband ratios. The wobble switching observing mode was used with a 120” chopper throw, and a 50% duty cycle. Efficiency of the telescope at 350 GHz is ~0.45 for unresolved sources. Spectra were fitted with linear baselines and co-added, weighted by RMS noise using the GILDAS CLASS software package.

We tentatively detected the v=1c line in four objects, IRAS16293, Cep A, S140 and AFGL 2591. IRAS 16293 is a low mass protobinary system, but with a relatively massive and large accretion disk. It is fairly nearby as well (160 pc.) making it an excellent candidate for detection of collisionally pumped vibrational HCN emission. Cepheus A is a region of massive star formation and strong IR radiation. These observations were centered on the continuum source in the center of Cep A. This is known to be a region of massive star formation with 14 radio point sources, a strong outflow, and evidence for multiple outflow events (Narayanan 1996). This would seem to be an ideal region to radiatively pump vibrational lines of HCN, but the possibility still exists that collisional excitation is

still responsible for some of the emission. S 140 is a HII region with massive star formation and a strong IR radiation field. The source contains a cluster of deeply embedded B stars, and a large outflow apparently produced by the most luminous star in the cluster. This is a favorable environment for IR pumped vibrational HCN. AFGL 2591 is also a region of high mass star formation, and a HII region. Boonman et al. 2001 show that the HCN abundance in this object is abnormally high. The models point towards high temperatures (above 300K) effecting the chemistry such that HCN production is radically increased. Their model for this source combines collisional and radiative pumping for the vibrational levels. As expected, we were not able to detect any vibrationally excited HCN emission in the class I sources. While observations with interferometers might be able to detect this emission, the associated v=0 emission in these sources was far too weak for us to detect v=1c emission unless it was abnormally bright. IRAS 16293 was the only low mass class 0 source detected. This is not surprising given that this source is especially bright and nearby, making it a favorite for studying low mass star formation in the mm and submm wavelength regimes.

We then submitted a proposal to observe v=1d, as well as the v=$(0,2^{0},0)$, $(0,2^{2c},0)$ and $(0,2^{2d},0)$ lines in those four sources via the HHT priority queue scheduling process. Those objects were observed during times when $\tau_{225\ GHz}$ dropped below 0.05, during the 2002-2003 observing season. Calibration, pointing, observing mode and comparison spectra were taken as with the v=1c data, however both W3(OH) and Orion IRC2 were used as comparison sources. These observations are summarized in Table 8. Spectra of all the

sources for the v=0 tuning are shown in Figure 51. Spectra of the sources with v=1c detections are shown in Figure 52 through Figure 55. HCN lines are labeled in black. Lines in the frequency range of the observation in both sidebands were compiled from the JPL molecular line spectroscopy database. All lines with transition strengths greter than a factor of 6 less than that of the v=1 modes of HCN were included. Lines marked in red are in the lower sideband (used for the observations), and the lines marked in blue are in the upper sideband. Lines marked with stars have not been detected in an interstellar context (Lovas 2003).

5.3 Discussion

5.3.1 IRAS 16293

Spectra of IRAS 16293 are shown in Figure 52. Detection of the $(0,1^{1c},0)$ line is relatively clear, with a significance of 4σ. This line could be confused with SiCC, but to date this line has only been detected in AGB stars, and never in a protostellar source. In addition, during the observations, we shifted the LO frequency to determine which sideband the observed lines were in. The suspected v=1c line was in the lower sideband, not in the upper sideband as is SiCC. The v=1c line is redshifted about 4 km/s with respect to the systemic velocity of the source. Walker et al. also detected a similar velocity shift for the vibrationally excited CS line. Unfortunately, the results of the search for the v=1d line were not conclusive. We did not detect the $v=(0,1^{1d},0)$ line, and the v=2 lines are marginal

detections, at about 1.5σ. While these lines are unlikely to be confused with any other lines in the region, they could be unlucky noise. Any one line is not very convincing, but all three possible lines are at the correct frequency. The $(0,2^{2c},0)$ and $(0,2^{2d},0)$ lines are blended with two other lines, CH_3OCH_3 and $H_2{}^{13}CO$. The signal to noise is low enough that it is impossible to see if these lines, if present, have the same velocity offset as the v=1c line. We do not have a convincing explanation for why the v=1d line is not present. The weak v=2 lines, which if real, are all at the same intensity and all present point towards collisional excitation by gas at about 1000K. In this scenario, however, the v=1d line should be equal in intensity to the v=1c line. The lower limit for the intensity of the v=1d line in our spectrum is 5 mK, whereas the v=1c line has an antenna temperature of about 60 mK.

5.3.2 AFGL 2591

Spectra of AFGL2591 are shown in Figure 53. This source has an abnormally high HCN abundance (Boonman et al. 2001). We find a very bright v=0 HCN(4-3) line, as well as what seems to be extremely strong (~110 mK) HCN(4-3) v=$(0,1^{1c},0)$ emission. Given the strong IR radiation field around this source, we would expect that the emission is infra-red pumped through 14μm absorption. Observations of v=1d are enigmatic. The line is marginally detected at the 1.5σ level. No v=2 lines are present in the spectrum. This is an even more surprising result than the lack of v=1d emission in IRAS16293. The line is also about 5 times weaker than expected from the intensity of the v=1c line. We do not believe

the v=1c line could be another molecular transition, since the high HCN abundance of this object would suggest that the v=1c transition should be brighter than expected. It is again unlikely, although possible, that SiCC is present in this source.

5.3.3 Cepheus A

Spectra of Cepheus A are shown in Figure 54. We detect the v=1c line at about 50 mK intensity (6σ). The line is quite wide, with significant velocity structure. The line could be blended with at least one other unidentified line at somewhat higher frequency. The v=1d line is also clearly detected at the 50 mK level in the other tuning, detected at 5σ. No v=2 lines were detected. The v=1d line has similar width and velocity structure to the v=1c line, but is not blended. Neither line is shifted in velocity with respect to the source. If the emission in this source was excited solely by radiative pumping, we would expect to see the $v=2^0$ line at similar intensity to the v=1 lines, but it is not detected, with an upper limit of 11 mK. This points toward the conclusion that a significant amount of the vibrationally excited HCN emission in this source is from collisional processes.

5.3.4 S 140

Spectra of S140 are shown in Figure 55. We detect a very weak v=1c line, with 30 mK intensity (3σ). The line is quire narrow and does not have a velocity offset from the source. We do not detect a v=1d line, nor do we detect any v=2 lines of HCN. S140 has the

brightest v=0 HCN(4-3) emission of all our sources, and does have a strong IR radiation field, but our observations do not conclusively determine an excitation mechanism.

5.3.5 Interpretation

Detection of vibrational lines in our sources is enigmatic in all cases excepting Cep A. In S140, we fail to detect any v=1 lines except v=1c, which is extremely weak. While we expect that this source has infrared pumped vibrationally excited HCN, we cannot make any strong conclusions from our data. AFGL2591 has an extremely bright v=1c line, but virtually no v=1d line nor any v=2 lines. While the extraordinary brightness of the v=1c line can be explained by the high HCN abundance in this object, we cannot explain the lack of v=1d emission. The possibility exists that a pointing error caused the source to fall out of the beam, or the receiver was improperly tuned, but the data show no sign of improper pointing or tuning for these observations.

In IRAS 16293, the detection of vibrationally excited HCN would be important, since the infrared radiation field is three orders of magnitude too low for IR pumping of the v=1 transitions (Walker et al. 1994). We believe we have detected the v=1c line, and there are hints of the detection of all three v=2 lines, but no v=1d line is present, with an upper limit of less than 10 mK. Given the v=2 lines might not be real, pointing or tuning

errors might have lead to this problem, although there is no evidence for them. If we assume the v=1c line is indeed real, we can estimate the filling factor of the v=1 emission in the beam, and also estimate the filling factor of the circumbinary accretion disk. Assuming that the emitting gas has a brightness temperature similar to the energy above ground (1050K), the filling factor of our 22" beam is $6x10^{-5}$. Assuming a dense accretion disk diameter of 100AU (Walker et al. 1994), the areal filling factor of the emitting material in the disk is ~10%.

Cepheus A is the source with the cleanest vibrationally excited HCN emission. We clearly detect both the v=1c and v=1d lines at similar antenna temperatures (~50 mK). Both lines also have similar width and velocity structure. The v=1c line appears to be blended with another unidentified line at lower frequency. The v=1d line appears uncontaminated, and is detailed in Figure 56. No v=2 lines are detected, with a conservative upper limit of 11 mK. This points toward the conclusion that a significant component of the v=1 HCN emission from Cep A is via collisional excitation in a very high density ($n\sim10^{11}$ cm^{-3}) and hot (~1000K) environment. The v=1d line shows a double-peaked structure that could be indicative of rotation. The HCN(4-3) v=0 line shows no double peaked structure, so it is unlikely that this lineshape is due to self-absorption or infall motion. The velocity difference between the peaks is ~6 km/s, which would not be atypical of conditions in a disk around a high mass star. Narayanan et al. (1994) estimate the mass of the Cep A core to be ~330 $M_{\odot}$. If the double peaked line profile is indicative of Keplarian disk rotation, then the emitting regions of v=1 HCN(4-3) are mixed azimuthally

throughout the disk, rather than in a small number of clumps. VLA imaging shows a collection of masers about 300AU in extent that could be associated with a dense accretion disk (Torelles et al. 1998). Assuming a distance of 725 pc to the source (Johnson 1957) and optically thick emission at 1050K, the filling factor of the HCN v=1 emission is about 10%, similar to the estimates for IRAS 16293. This filling factor is with respect to the most dense part of the accretion disk where structure is most likely to form. These relatively low disk filling factors suggest clumpiness and structure in protostellar accretion disks. Assuming circular rotation at 6 km/s around a point mass at a radius of 150 AU, we estimate an enclosed mass of ~6 $M_{\odot}$. This is much lower than the 330 $M_{\odot}$ of the Cep A core, but a realistic number for a single high mass protostellar source in the core.

5.4 Summary

We have presented a novel technique for the study of protostellar accretion disks through the use of vibrationally excited HCN(4-3). While this technique has been used before with vibrationally excited CS(7-6), HCN has several advantages. The energy above ground of HCN(4-3) v=1 is 1050K, half that of vibrationally excited CS, while the critical density similar at ~10^{11} cm^{-3}. This allows us to probe regions of protostellar accretion disks farther from the protostellar source. In addition, selection rules for v=1 and v=2 HCN emission allow us to determine the excitation mechanism independent of any other observations or assumptions, while observation of the v=2 lines also helps constraint the temperature of the gas since the energy above ground for these transitions is 2100K. The

v=0, v=(0,1^{1c},0), v=(0,1^{1d},0), v=(0,2^{0},0), v=(0,2^{2c},0) and v=(0,2^{2d},0) lines can all be observed in two tunings of a 350 GHz heterodyne receiver system with a 1 GHz IF bandwidth. Contamination by other molecular lines is minimal, even with double sideband receiver systems.

Beam dilution makes these observations difficult with single dish sub-mm wave telescopes. The brightest v=1 line we detected is just over 100 mK antenna temperature, with most lines around 50 mK. Out of 9 sources, we detected vibrationally excited emission in 4 sources, IRAS 16296, AFGL 2591, S140 and Cepheus A. Only in Cepheus A did we obtain conclusive results. Both the v=1c and v=1d lines are present, with similar intensity and velocity structure. We do not detect any v=2 lines. This suggests excitation by ~1000K dense (n~10^{11} cm^{-3}) gas, with less than 20% contribution from IR pumping. The filling factor in the disk of this emission, assuming a 300AU disk diameter is ~10%. The line profile suggests Keplarian disk rotation at characteristic rotational velocity of 6 km/s. If we assume the v=1c line we see in IRAS 16293 is real, we determine a similar disk filling factor assuming a 100AU disk diameter. These observations show the power of this technique for probing the most dense parts of protostellar accretion disks without spatially resolving their structure. With the next generation of sub-mm wave interferometers, this technique will be far more powerful. The 0.4” spatial resolution of the SMA could yield HCN(4-3) v=1 antenna temperatures in excess of 100K if the emitting region remains unresolved. With dramatically increased signal to noise, many more sources will be open

for study by this technique, and line profiles will be detailed enough to allow in depth study through radiative transfer modelling.

Transition	Energy above ground [K]	n_{crit} [cm^{-3}]
HCN(4-3) v=0	43K	10^7
HCN(4-3) v=1	1050K	~10^{11}
HCN(4-3) v=2	2100K	~10^{12}

Table 6: Energies and critical densities for the v=0, v=1 and v=2 bending modes of HCN(4-3).

Source	Type	RMS Noise [mK]
IRAS 16293	Class 0	15
L1527	Class 0	10
L1551	Class 0	11
GG Tau	Class I	9
HL Tau	Class I	18
TW Hya	Class I	16
Cep A	[HII]	8
S140	[HII]	9
AFGL 2591	[HII]	14

Table 7: HCN(4-3) v=0 and v=1c observations.

Source	Type	RMS Noise [mK]
IRAS 16293	Class 0	5
Cep A	[HII]	11
S140	[HII]	10
AFGL 2591	[HII]	13

Table 8: HCN(4-3) v=1d and v=2 observations.

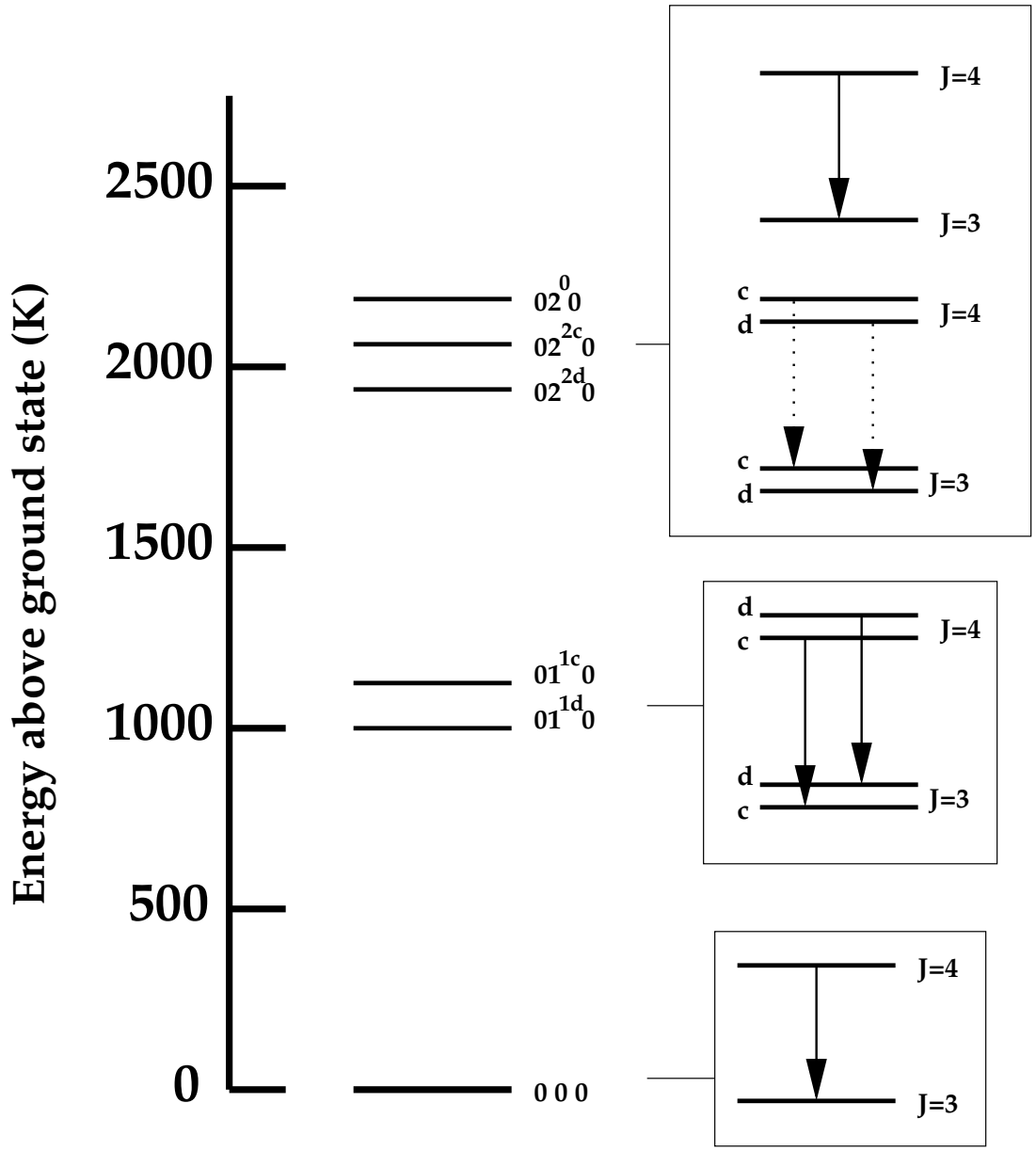

Figure 50: An energy level diagram for two ro-vibrational transitions of HCN(4-3). The $(0,1^{1c},0)$ and $(0,1^{1d},0)$ modes are a modest 1050K above ground, compared to the v=2 modes. The panels on the right show the selection rules for the transitions. The $(0,2^{2c},0)$ and $(0,2^{2d},0)$ transitions are not permitted for the radiative pumping excitation mechanism.

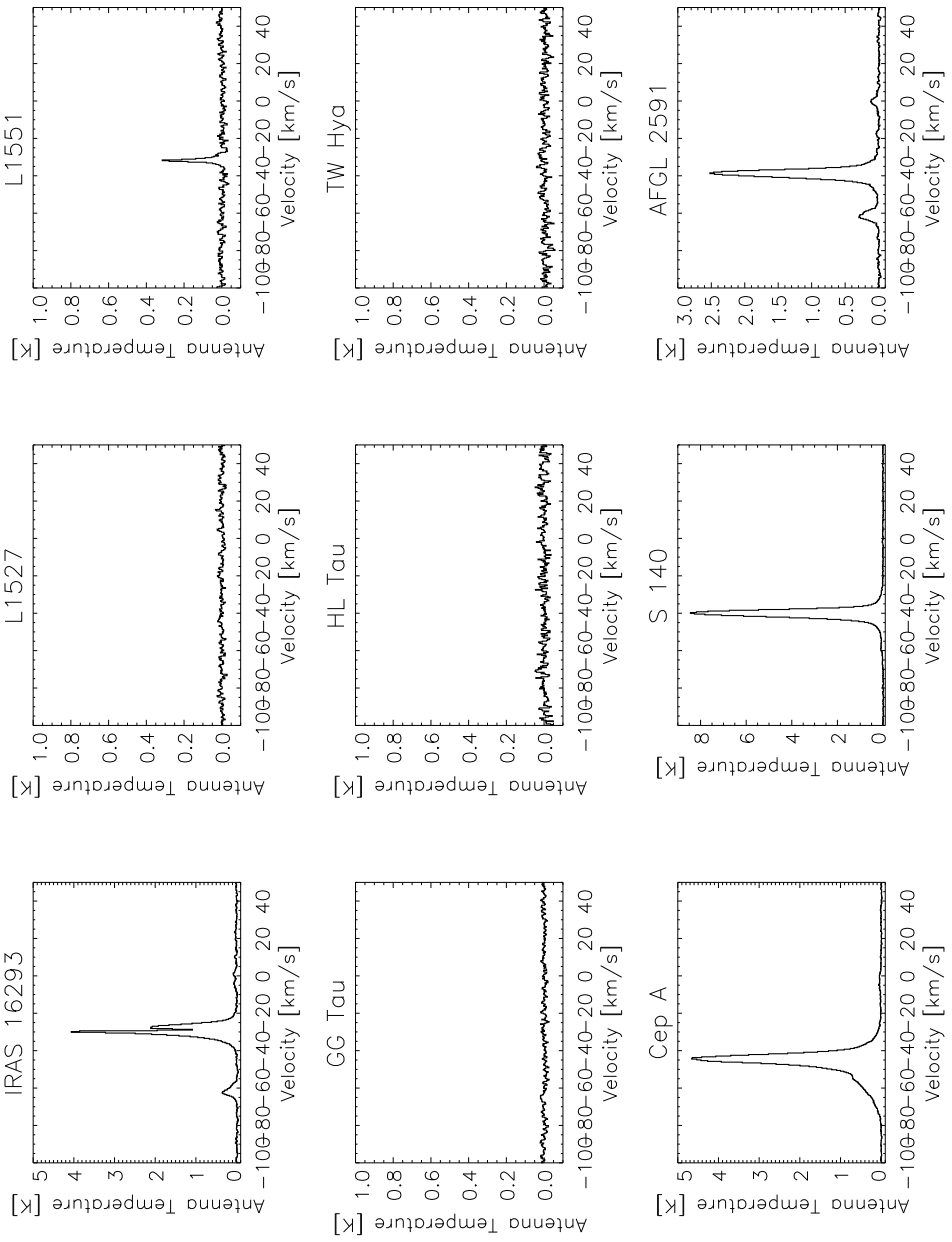

Figure 51: Spectra of all 9 sources we observed in February, 2002.
In 5 out of 9 sources, HCN(4-3) v=0 was detected. HCN(4-3) v=1c was detected in 4 of the 9 sources, as detailed in Figure 52 through Figure 55.

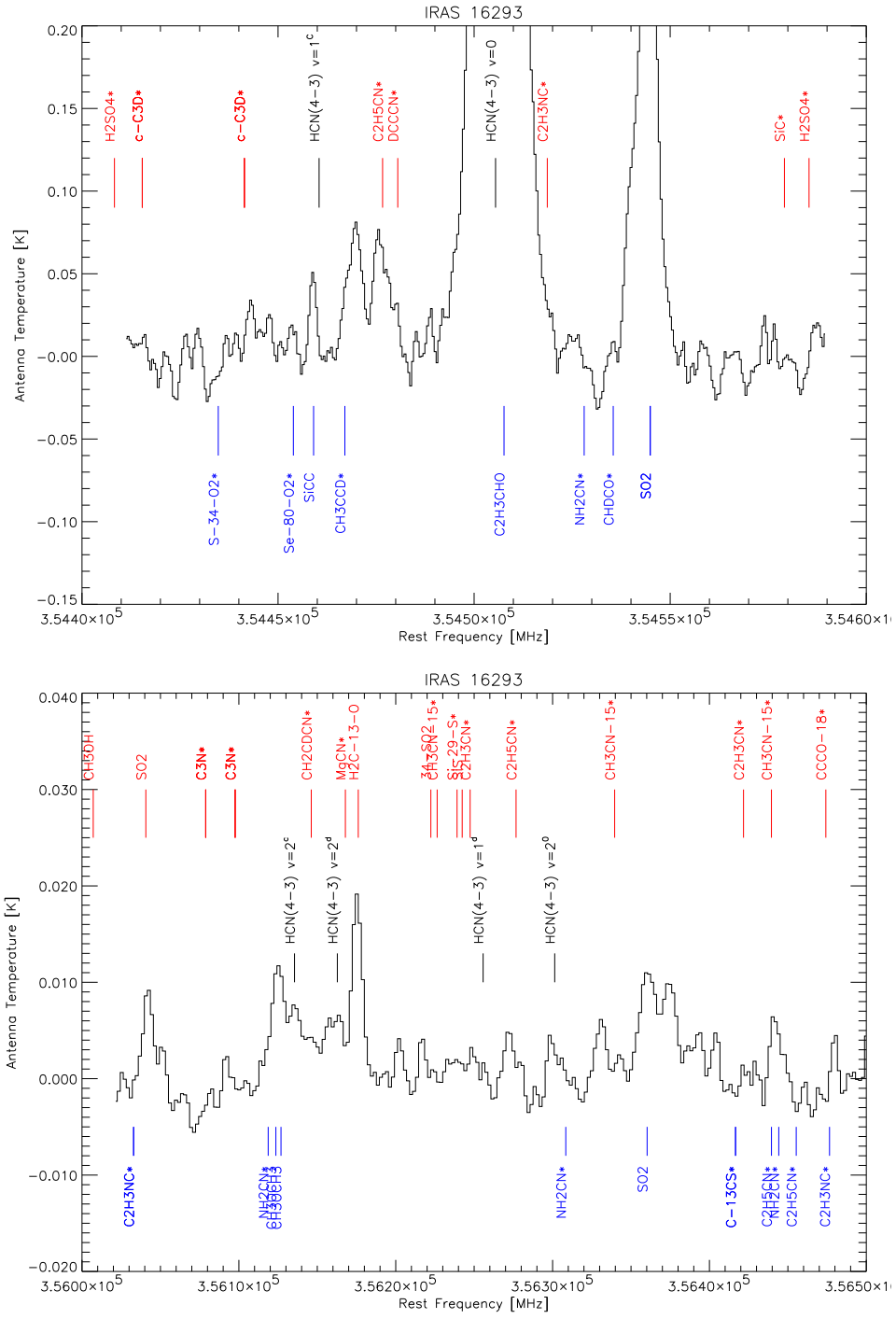

Figure 52: Spectra of IRAS 16293.
The top panel is tuned for HCN(4-3) v=0 and v=1c, while the bottom contains v=1d and the v=2 lines. USB lines are marked above, LSB below. Stars denote no interstellar detections.

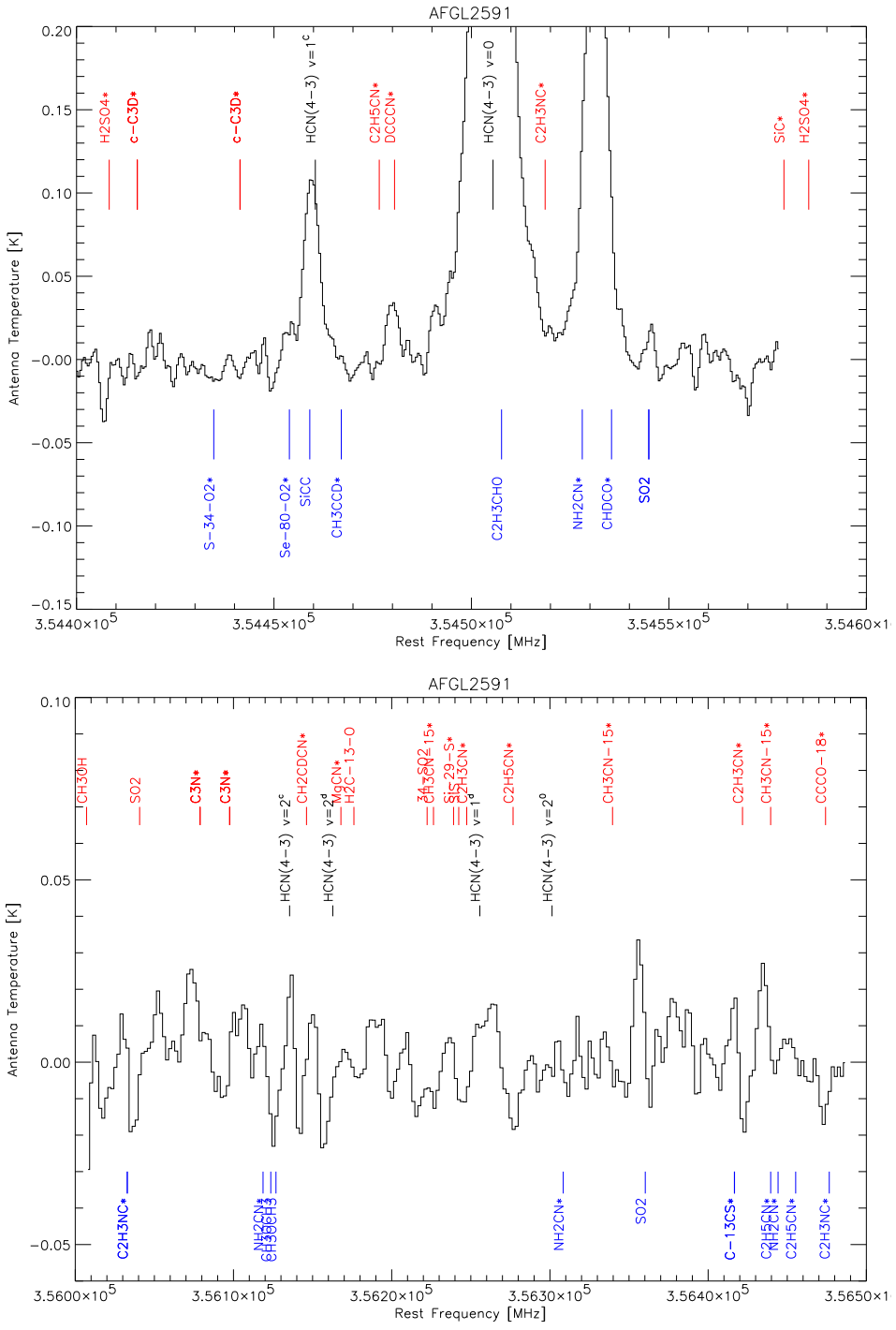

Figure 53: Spectra of AFGL 2591, with the same tuning as Figure 52.

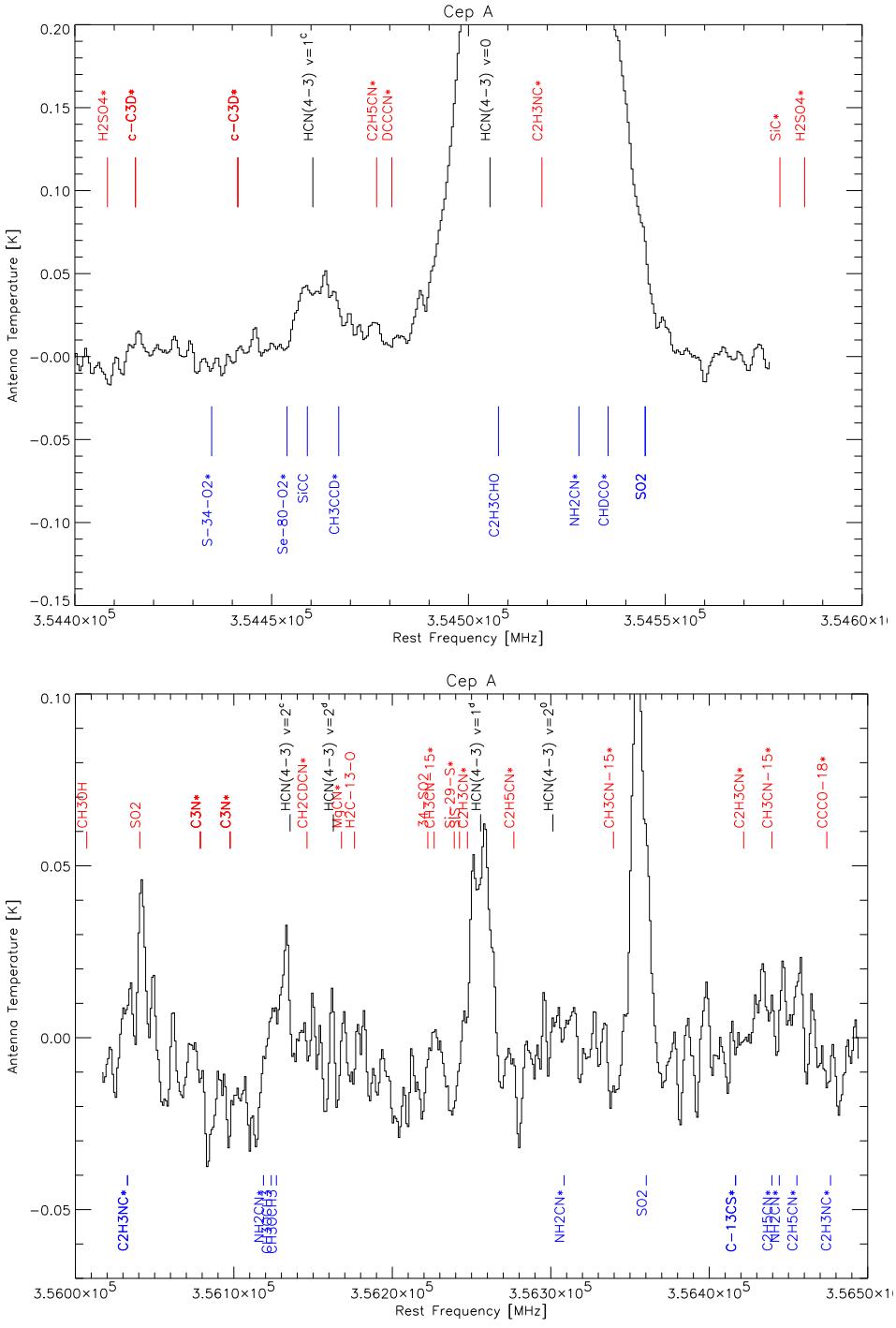

Figure 54: Spectra of Cep A, with the same tuning as Figure 52.

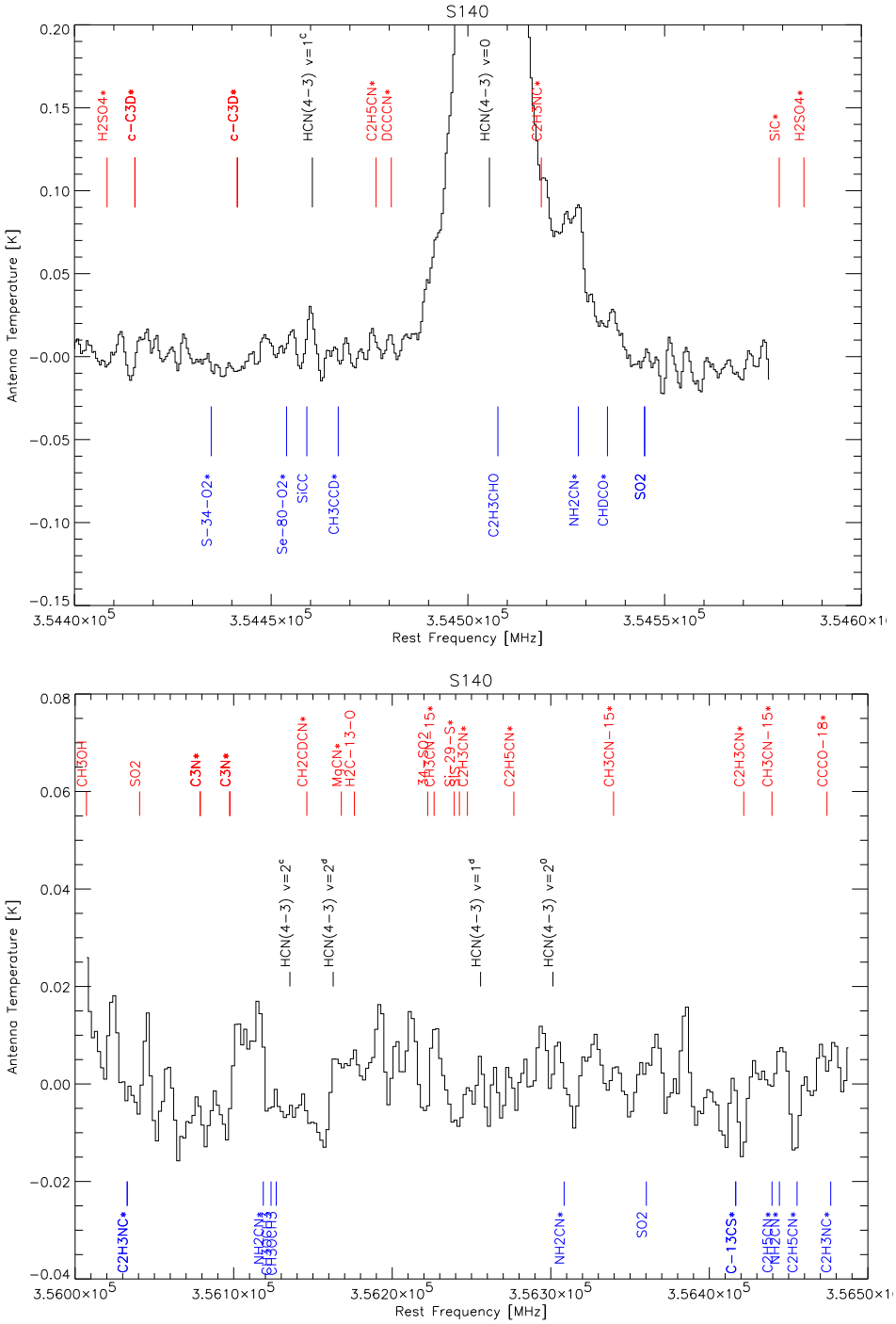

Figure 55: Spectra of S140 with the same tuning as Figure 52.

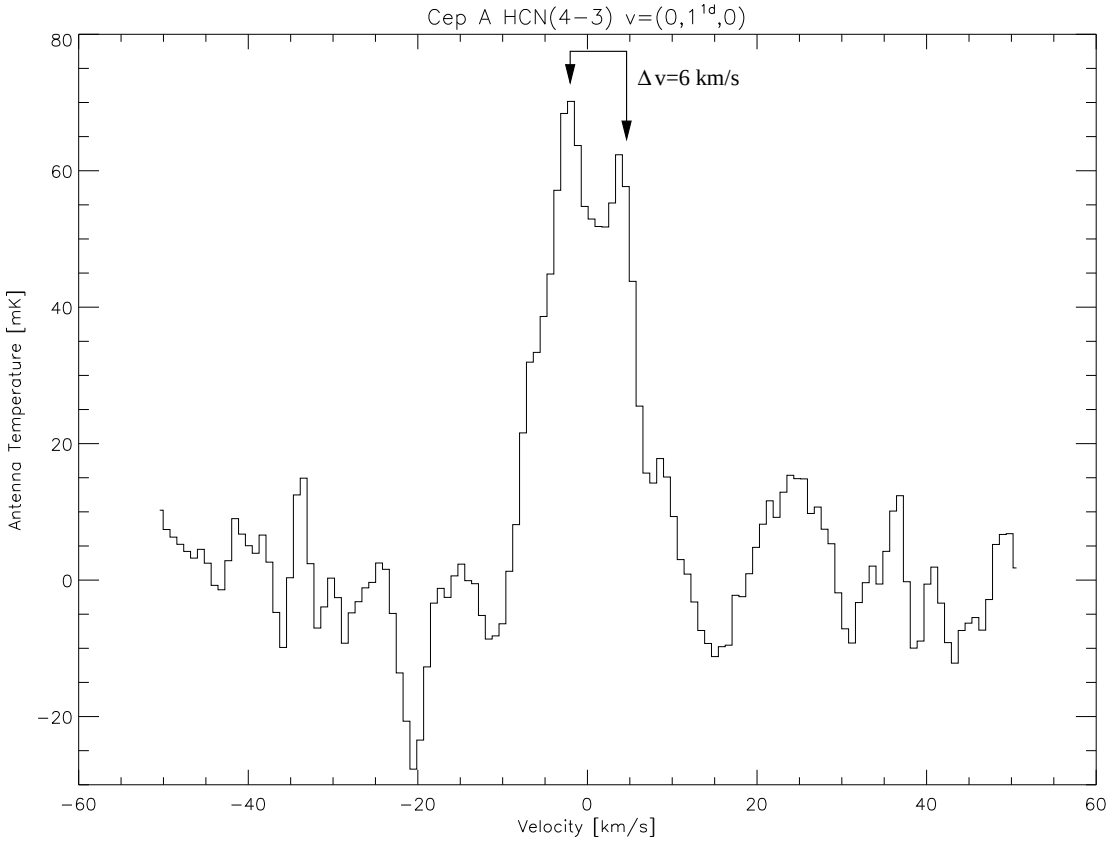

Figure 56: The v=(0,1^{1d},0) line in Cepheus A, at 0.8 km/s velocity resolution.
The line appears to be double peaked, which might be the sign of disk-like rotation, The velocity offset between peaks is 6 km/s. RMS noise level is 11 mK.

6. CONCLUSION

In this thesis, I have presented two heterodyne array receiver systems built at SORAL, and two submillimeter wave studies of star formation from the size scales of protostellar accretion disks to molecular outflows. The combination of technology and science is still the driving force behind new discoveries in the submillimeter, and will continue to provide new insight into the star formation process.

6.1 Summary

We have constructed a 2x2, 810 GHz array receiver for the AST/RO telescope. The array utilizes a common set of re-imaging optics, an efficient 4-way quasi-optical LO power splitter, a solid-state LO, low noise mixers, a flexible computer controlled bias system, and an array AOS. A state-of-the-art planar, tunerless LO chain with W-band power amplifiers can easily pump all the mixers with only a 0.5 mil Mylar LO diplexer. Upgrades and repairs have reduced the receiver noise temperatures to between 625K and 640K per mixer, making the system ~15 times faster for mapping than the previous 810 GHz system on the AST/RO telescope.

DesertStar is a 345 GHz, 7 pixel heterodyne array receiver for use on the Heinrich Hertz Telescope on Mt. Graham in Arizona. The instrument uses fixed backshort, suspended stripline SIS mixers with 2 GHz IF bandwidth. Cooling is provided by a high capacity closed cycle refrigerator in a large, expandable cryostat. We have demonstrated

proper operation of the cryogenic system and computer controlled bias system. Measurements indicate the array mixer can provide uncorrected receiver noise temperatures of ~60K-70K from 326-356 GHz. Performance has been verified in the JT cryostat with 3 mixers, and the instrument has had a engineering run on the HHT, where it successfully collected data. We will be continuing to add mixers to the cryostat, and plan to have the instrument operational in the lab with 7 pixels in fall, 2003, as well as return to the telescope for further testing.

We have observed the molecular core near R CrA in ^{12}CO(1-0), ^{13}CO(1-0), C^{18}O(1-0), ^{12}CO(3-2), ^{12}CO(4-3), [CI] $^3P_1$, H^{12}CO$^+$(4-3), H^{13}CO$^+$(4-3) and 870 μm continuum. This varied data set points toward the conclusion that the source for the FIR line and continuum emission, and the driving source for the molecular outflow might be a yet unidentified class 0 source deeply embedded in the cloud, not the class I source IRS7 as previously thought. We use the HCO^+ measurements and the continuum measurements to estimate the envelope mass at the peak of the FIR emission, and find a gas mass of about 0.5 $M_\odot$. We also use the centroid velocity of HCO^+ to estimate the enclosed mass inside the rotating molecular disk to be ~0.75 $M_\odot$. Both these measurements suggest a low mass (0.5 $M_\odot$) protostar surrounded by an envelope of similar mass. In addition, the FIR SED yields a luminosity of 21 $L_\odot$ from cold dust, which is also consistent with a low mass protostar. These estimates are consistent with a class 0 source. In addition, the peak of the FIR

line and continuum emission is not centered on IRS7, but is offset ~10”to the south, as is the center of rotation derived from the HCO^+ velocity gradient.

The interaction of rotation, infall and outflow are all visible in the high spatial resolution HCO+ map of the central region of the cloud. Lineshapes show evidence for all three motions in the central 60”x60” of the map. A slice through the centroid velocity plot along the major axis of the molecular disk reveals a clean signature of rotation.The HCO^+ lineshapes and centroid velocity plots also show clear evidence for infall motions, with blue peaked line profiles at the center of the map, even when convolved to large beam-sizes. In addition the centroid velocity plot shows the “Blue Bulge” signature of infall. We calculate a mass infall rate of $\sim 10^{-5}$ $M_\odot$/yr. The molecular outflow is detected in CO(1-0), CO(4-3), HCO^+(4-3) and [CI] $^3P_1$. We trace the outflow to the edge of our 10’x10’ mapped region. In the small 120”x80” HCO^+ map, we only see signs of outflow at the east and west edges of the map, since infall and rotation kinematics dominate in the central region. We have estimated the outflow mass an energetics using both CO(1-0) and CO(4-3). These estimates bracket the likely values for these parameters in the outflow system. The outflow mass is ~0.7 $M_\odot$, similar to the mass of the protostar we believe is driving the outflow. The energetics are typical for a molecular outflow around a young, low mass protostar, with a mechanical luminosity much less than the FIR luminosity.

The result is a picture of typical low mass star formation, but in a region with young, higher mass stars. We believe continued study of this system is important due to the high spatial resolution available. The system shows all the kinematic signatures of a class 0 system, and high spatial resolution allows us to disentangle all the effects normally blurred together in more distant sources. Follow-up with mm-wave interferometers in both continuum and high density molecular tracers could reveal the class 0 source, if present, and allow detailed study of the infall and rotational motions of a highly resolved molecular disk. Physical resolutions of better than 200 AU are easily obtainable. This is a difficult observation for interferometers located in the northern hemisphere, but this source provides the opportunity to study a young protostar with a minimum of complications.

We have presented a novel technique for the study of protostellar accretion disks through the use of vibrationally excited HCN(4-3). While this technique has been used before with vibrationally excited CS(7-6), HCN has several advantages. The energy above ground of HCN(4-3) v=1 is 1050K, half that of vibrationally excited CS, while the critical density similar at ~10^{11} cm^{-3}. This allows us to probe regions of protostellar accretion disks farther from the protostellar source. In addition, selection rules for v=1 and v=2 HCN emission allow us to determine the excitation mechanism independent of any other observations or assumptions, while observation of the v=2 lines also helps constraint the temperature of the gas since the energy above ground for these transitions is 2100K. The v=0, v=(0,1^{1c},0), v=(0,1^{1d},0), v=(0,2^{0},0), v=(0,2^{2c},0) and v=(0,2^{2d},0) lines can all be observed in two tunings of a 350 GHz heterodyne receiver system with a 1 GHz IF band-

width. Contamination by other molecular lines is minimal, even with double sideband receiver systems.

Beam dilution makes these observations difficult with single dish sub-mm wave telescopes. The brightest v=1 line we detected is just over 100 mK antenna temperature, with most lines around 50 mK. Out of 9 sources, we detected vibrationally excited emission in 4 sources, IRAS 16296, AFGL 2591, S140 and Cepheus A. Only in Cepheus A did we obtain fully conclusive results. Both the v=1c and v=1d lines are present, with similar intensity and velocity structure. We do not detect any v=2 lines. This suggests excitation by ~1000K dense ($n \sim 10^{11}$ cm^{-3}) gas, with less than 20% contribution from IR pumping. The filling factor in the disk of this emission, assuming a 300AU disk diameter is ~10%. The line profile suggests Keplarian disk rotation at characteristic rotational velocity of 6 km/s. If we assume the v=1c line we see in IRAS 16293 is real, we determine a similar disk filling factor assuming a 100AU disk diameter. These observations show the power of this technique for probing the most dense parts of protostellar accretion disks without spatially resolving their structure. With the next generation of sub-mm wave interferometers, this technique will be far more powerful. The 0.4” spatial resolution of the SMA could yield HCN(4-3) v=1 antenna temperatures in excess of 100K if the emitting region remains unresolved. With dramatically increased signal to noise, many more sources will be open for study by this technique, and line profiles will be detailed enough to allow in depth study through radiative transfer modelling.

6.2 Future Work

6.2.1 DesertStar

The DesertStar receiver was designed from the beginning to support expansion, including an entire second mixer array for the orthogonal linear polarization at 345 GHz or a different frequency. One of the most powerful projects for this array is to conduct a fully sampled galactic plane survey of the 1st quadrant of the galaxy in ^{12}CO and ^{13}CO. Ideally we would like to simultaneously collect both CO(3-2) and CO(2-1) data. To this end, we plan to equip DesertStar with a second mixer array of four 230 GHz balanced, sideband separation mixers (Walker et al. 2003). These mixers, designed by Anthony Kerr of NRAO, require far less LO power than single ended mixers. While the design uses four SIS junctions, theoretically requiring four times the LO power, the LO is injected via waveguide through hybrid couplers, allowing very efficient use of 100% of the LO power provided. In addition, the mixers separately downconvert both the upper and lower side-bands, sending them through independent IF chains. These mixers have already been developed and tested, and offer exceptional performance, with SSB T_{rec}~60K (Kerr 2003). Mounting for the two mixer arrays is shown in Figure 57. The 45 degree flat mirror in the cryostat need only be replaced with a linear wire grid, allowing one linear polarization to pass to the 230 GHz mixer array, with the other reflecting off the grid to the 345 GHz array.The quasioptical LO injection used for the 345 GHz array is unaffected by this addition. No LO multiplexing is required, since the 230 GHz mixers will be fed the LO signal via waveguide from a multiplier in the cryostat on the 40K radiation shield. The resulting

dual frequency array receiver will be the first of it's kind at any frequency, and will be a uniquely powerful tool virtually all types of mapping.

6.2.2 Integrated THz Arrays

Experience with PoleStar and DesertStar has shown that expanding heterodyne arrays past a few tens of pixels using the conventional technique of stacking mixer blocks in the focal plane becomes intractable. We have been working on the development of integrated focal plane arrays that combine the technologies of silicon micromachining, semiconductor silicon processing, Microwave Monolithic Integrated Circuits (MMICs) and high speed digital electronics that can produce arrays of ~100 pixels at greatly reduced cost per pixel and reduced complexity. The use of silicon micromachining makes this idea suitable for THz applications. Through use of the instrument at the prime focus of compatible telescopes, or through re-imaging optics, the input F number can be kept low. Since the spacing between pixels in a heterodyne array is $2F\lambda$ for 20 dB isolation between pixels, a low F number feed can produce a very compact mixer array. The mixer array is composed of stacks of linear arrays. Each linear array is composed of three modules: the horn block, the detector block and the backshort block (Figure 58). Both the horn block is produced via silicon micromachining. The detector block consists of arrays of SIS junctions or Hot Electron Bolometer mixers fabricated on membranes supported by a silicon frame. The backshort pedestals are produced via wet etching of silicon, with laser machined backshort cavities. The final structure is all silicon, and is self aligning. This design can be

scaled to in excess of 4 THz, well into the far infrared. The completed array is then mounted in an “array motherboard” structure. These nested rings of circuit boards are connected with microstrip ribbon cables, and are thermally isolated. All IF and bias signals are conveyed to and from the mixer array via microstrip and circuit traces on the boards and connecting ribbon cables. This minimizes the number of connections, greatly simplifying the construction of the instrument, and increasing reliability. Rather than use amplifiers connected with semi-rigid coaxial cable, surface mounted amplifiers are built directly on the motherboard structure. No wires or cables are used anywhere except on the room temperature stage of the motherboard. Figure 59 shows a concept for a complete 100 pixel array at 810 GHz for the Large Binocular Telescope. With 100 IF signals, backend spectrometers could become a problem. Conventional AOS, filter back or autocorrelation spectrometers are too large, power hungry and costly to serve 100 IF signals. Modern Field Programmable Gate Arrays (FPGAs), and the dramatic increase in speed of moderately priced computers now allows us to buy a 100 channel digital autocorrelation spectrometer with 2 GHz of IF bandwidth per channel for less than $500,000. Such a system, based on already developed technology, would occupy half a standard equipment rack and require only 1kW of power to run. Efforts to develop all these technologies are ongoing at SORAL, and have direct application to both ground and space based sub-mm and FIR applications.

6.2.3 R CrA

This work has shown R CrA to be a very promising laboratory for studying the early phases of star formation at high spatial resolution. We plan to continue work with the AST/RO telescope this observing season. PoleStar will be fully operational this next season, with the supershorted mixer repaired. The resulting factor of ~20 improvement in mapping speed over WANDA will allow us to make a fully sampled, 10x10 arcminute map of the region in CO(7-6) and [CI] $^3P_2$. This data will be important, since it will pin down the rotational level population for the CO, allowing for multi-transition, non-LTE analysis of the outflow gas. In addition, the column density and excitation of the atomic carbon can be determined far better than with the current data, which forces the assumption of optically thin, LTE conditions. Due to the 50% smaller beam and somewhat lower atmospheric transparency at 810 GHz, a 10x10 arcminute map made with previous generation receiver systems would be very resource intensive. With PoleStar, the project becomes no more difficult than the 460/492 GHz observations we already have.

The molecular disk in the R CrA cloud will be an important target for future interferometers. For the SMA at 356 GHz, the field of view will be 37.” This means it will take a mosaic of several pointings to fully cover the molecular disk. There will be ~500 resolution elements across the major axis of the disk, allowing an unprecedented look at such a structure. Currently, no northern hemisphere mm-wave or sub-mm wave interferometer, save the SMA can see far enough south to observe R CrA. It would be possible to use the

VLA to observe CS(1-0) in this source, at 49 GHz. While the first observation might be done in the early stages of operation of the SMA in guaranteed time mode, observation of this disk in high density tracers will yield results long into the future. In the mean time, the VLA might be able to reveal important information about this disk.

6.2.4 Vibrationally Excited Lines

The true promise of using vibrationally excited lines as a tracer for accretion disk structure will be realized through the use of interferometers. With a single dish telescope, the beamsize is vastly larger than the emitting regions. We estimate emitting regions of a diameter far less than 50 AU, although the clumps responsible for the emission are probably spread throughout the disk. With an interferometer, beam dilution will be greatly reduced, or possibly eliminated as the resolution of future interferometers is able to resolve the emitting regions. The optimum tools for this future study will be the SMA and ALMA. As shown in section 5.1, higher J lines are preferentially populated when the emitting gas is hot. This favors the use of sub-mm wave interferometers over existing mm-wave interferometers. HCN(4-3) v=1 will probably be the optimal combination of line brightness and atmospheric transparency, but good weather at the ALMA site could favor observation of HCN(7-6) at 623 GHz. In the mean time, it will be possible to use existing mm-wave interferometers to observe HCN(3-2) (BIMA, OVRO) and CS(1-0) (VLA). We plan to continue this work, proposing to observe the four sources we have already detected in CS(1-0) v=1 at the VLA. Unfortunately, BIMA and OVRO will be off line for some

time as they are moved and combined into CARMA. Shortly, SMA will be available for 350 GHz observations, making it the optimal tool for this work until ALMA begins to come on line in 2008. These interferometric observations will be combined with radiative transfer modeling of both simple model disks, and results from numerical hydrodynamic simulations. We hope to predict line profiles and intensities with the hope of someday being able to invert observed line profiles to yield information about accretion disk structure and planet formation.

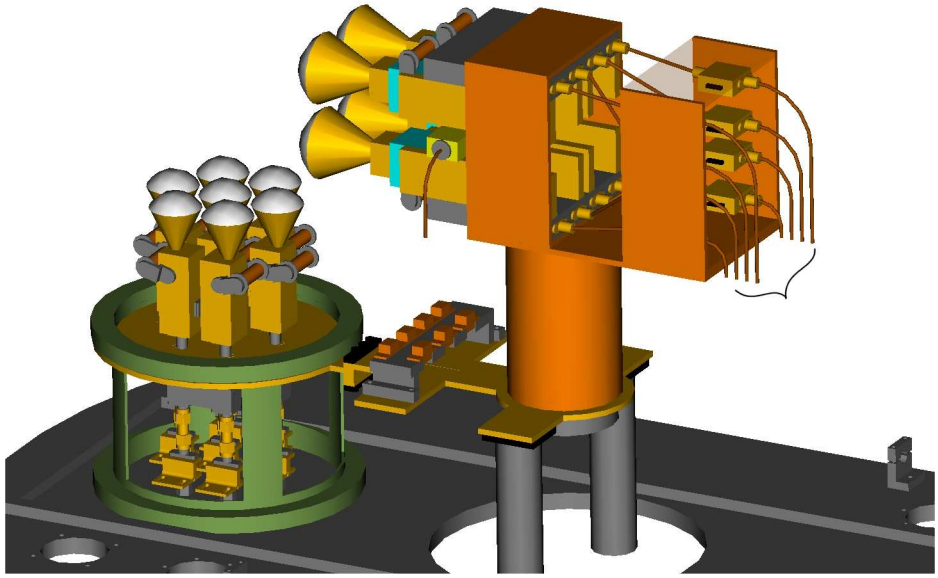

Figure 57: Expansion to DesertStar
This expansion adds four balanced, sideband seperation mixers at 230 GHz. Diplexing is accomplished through the use of a linear wire grid in place of the flat mirror currently in the system (3D model courtesy Dathon Golish).

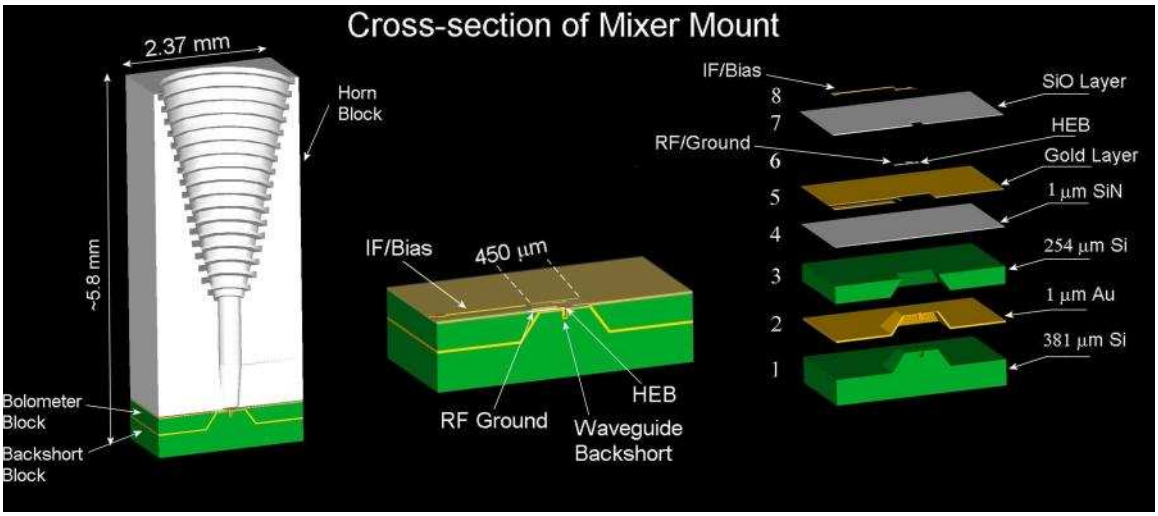

Figure 58: An integrated silicon micromachined array mixer design.
All layers can be fabricated with a combination of photolithography, silicon micromachining and wet etching (Figure courtesy Dathon Golish).

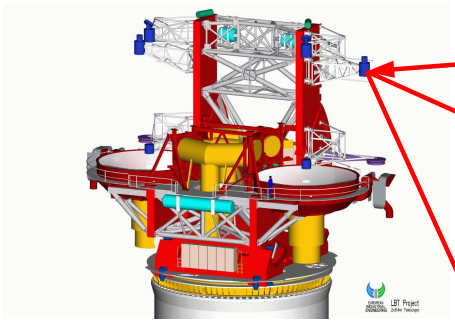

SuperCam prime focus location

The SuperCam prime focus location on the LBT. Each mirror is 8.4m in diameter; standing in front of the right mirror is a person for scale. Swingarms can be deployed in a matter of minutes to take advantage of the best submillimeter weather.

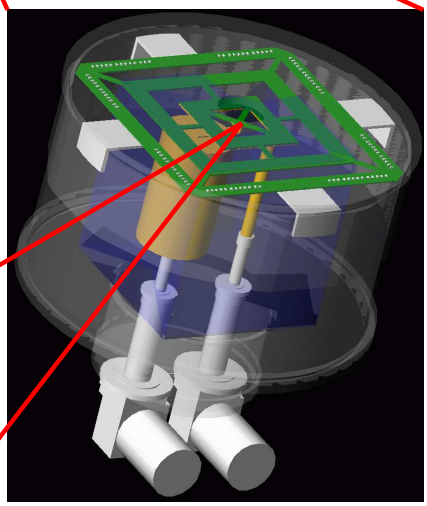

The SuperCam cryostat, showing the nested frame concept for cryogenic isolation. The central region is cooled to ~4K with a mechanical refrigerator. The next two frames are cooled to 12K and 60K with another mechanical refrigerator. The outer frame is at room temperature and contains all the connectors to the outside world.

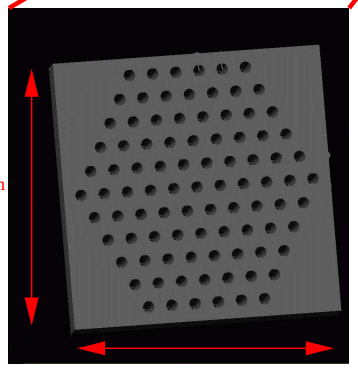

The 100 pixel array of laser micromachined dual mode feedhorns. HEB devices will be fabricated on a silicon nitride membrane with a silicon frame. Backshorts are machined in a third silicon layer. The three layers are sandwiched together to produce the complete mixer array.

Figure 59: Design concept for a 100 channel, 810 GHz receiver system.

REFERENCES

Adams, F. C., Ruden, S. P., and Shu, F. H., *Eccentric gravitational instabilities in nearly Keplerian disks*, ApJ, 347, 959, 1989.

Adelson, L.M., & Leung, C.M., *On the Effects of Rotation on Interstellar Molecular Line Profiles*, BAAS, 14, 606, 1982.

Anderson, I.M., Harju, J., Knee, I.B.G., Haikala, L.K., *A Molecular Disk and Dense Outflow in Corona Australis*, A&A, 321, 575, 1997.

Anderson, I.M., Harju, J., & Haikala, L.K., *HCO^+ (J=4-3) Mapping of the Molecular Disk Around IRS7 in Corona Australis*, A&A, 326, 366, 1997.

Anderson, I.M., Caselli, P., Haikala, L.K., & Harju, J., *Deuterium Fractionation and the Degree of Ionization in the R Coronae Australis Molecular Cloud Core*, A&A, 347, 983, 1999.

Baars, J. W. M., Martin, R.N., Mangum, J.G., McMullin, J.P., Peters, W.L. *The Heinrich Hertz Telescope and the Submillimeter Telescope Observatory*, PASP, Volume 111, Issue 759, 1999.

Bally, J., & Lada, C.J., *The High Velocity Molecular Flows Near Young Stellar Objects*, ApJ, 265, 824, 1983.

Blundell, R., Tong, C-Y.E., Papa, D.C., Leombruno, R.L., Zhang, X., Paine, S., Stern, J.A., LeDuc, H.G. & Bumble,B., *Wideband fixed-tuned SIS receiver for 200 GHz operation*, IEEE MTT Symp. on Space Terahertz Technology,Vol. 43, 1995.

Boonman, A. M. S., Stark, R., van der Tak, F. F. S., van Dishoeck, E. F., van der Wal, P. B., Schäfer, F., de Lange, G., Laauwen, W. M., *Highly Abundant HCN in the Inner Hot Envelope of GL 2591: Probing the Birth of a Hot Core?*, ApJ, 553, L63, 2001.

Dent, W.R.F., *HARP & ACSIS on the JCMT*, Imaging at Radio Through Submillimeter Wavelengths, ASP Conference Proceedings Series, Vol. CS-217, 2000.

Dickman, R.L., *The Ratio of Carbon Monoxide to Molecular Hydrogen in Interstellar Dark Clouds*, ApJSS, 37, 407, 1978.

Dotson, J.L., Novak, G., Renbarger, T., Pernic, D., & Sundwall, J.L. *SPARO: the submillimeter polarimeter for Antarctic remote observing*, Proc. SPIE Vol. 3357, 1998.

REFERENCES - *Continued*

Draine, B.T. & Lee. H.M., *Optical Properties of Interstellar Graphite and Silicate Grains*, ApJ, 285, 89, 1984.

Giannini, T. et al., *ISO-LWS Observations of Herbig Ae/Be Stars II. Molecular Lines*, A&A, 346, 617, 1999.

Graf, U. U., Haas, S., Honingh, C. E., Jacobs, K., Schieder, R., Stutzki, J., *Array receiver development at KOSMA for the submillimeter and terahertz spectral range*, Proc. SPIE Vol. 3357, 1998.

Groesbeck, T.D., *The Contribution of Molecular Line Emission to Broadband Flux Measurements at Millimeter and Submillimeter Wavelengths*, Ph.D. Thesis, California Institute of Technology, 1995.

Groppi, C.E. et al., *Pole STAR: An 810 GHz Array Receiver for AST/RO*, Imaging at Radio Through Submillimeter Wavelengths, ASP Conference Proceedings Series, Vol. CS-217, 2000.

Gusten, R., *First Results with CHAMP, the Carbon Heterodyne Array of the MPIfR*, Imaging at Radio Through Submillimeter Wavelengths, ASP Conference Proceedings Series, Vol. CS-217, 2000.

Harju, J., Haikala, L.K., Mattila, K., Mauersberger, R., Booth, R.S., & North, H.L., *Large Scale Structure of the R Coronae Australis Cloud Core*, A&A, 278, 569, 1993.

Henning, T., Launhardt, R., Steinacker, J., & Thamm, E., *Cold Dust Around Southern Herbig Ae/Be Stars*, A&A, 291, 546, 1994.

Henning, T., Burkert, A., Launhardt, R., Leinert, C., & Stecklum, B., *Infrared Imaging and Millimetre Continuum Mapping of Herbig Ae/Be and FU Orionis Stars*, A&A, 336, 565, 1998.

Heyminck, S. & Graf, U.U., *Reflection gratings as THz local oscillator multiplexer*, Proc. SPIE Vol. 4014, 1998.

Hildebrand, R.H., *The Determination of Cloud Masses and Dust Characteristics from Submillimetre Thermal Emission*, QJRAS, 24, 267, 1983.

Hogerheijde, M.R., *The Serpens Star Forming Region in HCO+, HCN, and N2H+*, SFChem 2002, Edited by Charles L. Curry and Michel Fich. To be published by NRC Press, Ottawa, Canada, p. 44.

REFERENCES - *Continued*

Jewell, P.R. & Mangum, J.G., *System Temperatures, Single Versus Double Sideband Operation and Optimum Receiver Performance,* ALMA Memo 170, 1997.

Johansson, J.F., & Whyborn, N.D., *The Diagonal Horn as a Sub-Millimeter Wave Antenna*, IEEE MTT, Vol. 40, No, 5, 1992.

Johnson, H. L., *Photometric Distances of Galactic Clusters*, ApJ, 126, 121, 1957.

Kerr, A.R. Private Communication, 2003.

Kontinen, S., Harju, J., Haikkila, A., Haikala, L.K., *Molecular Line study of Evolution in Protostellar Cloud Cores*, A&A, 361, 704, 2000.

Kooi, J.W., *Cryogenic Low Noise Balanced IF Amplifiers*, CSO Memo, 1998.

Kooi, J.W., Chattopadhyay, G., Thielman, M., Phillips, T.G., & Schieder, R. *Noise Stability of SIS Receivers,* Int J. IR and MM Waves, Vol. 21, No. 5, May, 2000.

Kulesa, C. Private Communication, 2003.

Kuo, C.L. et al., *ACBAR Measurements of CMB Angular Power Spectrum*, American Astronomical Society Meeting 200, #06.03, 2002.

Lamb, J.W., *SSB vs. DSB for Submillimeter Receivers*, ALMA Memo 301, 2001.

Levreault, R.M., *A Search for Molecular Outflows Toward Pre-Main-Sequence Objects,* ApJSS, 67, 283, 1988.

Loren, R.B., *The Star Formation Process in Molecular Clouds Associated with Herbig Be/Ae Stars. II. The Nonhomologous Collapse of the CrA Cloud*, ApJ, 227, 832, 1979.

Loren, R.B, Sandqvist, Aa., & Wooten, A., *Molecular Clouds on the Threshold of Star Formation: The Radial Density Profile of the Cores of the Rho Ophiuchi and R Coronae Australis Clouds*, ApJ, 270, 620, 1983.

Lovas, F.J., *NIST Recommended Rest Frequencies for Observed Interstellar Molecular Microwave Transitions,* NIST web search engine, 2003.

Mannings, V., *Submillimetre Observations of Herbig Ae./Be Systems*, MNRAS, 271, 587, 1994.

REFERENCES - *Continued*

Mardones, D., Myers, P.C., Tafalla, M., Wilner, D.J., *A Search for Infall Motions Toward Nearby Young Stellar Objects,* ApJ, 489, 719, 1997.

Martin, D. H., El-Atawy, S., Duncan, W. D., Puplett, E. F., Fonti, S. *A new balloon-borne measurement of the cosmic background,* Societa Astronomica Italiana, Memorie, vol. 49,1978.

Mehdi, I., Schlecht, E., Chattopadhyay, G., Siegel, P.H. *THz local oscillator sources: performance and capabilities*, Proc. SPIE Vol. 4855, 2003.

Mueller, E., 2001, DeMaria ElectroOptics Systems, Inc., 1280 Blue Hills Ave., Bloomfield, CT 06002.

Myers, P.C., Mardones, D., Tafalla, M., Williams, J.P., & Wilner, D.J., *A Simple Model of Spectral-Line Profiles from Contracting Clouds*, ApJL, 465, L133, 1996.

Narayanan, G., Walker, C.K., *Evidence for Multiple Outbursts from the Cepheus A Molecular Outflow,* ApJ, 466, 844, 1996.

Narayanan, G., Walker, C.K., Buckley, H.D., *The Blue Bulge Signature towards IRAS 16293-2422,* ApJ, 496, 292, 1998.

Narayanan, G., Walker, C.K., Buckley, H.D., *The Blue Bulge Signature towards IRAS 16293-2422 - Erratum,* ApJ, 530, 1105, 2000.

Narayanan, G. *Allan varience algorithm*, Private Communication, 2003.

Schieder, R.T. et al. *Toward very large bandwidth with acousto-optical spectrometers,* Proc. SPIE Vol. 4855, 2003.

Schuster, K., Blondel, J.,Carter, M., Fouilleux, B., Lazareff, B.,Mattiocco, M., Pollet, J., *The IRAM 230 GHz Multibeam SIS Receiver,* Imaging at Radio Through Submillimeter Wavelengths, ASP Conference Proceedings Series, Vol. CS-217, 2000.
REFERENCES - *Continued*

Snell, R.L., Scoville, N.Z., Sanders, D.B., Erickson, N.R., *High Velocity Molecular Jets,* ApJ, 284, 176, 1984.

Shu, F.H., *Self-similar collapse of isothermal spheres and star formation,* ApJ, 214, 488, 1977.

REFERENCES - *Continued*

Stahler, S.W., Shu, F.H., & Tamm, R.E., *The evolution of protostars. II - The hydrostatic core*, ApJ, 242, 226, 1980.

Stark, A. et al., *The Antarctic Submillimeter Telescope and Remote Observatory (AST/RO)*, PASP, Volume 113, Issue 783, 2001.

Sunada, K.,Yamaguchi, C.,Kuno, N. & Ukita, N., *Development and First Results of NRO 25-BEam Array Receiver System (BEARS)*, Imaging at Radio Through Submillimeter Wavelengths, ASP Conference Proceedings Series, Vol. CS-217, 2000.

Tafalla, M., Mardones, D., Myers, P.C., Caselli, P., Bachiller, R., & Benson, P.J., *L1544: A Starless Dense Core with Extended Inward Motions*, ApJ, 504, 900, 1998.

Taylor, K.N.R., & Storey, J.W.V., *The Coronet, an obscured cluster adjacent to R Corona Austrina*, MNRAS, 209, 5, 1984.

Thompson, A.R., & Kerr, A.R., *Relative Sensitivities of Single and Double Sideband Receivers for the MMA*, ALMA Memo 168, 1997.

Torrelles, J. M., Gomez, J. F., Garay, G., Rodriguez, L. F., Curiel,S., Cohen, R. J., & Ho, P. T. P., *Systems with H_2O Maser and 1.3 Centimeter Continuum Emission in Cepheus A*, ApJ, 209, 262 1998.

Turner, B.E., *Vibrationally excited CS in IRC + 10216*, A&A, 182, L15, 1987.

Vilas-Boas, J.W.S., Myers, P.C., Fuller, G.A., *Dense Cores of Dark Clouds. XII. ^{13}CO and C18O in Lupus, Corona Australis, Vela and Scorpius*, ApJ, 532, 1038, 2000.

Walker, C.K., Lada, C.J., Young, E.T., & Margulis, M., *An Unusual Outflow around IRAS 16293-2422*, ApJ, 332, 335, 1988.

Walker, C.K, Adams, F.C., & Lada, C.J., *1.3 Millimeter Continuum Observations of Cold Molecular Cloud Cores*, ApJ, 349, 515, 1990.

Walker, C.K., Carlstrom, J.E., Bieging, J.H., Lada, C.J. & Young, E.T., *Observations of the Dense Gas in the IRAS 16293-2422 Outflow System*, ApJ, 364, 173, 1990.
REFERENCES - *Continued*

Walker, C.K., Carlstrom, J.E. & Bieging, J.H., *The IRAS 16293-2422 Cloud Core: A Study of a Young Binary System*, ApJ, 402, 665, 1993.

REFERENCES - *Continued*

Walker, C.K., Narayanan, G., Buttgenbach, T.H., Carlstrom, J.E., Keene, J. & Phillips, T.G., *The Detection of [CI] in Molecular Outflows Associated with Young Stellar Objects*, ApJ, 415, 672, 1993.

Walker, C.K., Maloney, P.R., & Serabyn, E., *Vibrationally Excited CS: A New Probe of Conditions in Young Protostellar Systems*, ApJL, 437, L127, 1994.

Walker, C.K. NSF ATI Proposal, 2003.

Wilking, B.A., Harvey, P.M., Joy, M., Hyland, A.R., & Jones, T.J., *Far-Infrared Observations of Young Clusters Embedded in the R Coronae Australis and Rho Ophiuchi Dark Clouds*, ApJ, 293, 165, 1985.

Wilking, B.A., McCaughrean, M.J., Burton, M.G., Giblin, T., Rayner, J.T., & Zinnecker, H., *Deep Infrared Imaging of the R Coronae Australis Cloud Core*, AJ, 114, 2029, 1997.

Wilson, R. W.; Jefferts, K. B.; Penzias, A. A., *Carbon Monoxide in the Orion Nebula*, ApJ, 161, L43, 1970.

Ziurys, L.M., Turner, B.E., *Detection of interstellar vibrationally excited HCN*, ApJ, 300, L19.